SFB 837
**Interaktionsmodelle für den
maschinellen Tunnelbau**

Rheological Investigation of Particle-Foam Mixtures

Aycan Özlem Özarmut

Rheological Investigation of Particle-Foam Mixtures

Dissertation
zur
Erlangung des Grades
Doktor-Ingenieur

der
Fakultät für Bau- und Umweltingenieurwissenschaften
der Ruhr-Universität Bochum

von

Aycan Ö. Özarmut

aus Erzincan, Türkei

Bochum 2018

This thesis is dedicated to my grandfathers

Kamber AYDIN (1935 - 2013) & Mustafa AYDIN (1931 - 2015)

Acknowledgements

Firstly, I would like to express my sincere gratitude to my advisor Prof. Dr.-Ing. Holger Steeb for the continuous support of my Ph.D study and related research, for his patience, motivation, and immense knowledge. His guidance helped me in all the time of research and writing of this thesis.

Besides my advisor, I would like to thank Prof. Dr.-Ing. Markus Thewes for his insightful comments and having useful discussion.

My sincere thanks also go to Petra Nagel and Stefan Seifert for their coordinative technical supports in experiments. I also greatly thank to my colleagues for their direct or in-direct co-operation and help which facilitated the working atmosphere. I also thank my subproject partner, Dr.-Ing. Mario Galli for our own little scientific community.

Last but not the least, I especially thank my daughter, my husband, my parents and my brother for supporting me throughout writing this thesis and my life in general. Without their support, encouragement and understanding, it would have not been possible for me to achieve this research.

Bochum, April 2017

Aycan Özlem Özarmut

Abstract

In Earth Pressure Balance (EPB) tunnelling the excavated ground is used as face support medium to prevent surface settlements. In general, the excavated ground (e.g. for cohesionless soils) does not exhibit suitable conditions to support the tunnelling face. This technical challenge can be solved by adding conditioning agents that are mainly foams. In order to physically understand the rheological properties of the (added) liquid foam and the foam-soil (foam-particle) mixture and to comprehend its influence on the soil, advanced rheological investigations are necessary. Since the morphology, i.e. the microstructure of the foam accounts for effective rheological properties, size, shape and distribution of the cells of the foam and particle-foam mixture were characterized in detail by applying imaging techniques. To perform the rheological experiments, polymer-stabilised shaving foam seems to be a good replacement of tunnelling foam and suitable for laboratory tests due to its time stability, characteristic length scales of the microstructure and accessibility. Glass beads (of different diameter and volume fractions, i.e. specific surface areas) are used to investigate the effective material behaviour of synthetic foam-particle mixtures. The experimental results are compared with an appropriate model (modified Herschel-Bulkley-Papanastasiou type).

Liquid foam and its mixture with glass beads are non-Newtonian fluid causing wall slip effects at solid boundaries like plate-plate geometries in rheological experimental investigations. However, an accurate rheological experiment can be obtained by eliminating the slip effect. In order to understand the slip effect, a visualization method was used to get images of materials. The slip velocity was determined by the hypothesis of following Mooney and Oldroyd & Jastrzebski. The slip velocity, which was determined by the visualization technique, was compared to the corrected slip velocity. In addition, rough surfaces (P320-sandpaper) were used to minimize slip effect for rheological experiments.

For advanced rheological investigations, heterogeneous experiments can also be used to verify the ascertained material parameters. For instance, the mini-slump test (heterogeneous experiment), which is a simple and cheap rheological experiment, was performed to determine the flowability of the surface wetted particle foam mixtures. To interpret this experiment, the Lagrangian meshfree Smoothed Particle Hydrodynamics method (SPH) is used to provide numerical simulations of fluid flow with free surfaces.

Kurzfassung

Im maschinellen (EPB) Tunnelbau wird der abgetragene Boden als unterstützendes Medium benutzt, um die Ortsbrust zu stabilisieren und Oberflächensetzungen zu verhindern. Generell weist der ausgehobene Boden keine geeigneten Eigenschaften auf, um den Tunnelvortrieb zu unterstützen. Diese technische Herausforderung kann durch Zugabe von Konditionierungsmitteln, welche aus Tensidschäumen bestehen, gelöst werden. Um die rheologischen Eigenschaften des flüssigen Schaums und der Schaum-Boden Mischung sowie deren Einfluss auf den Boden physikalisch zu charakterisieren, sind weitergehende rheologische Untersuchungen notwendig. Da die Morphologie des Gemisches, wie zum Beispiel die Mikrostruktur des Schaums, die effektiven rheologischen Eigenschaften maßgeblich beeinflusst, wurden durch bildgebende Verfahren die Größe, Form und Verteilung der Schaumzellen und der Schaum-Partikel Mischung eingehend charakterisiert. Zur Durchführung von rheologischen Experimenten unter Laborbedingungen erwiesen sich polymerstabilisierte Rasierschäume als adäquater Ersatz für Schäume, welche im Tunnelbau eingesetzt werden. Aufgrund ihrer Langzeitstabilität und der charakteristischen Längenskalen der Mikrostruktur sowie der leichten Zugänglichkeit eignen sich Rasierschäume besonders gut für Laboruntersuchungen. Glaskugeln mit verschiedenen Durchmessern und Volumenanteilen und damit spezifischen Oberflächen, wurden eingesetzt, um das effektive Materialverhalten von Schaum-Partikel Mischungen zu untersuchen. Die experimentellen Ergebnisse wurden anschließend mit geeigneten rheologischen Modellen verglichen, wie zum Beispiel dem modifizierten Herschel-Bulkley-Papanastasiou Model.

Bei flüssigen Schäumen und Glaskugel-Schaum Gemischen handelt es sich um Nicht-Newtonsche Fluide, die an Grenzflächen (Schaum-Partikel Gemisch / Metalloberfläche) frei gleiten können („Free Slip"). Durch die Eliminierung der Wandgleitung können allerdings präzise genauere rheologische Interpretationen der Messergebnisse erzielt werden. Zum besseren Verständnis des Wandgleit-Effekts wurden bildgebende Visualisierungsmethoden eingesetzt und die Schlupfgeschwindigkeit nach Mooney und Oldroyd & Jastrzebski bestimmt. Die aus der Visualisierungsmethode ermittelte Schlupfgeschwindigkeit wurde mit der korrigierten Schlupfgeschwindigkeit verglichen. Zusätzlich wurden raue Oberflächen (P320-Sandpapier) eingesetzt, um den Grenzflächeneffekt in rheologischen Experimenten zu verringern. Bei fortgeschrittenen rheologischen Untersuchungen können sogenannte heterogene Experimente eingesetzt werden, um die ermittelten konstitutiven Eigenschaften zu validieren. In dieser Arbeit wurde ein kleinskaliger Setzversuch (heterogenes Experiment) durchgeführt, um die Fließfähigkeit der oberflächenbenetzten Mischung zu bestimmen. Zur Auswertung dieser heterogenen Experimente werden Smoothed Particle Hydrodynamics (SPH) Simulationen herangezogen, um numerische Untersuchungen von Fluidströmungen mit freien Oberflächen bereitzustellen.

Contents

List of Figures

List of Tables

Chapter 1

Introduction and Motivation

The human population on Earth is growing very rapidly and now it is greater than 7 billion [40]. 200 years ago the world population was less than 1 billion [79]. Under the circumstances it is clear that large infrastructure programs based e.g. on mechanized tunnelling has a crucial role providing an easy and economical transportation under ground. The process of mechanized tunnelling is applied by specific Tunnel Boring Machines (TBM). In this study, an Earth Pressure Balance (EPB) shield machine, which is the type of specific TBM, is applied in the tunnelling process.

An EPB shield machine works with the combination of three main subjects: soil mechanics (soil characteristics and pressure support), TBM technology (cutterhead design, installed force, screw conveyor, etc.) and soil conditioning additives. In order to satisfy continuous support of the tunnelling face, the excavated soil is used in an EPB shield machine. Due to many benefits of the soil conditoning, the excavated soil is one of the most important subjects in the operation of an EPB shield machine. The soil conditioning provides an improved workability of the excavated soil, reducing friction and cutterhead torque, increasing face stability and controlling groundwater, etc. [82]. However, when the soil conditioning is not used in tunnelling, which means the natural ground does not have a consistency to form a low permeability and high content of fines (ideal soil), the control of pressure in the excavation chamber is not possible, causing the machine to stop working. Therefore, conditioning agents, such as foam, water, bentonite or polymer, must be mixed with the soil collected in the excavation chamber to have the above mentioned ideal soil properties. The distinct properties of each conditioning agent has different effects on the different soil properties. For instance, the effect of foam strongly depends on its decomposition, i.e. volume fraction also called foam expansion ratio and injection ratio. Additionally, the conditioning agents can be also used in combination. Their effect on different soil varies when they are used in combination. On the other hand, the soil properties, such as permeability, the distribution of the particle sizes, have an influence on the overall

performance of soil conditioning.

In order to understand the influence of the conditioning agent on the soil, the conditioning agent should be investigated in laboratory on micro- and macro-scale. In mechanized tunnelling, it is possible to find various studies on soil conditioning an engineering scale. For instance, Maidl [73] studied foam and its influence on the soil; Quebaud [94] investigated foam with different type of sand; Budach [18] carried out experimental investigations of foam and foam-soil mixtures; Thewes et al. [112] investigated foam with the combination of saturated- and unsaturated-soil. On the micro-scale, i.e. the scale where discrete foam cells can be observed, liquid foam has also been investigated by several authors. Kroezen et al. [61] researched foam experimentally by using a coaxial viscometer. The rheological experiments of foam, which were performed by using a plate mode of rheometrics mechanical spectrometer, were investigated by Khan et al. [57]. Marze et al. [78] used a rheometer with selfmade cone-plate geometries to measure flow curve tests of foam. However, investigation of the conditioning agent (foam) combined with particle on the micro-scale are rarely available in literature.

Therefore, the rheological behavior and micro-structure of particle-foam mixtures should be investigated intensively. On the micro-scale, the research on the particle-foam mixture aims at devoloping a constitutive model that can describe its effective rheological behaviour. For this purpose, an existing rheological model (Herschel-Bulkley-Papanastasiou model) is modified and its parameters are optimized by means of rheological experiments performed with particle-foam mixtures differing in terms of the amount of constituents. However, slip effect occured in the rheological experiment, which is a challenge for rheological experiments and seen frequently. In order to perform the rheological tests, the slip effect was minimized by using sandpaper on the surface of the measuring devices (plate-plate configurations). On the other hand, the slip effect was also investigated intensively for rheological experiments. Since the focus of this study are micro-scale properties of the conditioning agent, the syntetic foam (shaving foam) and solid glass beads have been utilized for rheological experiments due to difficulties an performing experiments with (time-unstable) tunnelling foam and soil. A synthetic foam is suitable for laboratory tests due to its time stability, characteristic length scales of the microstructure and accesibility. Solid glass beads are used to investigate the effective material behavior of foam-particle mixture. In addition, a mini slump test was performed to determine the flowability of the foam particle mixtures for the rheological investigation. To verify the experimental results, a numerical simulation (smoothed particle hydrodynamics method) were applied by using inverse analysis.

1.1 Scope and Outline

The aim of the project is to investigate soil conditioning agent experimentally and to develop the appropriate rheological constitutive model of the particle-foam mixtures for the EPB machine. The research presented in this thesis was carried out to show the effects of the conditioning agent (foam) on the particle (soil) in the laboratory and to manage an experimental challenge like slip effect during the rheological research. The work of this thesis are summarised as follows:

- Chapter 2 introduces mechanized tunnelling with EPB machines. The excavation process of the EPB machine is explained to show how soil conditioning is important for face stability of EPB tunnelling. The influence of the soil conditioning agent (foam) parameters (C_F, FIR and FER) are discussed due to their crucial role in EPB tunnelling. The importance of rheological properties and workability of the soil-foam mixture and literature review of the soil conditioning are presented.

- Basic equations of a continuum description are presented to describe fluid-flow in Chapter 3. The Navier-Stokes equations for incompressible fluids are also presented in cartesian, cylindrical and spherical coordinate systems.

- Chapter 4 presents basic principles of rheology. Rheological experiments and the history of the rheometry are summarised. The properties and ingredients of a liquid foam (shaving foam), used for rheological experiments, is presented. The working process of the rheometry is explained within rheological terms and equations. The geometry type and their advantages are given to use most suitable one for liquid foam and/or particle-foam mixtures. In addition, the specific type of fluid is classified. In order to use non-Newtonian constitutive models for foam-particle mixtures, some models and especially the modified Herschel-Bulkley-Papanastasiou model [90] are presented with the viscosity function at zero and infinite shear rate. This model is derived for cone-plate and plate-plate geometries in spherical and cylindrical coordinates, respectively. The boundary conditions with and without slip effect is discussed for plate-plate geometry.

- Chapter 5 discusses rheological experiments and micro-structure of liquid-foam and dry- and surface wetted particle-foam mixtures. A rheological constitutive model, which is the appropriate model for our experimental results, is matched with the flow curve data. Rheological characterization of foam and particle foam mixtures are defined for various volume fraction of dry- and wet particle mixtures.

- The slip effect is conducted for rheological experiments of non-Newtonian fluids in Chapter 6. Two assumptions the Mooney and Oldroyd-Jastrzebski methods are presented to determine slip velocity of materials. Additionally, for the calibration of smooth plate-plate, rough plate-plate and glass plate-plate geometries, two calibration oils (APN145 and APN26) are used to calibrate the geometries. The slip velocity is also determined through image analysis.

- The (heterogeneous) mini slump test is presented and compared with numerical simulations in Chapter 7. For the comparison of the experimental and numerical simulation, various volume fractions of surface wetted particle-foam mixture have used. The slip effect is conducted to show how affect the flowability of foam and surface wetted particle-foam mixture. Numerical simulation (Smoothed Particle Hydrodynamics method), which have been performed by Sivanesipillai et al. [105], are used to compare the rheological experiments for foam and particle-foam mixture.

- Chapter 8 summarises the conclusions of this work, research soil conditioning for EPB tunnelling. The crucial role of the rheological behavior is explained for soil conditioning and the constitutive rheological model is discussed for rheological experiments.

Chapter 2

Mechanized Tunnelling with EPB Machines

2.1 Mechanized Tunneling

The tunnels have been built for various reasons such as protection of goods and improvement of transportation routes [72]. In 1825, the first tunnel boring machine (TBM), which was used to excavate the Rotherhithe tunnel under the Thames, was developed by Sir Marc Isambard Brunel. In 1876, John Dickinson Brunton and George Brunton were awarded for the first mechanised full face TBM. Around the 1960s, the Japanese built the EPB shield machine to solve some challenges, including reduction in costs, and laws on air and water pollution, for a method of tunnelling through soft ground. In the 1960s, the earth pressure balance (EPB) was developed in Europe. This type of TBM has been used since the 1960s.

The term "mechanized tunnelling" stands for the tunnelling technique where the excavation process is performed mechanically by a TBM. In unstable ground, tunnelling processes need face support to prevent collapse. In order to achieve the required face support pressure, support mediums, which have a crucial role, are used in mechanized tunnelling. Thus, the types of TBM, such as slurry shields and EPB shields, derive from what type of support medium is choosen for the construction of tunnelling. Slurry shield (hydro shield) machines are used to accomplish the face support by pressurized slurry. The pressurized slurry is usually a bentonite suspension, which is a mixture of special clay and water. The bentonite slurry is used for face support, as well as to help transport excavated soil easily. Comparing EPB machines and slurry machines, the EPB is regarded as the most employed machine in mechanized tunnelling due to its vast applicability. The application fields of EPB are soil, soft rock and highly fractured hardrock, especially those with high water content [45]. On the other hand, the excavated soil is used as a support medium

in EPB shield machines. Since the face support is provided by excavated soil in the excavation chamber, EPB shield machines do not need a secondary support medium, as is the case with slurry shield machines. However, excavated soil should be mixed with conditioners to achieve an ideal ground condition in EPB shield machines. The most important advantage of EPB shield machines is the low investment cost due to seperation plant [74].

The excavation process is done with a trailing support mechanism (back-up system) of EPB. The support mechanism can include conveyors, electrical systems, ventilation and control rooms. A cross-section of the EPB shield machines can be seen in Figure 2.1 with their tools; (1) cutting wheel, (2) excavation chamber, (3) bulkhead, (4) a man lock, (5) screw conveyor, (6) thrust jacks, (7) a segment erector, (8) thick shield, (9) a segment feeder and (10) belt conveyor. The cutting wheel, which is at the front of the shield, excavates the ground. It is the main excavation tool and has many holes. Through these holes, the excavated soil enters the excavation chamber. The excavation chamber is the area of the shield, where the cutting wheel rotates. Additionally, cutting wheel inspection is carried out through a man lock, which allows access to the excavation chamber under compressed air.
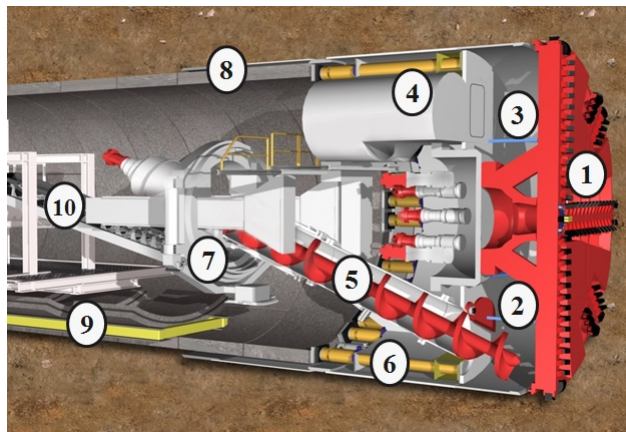
Figure 2.1: Cross section of an EPB shield machine with its tools (Herrenknecht AG)

The excavated soil can be mixed with conditioning agents (foam, polymers etc.) and the conditioned excavated soil fills the excavation chamber completely. In order to compensate for tunnel face pressure, pressure should be created inside the excavation chamber. The inflows of soil and conditioning agents controll pressure level. The earth pressure sensors measure the pressure level at the bulkhead. The bulkhead separates the excavation chamber under atmospheric pressure from the remaining EPB shield machines. During tunnel construction, the most important issue is the removal of the excavated soil to prevent idle times. The conditioned excavated soil is transported by the screw

conveyor and is carried out of the tunnel by the belt conveyor. At the end of the EPB shield machine, the segment erector erects the segmented tunnel lining sequentially. The tunnel lining consists of reinforced lining segments and ensures the stability and structural safety of the tunnel [72]. In order to carry out a forward movement of the TBM and allow the excavation of the ground, thrust jacks (thrust cylinder) are used to push against the already installed tunnel segments.

2.2 Soil Conditioning in EPB Tunnelling

Soil conditioning has a crucial role in supporting the tunnel face by improving excavated soil properties. They cause the excavated soil to become more plastic with low permeability and low internal friction which prevents clogging and difficulties with transportation in EPB machines. They also improve durability and reduce of power requirements at the cutterhead. Additionally, the conditioning agents allow for control of pressure in the chamber and screw conveyor. If the support pressure varries and cannot be controlled for face collapsing is inevitable and the excavation process will stop. Thus, the conditioning agents affect the performance of EPB machines. Maidl et al. [72] mentioned that the application field of EPB machine is restricted to fine grained soils, when it is used without soil conditioning agents. The soil is conditioned by injecting additives through the cutting wheel or the bulk head into the excavation chamber. Foam is usually used as a conditioning agent in mechanized tunnelling. Additonally, to prevent the earth pressure from dropping during interruptions of the excavation process, bentonite suspension is injected into the excavation chamber as an additional face support system [8]. If the excavation process cannot be continued in a TBM, the injection of foam must be stopped and an additional material (bentonite suspension) is added to the excavation chamber. In order to use an additional face support system, the TBM needs one or several tanks of bentonite suspension. As it is mentioned in [37, 93], bentonite suspensions are thixotropic fluids made by mixing bentonite and water. The bentonite consists of the clay mineral, sodium montmorillonite. The montmorillonite, which consists of thin flat sheets of clay particles, absorb water. It has a higher viscosity than the other types of bentonite and is the most dispersing type of bentonite [93]. In [37], several tests are used to characterize the bentonite suspensions:

- shear strength

- run out time of the Marsh funnel, a simple device to measure viscosity of the bentonite suspensions [93]

- density, determined by a mud balance test

- distribution of grains, which gives a clue to the permeability

- size and geometry of grains

In EPB machines, synthetic polymers (polyacrylamides) have been used as conditioning agents with bentonite or foam [7]. When polymers are used as soil conditioning agents, they inhibit the ground from absorbing water. However, they can also be used seperately.

2.2.1   Foam

Foam is the most suitable and useful conditioning agent when the excavation process is performed through coarser ground (the extended application range of EPB machines). Thewes [111] and Budach et al. [19] showed that the application range of EPB machines can be extended from fine-grained soil to coarse-grained soil by the use of foam. In coarse-grained soils, the permeability of the soil (k) should not exceed 10^{-5} m/s to prevent uncontrolled groundwater inflow [50]. A suitable type of foam is selected as a conditioning agent according to the geological condition (groundwater and soil permeability), soil type, and the characteristics of the tunnel boring machine (open or closed cutterhead, type of foam generator, etc). The selection of foam type according to soil properties was considered in [28]. An appropriate soil-foam mixture requires the foam types shown in Figure 2.2 to be matched with particular soils. Type A has a high dispersion (rate) and good coating capacity. Type B has medium stability, whereas type C has high stability and anti segregation properties. Type C can be used to develop impermeability of a cohesive soil.

Soil	Foam Types				Polymer Additives
	A	B	C	*FIR*	
Clay	●			30-80	Anti clogging polymer
Sandy Clay-Silt	●	●		40-60	Anti clogging polymer
Sand-Clayey silt		●		20-40	Polymer for consistency control
Sand		●	●	30-40	Polymer for cohosiveness and consistency control
Clayey Gravels			●	25-50	Polymer for cohosiveness and consistency control
Sandy Gravels			●	30-60	Polymer for cohosiveness and consistency control

Figure 2.2: Foam types depending on different soils for EPB machines [28].

In Figure 2.2, the indicative values of Foam Injection Ratio *FIR* can be seen for different types of foam. In order to understand *FIR* [vol%], *FER* [%] (Foam Expansion Ratio) and C_F [vol%] (Concentration of the foaming solution), Figure 2.3 is sketched to show volume and mass of foam, dry- and wetted

particle.
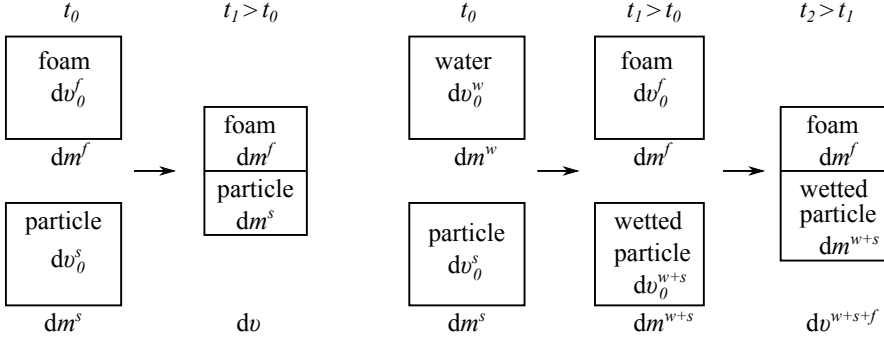
Figure 2.3: (a) Total volume of dry particle-foam mixture $t_1 > t_0$. (b) Pre-wetted particle-foam mixture at $t_2 > t_1$.

FIR is defined as the ratio of the volume of foam $\mathrm{d}v_0^f$ to the volume of excavated soil (particle) $\mathrm{d}v_0^s$. Foam injection ratio is determined by laboratory testing and the water content of the soil plays an important role in this process

$$FIR = 100 \; \frac{\mathrm{d}v_0^f}{\mathrm{d}v_0^s}, \qquad\qquad FIR = 100 \; \frac{\mathrm{d}v_0^f}{\mathrm{d}v_0^{w+s}}. \qquad (2.1)$$

Foam expantion ratio, which is also used in the tunnelling process, is the ratio of the volume of foam $\mathrm{d}v_0^f$ to the liquid phase volume of the foam $\mathrm{d}v_0^{f_l}$,

$$FER = \frac{\mathrm{d}v_0^f}{\mathrm{d}v_0^{f_l}}. \qquad (2.2)$$

The third parameter used to define foam properties is C_F. It determines the concentration of the foaming surfactant in water. C_F is determined by

$$C_F = 100 \; \frac{\mathrm{d}m^F}{\mathrm{d}m^F + \mathrm{d}m^W}, \qquad (2.3)$$

where $\mathrm{d}m^F$ is the mass of foaming surfactant, $\mathrm{d}m^W$ is the mass of water and $\mathrm{d}m^F + \mathrm{d}m^W$ is the mass of the foaming solution. These three parameters (C_F, FIR and FER) have a crucial role in mechanized tunneling. If the parameters are not calculated correctly, some challenges may occur during tunnelling process [62]. The injection of air can be too high in working chamber, which causes insufficient speed. On the other hand, too much foam can be injected, causing the soil to be squeezed into the screw conveyor, resulting in an increase

in the cost of the working process per linear meter of tunnel. Furthermore, the muck inside the working chamber cannot be handled easily. The last challenge is insufficient soil conditioning. Due to the insufficient soil conditioning, pressure decreases in the front of the TBM and plugging of the soil appears in the chamber and/or cutterhead.

In soil conditioning, the effectiveness of foam can be evaluated with various tests. In order to characterise foam, some tests were recommended by Quebaud et al. [94]: The consistency test is applied for the bubble size, the compressibility test, which was not investigated in this study, is used in order to understand foam behavior under pressure and the half-life test is applied to measure the time. However, the properties derived from these test are not sufficient to use in EPB machine. In addition, for mechanized tunnelling, foam mixed with soil should be tested. Several tests, such as compressibility, foam penetration, slump, permeability, etc. are performed to determine the properties of soil-foam mixture:

- workability

- rheological properties

- density

- sedimentation

- permeability

- compression behavior

- shear strength, and

- stability.

All of the properties have an influence on the operation of EPB machines. For instance, if the compressibility of the soil increases in the excavation chamber, the workability and homogeneity of the soil-foam mixture will be improved, meaning that the mixture in the chamber becomes plastic. It provides better control of the stability of the face. In order to minimize the possibility of face collapse, the permeabilty of soil should be reduced at the face because of water inflow. When the shear strength of the soil is considered, it affects the wear of the cutting wheel. If it decreases, the wear of cutting tool reduces and energy can be saved for the TBM.

Rheological Properties and Workability

The rheological property of soil-foam mixtures is important for the excavation process. It describes the flow behaviour of the mixture under various forces

(e.g. stress). When the viscosity of the mixture is very high, flow through the screw conveyor may decelerate or stop. This reduces the performance of the TBM and increases the cost of working process.

Figure 2.4: Foam generator at Ruhr-University Bochum [112]

The workability of soil-foam mixture mentioned in [112] is an indicator for the plasticity of the support medium in mechanized tunnelling. Kosmatka et al. [58] defined workability as a measure of how easy or difficult concrete can be placed, consolidated, and finished. Due to determination of the workability, a slump test was used according to DIN EN 12350-2 /-8 [3, 4] for fresh concrete and self compacting concrete by Thewes et al. [112]. In order to perform the test under realistic boundary conditions, the foam used in the mixture was generated by the foam generator (Figure 2.4) of the Institute for Tunnelling and Construction Management at Ruhr-University Bochum.

2.2.2 State of the Art

Soil conditioning was investigated by various researchers in the framework of EPB tunnelling. Peila et al. [91] investigated the soil conditioning process in which the ground is extracted from the excavation chamber. They used a large-scale pressure tank to simulate the excavation chamber. Additionally, soil conditioning was researched experimentally by Maidl [72] to show the effects of foam on the excavated soil. Bezuijen et al. [14] investigated the influence of soil permeability on the foam. They worked on the interaction between soil mechanics and soil conditioning experimentally and theoretically.

On the micro-scale, foams have also been analysed rheologically. Shear flow properties of liquid foam was studied experimentally and the effect of wall slip was determined on the rheological behaviour of liquid foam in [57, 61]. However, there are not many known investigations about soil-foam mixtures. In order to understand soil conditioning in mechanized tunnelling, soil-foam mixtures should be investigated from micro-scale to macro-scale. Therefore, the rheological property and workability (slump test) of soil-foam mixture should

be researched on a micro-scale. In this study, a synthetic foam and particle-foam mixtures have been investigated on a micro-scale.

Chapter 3

Theoretical Background of Fluid Flow

3.1   Description of Fluid Flow

In Euclidean space, the independent variables, which describe a fluid, are function of position $\mathbf{x}$ at time t. We assume that the fluid is identified with a material body B at $t = 0$ in a fixed reference configuration and B is reffered as the reference body. As the fluid flows, the material points of the fluid will be at new spatial positions, occupying the body B_t at time t. The body is referred as the current configuration.
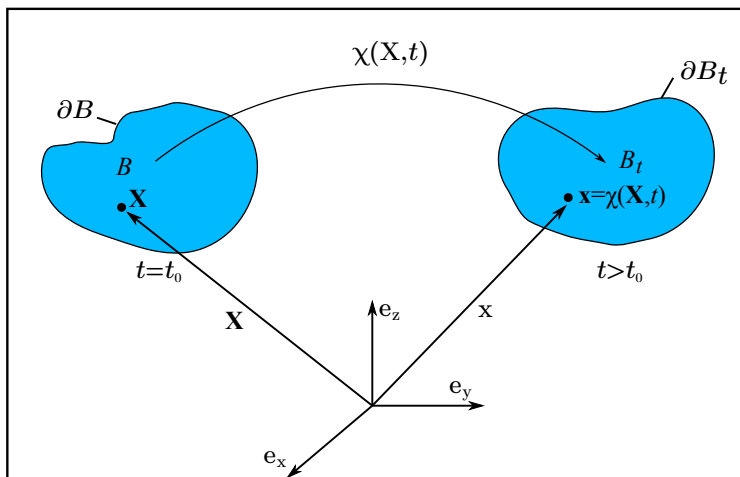
Figure 3.1: Euclidean space with the reference body B and the current configuration B_t.

The Lagrangian and the Eulerian description can be used to describe fluid

flow in continuum mechanics. In the Lagrangian description, fluid flow properties are determined by tracking the kinematics of each material point, and the velocities, acceleration and positions, depending on time. For instance, the position vector $\mathbf{x} = \boldsymbol{\chi}(\mathbf{X}, t)$ is introduced as the position of a fluid particle at time t, which was located at $\mathbf{X}$ at time $t = 0$ (Figure 3.1). The motion function $\boldsymbol{\chi}(\mathbf{X}, t)$ is describing the motion of the material point and can be evaluated at time t for all material position vector $\mathbf{X}$. From the first and second time derivatives of the position vector $\mathbf{x}$, the velocity and acceleration can be determined by

$$\mathbf{u} = \dot{\mathbf{x}}(\mathbf{X}, t) = \frac{\mathrm{d}\boldsymbol{\chi}(\mathbf{X}, t)}{\mathrm{d}t} \qquad\qquad \mathbf{a} = \ddot{\mathbf{x}}(\mathbf{X}, t) = \frac{\mathrm{d}^2\boldsymbol{\chi}(\mathbf{X}, t)}{\mathrm{d}t^2}. \qquad (3.1)$$

Axiomatically, the mapping function $\mathbf{x} = \boldsymbol{\chi}(\mathbf{X}, t)$ is one-to-one in $\mathbf{X}$ for fixed time t and, therefore, has an inverse $\mathbf{X} = \boldsymbol{\chi}^{-1}(\mathbf{x}, t)$ at each time t [47]. However, the inverse of the motion function $\boldsymbol{\chi}$ requires that the Jacobian should be greater than zero

$$J = \det \mathbf{F} > 0, \qquad (3.2)$$

where $\mathbf{F}$ is the deformation gradient. $\mathbf{F}$ is equal to the partial derivative of $\mathbf{x}(\mathbf{X}, t)$ with respect to $\mathbf{X}$

$$\mathbf{F} = \frac{\partial \mathbf{x}}{\partial \mathbf{X}} = \mathrm{grad}\mathbf{x}. \qquad (3.3)$$

In the Eulerian description, the flow properties are expressed as a function of current position vector $\mathbf{x}$ and time. The fluid flow of a continuum using the Eulerian description is represented by the mapping function

$$\mathbf{X} = \boldsymbol{\chi}^{-1}(\mathbf{x}, t). \qquad (3.4)$$

From the Eulerian description, the velocity and acceleration are a function of current position vector $\mathbf{x}$ and time. The velocity and acceleration can be represented as follows:

$$\mathbf{u} = \dot{\mathbf{x}}(\mathbf{x}, t) \qquad\qquad \mathbf{a} = \ddot{\mathbf{x}}(\mathbf{x}, t). \qquad (3.5)$$

3.1.1 Displacement Field

The displacement vector **s** can be defined by the geometrical measurement of deformation. It is determined by

$$\mathbf{s} = \mathbf{x} - \mathbf{X}. \tag{3.6}$$

3.1.2 The Material Time Derivative

The material time derivative ($\frac{\mathrm{d}}{\mathrm{d}t}$), which is often used in fluid mechanics, is the time rate change of a quantity (scalar, vector or tensor) of a material. The time rate of change of velocity (vector) gives acceleration

$$\mathbf{a} = \frac{\mathrm{d}\mathbf{u}}{\mathrm{d}t} = \frac{\partial \mathbf{u}}{\partial t} + \frac{\partial \mathbf{u}}{\partial \mathbf{x}}\frac{\mathrm{d}\mathbf{x}}{\mathrm{d}t} = \frac{\partial \mathbf{u}}{\partial t} + \mathrm{grad}\mathbf{u} \cdot \mathbf{u}. \tag{3.7}$$

The material time derivative of velocity can be written in the components form

$$\frac{\partial(u\mathbf{e}_x)}{\partial t} + \frac{\partial(u\mathbf{e}_x)}{\partial x}\frac{\mathrm{d}x}{\mathrm{d}t} + \frac{\partial(u\mathbf{e}_x)}{\partial y}\frac{\mathrm{d}y}{\mathrm{d}t} + \frac{\partial(u\mathbf{e}_x)}{\partial z}\frac{\mathrm{d}z}{\mathrm{d}t},$$

$$\frac{\partial(u\mathbf{e}_y)}{\partial t} + \frac{\partial(u\mathbf{e}_y)}{\partial x}\frac{\mathrm{d}x}{\mathrm{d}t} + \frac{\partial(u\mathbf{e}_y)}{\partial y}\frac{\mathrm{d}y}{\mathrm{d}t} + \frac{\partial(u\mathbf{e}_y)}{\partial z}\frac{\mathrm{d}z}{\mathrm{d}t}, \tag{3.8}$$

$$\frac{\partial(u\mathbf{e}_z)}{\partial t} + \frac{\partial(u\mathbf{e}_z)}{\partial x}\frac{\mathrm{d}x}{\mathrm{d}t} + \frac{\partial(u\mathbf{e}_z)}{\partial y}\frac{\mathrm{d}y}{\mathrm{d}t} + \frac{\partial(u\mathbf{e}_z)}{\partial z}\frac{\mathrm{d}z}{\mathrm{d}t}.$$

In addition, the material time derivative of the density can be given as an example for a scalar quantity. The material time derivative of the density is

$$\dot{\rho} = \frac{\partial \rho}{\partial t} + \mathrm{grad}\rho \cdot \mathbf{u}. \tag{3.9}$$

3.2 Types of Flow

Fluid flow can be classified through the number of space coordinates; one-, two-, and three-dimensional flow

$$\begin{aligned} \mathbf{u} &= u\mathbf{e}_x && \text{(1D)}, \\ \mathbf{u} &= u\mathbf{e}_x + u\mathbf{e}_y && \text{(2D)}, \\ \mathbf{u} &= u\mathbf{e}_x + u\mathbf{e}_y + u\mathbf{e}_z && \text{(3D)}. \end{aligned} \tag{3.10}$$

However, fluid flow is generally in three-dimensional which is difficult to calculate the fluid flow problems. The challange can be achieved by reducing a three-dimensional flow to a two-dimensional one, thus the fluid flow problems can be solved as simple as possible. On the other hand, If the fluid flow at any location does not change with time, this type of flow called steady flow. Otherwise, it is called unsteady flow.

$$
\begin{aligned}
\mathbf{u} &= \mathbf{u}(\mathbf{x}, t) \qquad &\text{(unsteady flow)} \\
\mathbf{u} &= \mathbf{u}(\mathbf{x}) \qquad &\text{(steady flow)}
\end{aligned}
\tag{3.11}
$$

The type of fluid flow can be classified as incompressible and compressible flow due to density of a fluid. For an incompressible fluid flow, the density of a fluid is constant, thus the time rate of change of density is zero. If the density of a fluid varies with its pressure, the type of fluid flow is compressible.

$$
\rho(\mathbf{x}, t) = \rho(\mathbf{x}, t_0) \qquad \text{(incompressible flow)}
\tag{3.12}
$$

In uniform flow, flow parameters, such as flow velocity, are same at every point in the fluid. When a fluid flow is non-uniform, the flow parameters change with respect to space (Figure 3.2).
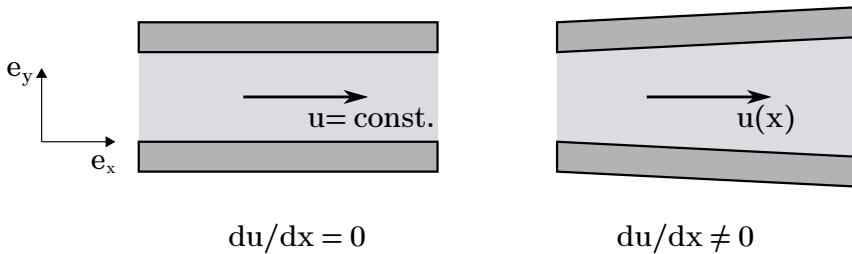
Figure 3.2: Uniform flow; flow velocity is constant because of constant diameter (left) and non-uniform flow; flow velocity varies due to variable diameter pipe (right).

The type of flow can also be classified as laminar and turbulent flow. In laminar flow, the fluid moves in smooth layers, in contrast to turbulent flow, in which the motion of fluid is not orderly (Figure 3.3).

In order to predict if the type of flow is laminar or turbulent, the Reynolds number (Re) is used

$$
Re < 2300 \text{ (laminar flow)}, \qquad Re > 2300 \text{ (turbulent flow)}.
\tag{3.13}
$$
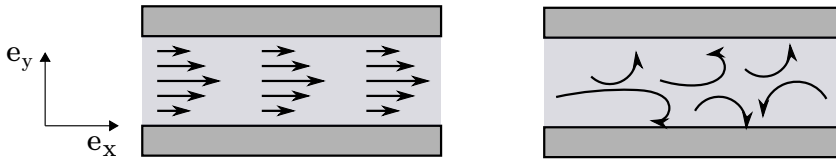
Figure 3.3: Laminar flow (left) and turbulent flow (right)

This number, which is a dimensionless quantity, is the ratio of inertial forces to viscous forces

$$Re = \frac{\rho \; u \; D}{\mu},$$ (3.14)

where μ is the dynamic viscosity and D is the pipe diameter.

3.3 The Basic Equations of Fluid Flow

Continuum Thermodynamics is based on three conservation laws of mechanics (balance of mass, linear momentum and angular momentum) and two laws of thermodynamics (the balance of energy and the imbalance of entropy). These laws apply without exceptions to all material bodies modeled within Continuum Thermodynamics. Hence, besides the kinematical relations, the distinction between solids and fluids lies in the supplemented constitutive laws, which model particular classes of materials. However, since the temperature has been kept constant during all experiments, the three laws of mechanics are sufficient for the description of mechanical processes.

3.3.1 Balance of Mass

The mass M of a reference body B can be written as

$$M(\mathbf{X}, t_0) = \int_B \rho_0 \; \mathrm{d}V,$$ (3.15)

where $\rho_0(\mathbf{X})$ is the mass density in the reference configuration $\mathbf{X}$ in the reference body (Figure 3.1). In the deformed body B_t, the mass $M(\mathbf{x}, t)$ can be expressed by

$$M(\mathbf{x}, t) = \int_{B_t} \rho(\mathbf{x}, t) \; \mathrm{d}v,$$ (3.16)

where $\rho(\mathbf{x}, t)$ is the density at the position $\mathbf{x}$. Balance of mass requires that Eqn. 3.15 should be equal to Eqn. 3.16, i.e. constant in time. The derivation of $M(\mathbf{X}, t_0) = M(\mathbf{x}, t)$ with respect to time can be determined by

$$\frac{\mathrm{d}}{\mathrm{d}t} \int_{B_t} \rho(\mathbf{x}, t) \, \mathrm{d}v = 0. \tag{3.17}$$

Thus, the principle of mass balance states that the mass of a material body does not change in time. Making use of the Reynolds' transport theorem [47], the balance of mass can be represented by

$$\frac{\mathrm{d}\rho}{\mathrm{d}t} =: \dot{\rho} = -\rho \, \mathrm{div}\mathbf{u}, \tag{3.18}$$

where $\mathbf{u}$ is the velocity vector. As mentioned above, if the fluid is incompressible (independent of space and time), ρ is constant, so that $\dot{\rho} = 0$. The balance of mass reduces to the continuity equation

$$\mathrm{div}\mathbf{u} = 0. \tag{3.19}$$

3.3.2 Balance of Linear Momentum
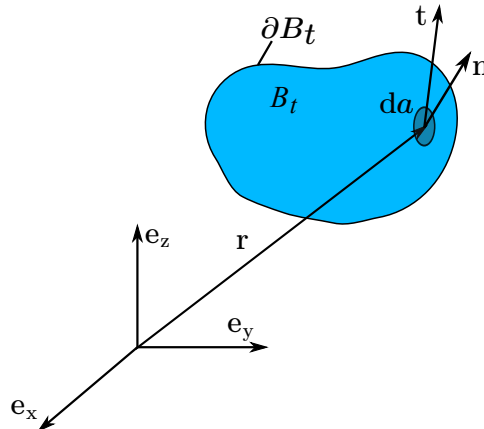
Figure 3.4: Traction vector $\mathbf{t}$ and the outward normal vector $\mathbf{n}$ of ∂B_t

Balance of linear momentum is the balance between the rate of change of linear momentum $\mathbf{J}(B_t)$ of fixed mass of the deformed body B_t and the sum of the forces acting on the body. Linear momentum is given as

$$\mathbf{J}(B_t) = \int_{B_t} \mathbf{u} \ \mathrm{d}m = \int_{B_t} \mathbf{u} \ \rho \ \mathrm{d}v. \tag{3.20}$$

The sum of the forces is

$$\mathbf{F} = \mathbf{F}_{\partial B_t} + \mathbf{F}_{B_t}, \tag{3.21}$$

where $\mathbf{F}_{\partial B_t} = \int_{\partial B_t} \mathbf{t} \ \mathrm{d}a$ are near field forces and $\mathbf{F}_{B_t} = \int_{B_t} \rho \ \mathbf{b} \ \mathrm{d}v$ are field forces. $\mathbf{t}$ is the surface traction and has a relation with the Cauchy stress tensor $\mathbf{T}$. This relation is called Cauchy's theorem

$$\mathbf{t} = \mathbf{T} \cdot \mathbf{n}, \tag{3.22}$$

where the vector $\mathbf{n}$ is the outward normal vector of ∂B_t (Figure 3.4).

3.3.3   Balance of Angular Momentum

Angular momentum is defined as the moment of the linear momentum. The balance of angular momentum is written as

$$\int_{B_t} \mathbf{r} \times (\mathbf{u} \ \rho) \ \mathrm{d}v = \int_{\partial B_t} \mathbf{r} \times \mathbf{t} \ \mathrm{d}a + \int_{B_t} \mathbf{r} \times (\rho \mathbf{b}) \ \mathrm{d}v, \tag{3.23}$$

where $\mathbf{r}$ is the position vector. From the balance of linear momentum, Eqn. 3.23 reduces to the requirement the Cauchy stress tensor must be symmetric $(\mathbf{T} = \mathbf{T}^T)$.

3.4   Constitutive Equations for Fluids

In engineering, a constitutive equation is a relation between two physical quantities, such as the relationship between the shear rate and the shear stress. In order to understand the background of the rheological experiments or the principle of rheometer, kinematic and dynamic quantities should be related to the flow of fluid. Material properties of fluid can be described by basic equations besides a set of constitutive equations

$$\mathbf{T} = \mathbf{T}_E - p \ \mathbf{I}, \tag{3.24}$$

where p is the pressure, which has a scalar value, and $\mathbf{I}$ is the second order unit tensor ($\mathbf{I} = \delta_{ij}\mathbf{e}_i \otimes \mathbf{e}_j$), with the Kronecker symbol $\delta_{ij} = 1$ for $i = j$ and $\delta_{ij} = 0$ for $i \neq j$. The components of the Cauchy stress tensor is

$$\mathbf{T} = \begin{bmatrix} T_{xx} & T_{xy} & T_{xz} \\ T_{yx} & T_{yy} & T_{yz} \\ T_{zx} & T_{zy} & T_{zz} \end{bmatrix} \mathbf{e}_i \otimes \mathbf{e}_j. \tag{3.25}$$

The extra stress tensor $\mathbf{T}_E$ is given by

$$\mathbf{T}_E = 2\ \eta(\mathrm{II})\ \mathbf{D}, \tag{3.26}$$

where $\mathbf{D}$ is the rate of deformation tensor and II is the second invariant. In order to derive $\mathbf{D}$ from the deformation gradient ($\mathbf{F} = \frac{\partial \mathbf{x}}{\partial \mathbf{X}}$) and the rate of change of the deformation gradient ($\dot{\mathbf{F}} = \frac{\mathrm{d}}{\mathrm{d}t}(\frac{\partial \mathbf{x}}{\partial \mathbf{X}})$), relation between the spatial velocity gradient ($\mathbf{L} = \mathrm{grad}\mathbf{u}$) and the rate of change of the deformation gradient is written by

$$\mathbf{L} = \mathrm{grad}\mathbf{u} = \frac{\partial \mathbf{u}}{\partial \mathbf{x}} = \frac{\partial \mathbf{u}}{\partial \mathbf{X}}\frac{\partial \mathbf{X}}{\partial \mathbf{x}} = \frac{\partial}{\partial \mathbf{X}}\frac{\partial \mathbf{X}}{\partial \mathbf{x}} = \frac{\mathrm{d}}{\mathrm{d}t}\left(\frac{\partial \mathbf{x}}{\partial \mathbf{X}}\right)\frac{\partial \mathbf{X}}{\partial \mathbf{x}} = \dot{\mathbf{F}} \cdot \mathbf{F}^{-1}. \tag{3.27}$$

$\mathbf{L} = L_{ij}\mathbf{e}_i \otimes \mathbf{e}_j$ is a second order tensor and can be decomposed into a symmetric part $\mathbf{D}$ and a skew-symmetric part $\mathbf{W}$ with

$$\mathbf{D} = \frac{1}{2}(\mathbf{L} + \mathbf{L}^T), \qquad \mathbf{W} = \frac{1}{2}(\mathbf{L} - \mathbf{L}^T). \tag{3.28}$$

From Eqn. 3.28, $\mathbf{L}$ is

$$\mathbf{L} = \mathbf{D} + \mathbf{W}, \tag{3.29}$$

where $\mathbf{W}$ is a skew-symmetric second order tensor $W_{ij}\mathbf{e}_i\otimes\mathbf{e}_j = -W_{ji}\mathbf{e}_j\otimes\mathbf{e}_i$ and is called rate of rotation tensor, and $\mathbf{D}$ is a symmetric second order tensor $D_{ij}\mathbf{e}_i \otimes \mathbf{e}_j = D_{ji}\mathbf{e}_j \otimes \mathbf{e}_i$.

3.5   Navier Stokes Equations

The Navier Stokes equations are equations of motion that describe the flow of compressible and incompressible fluids. The vector form of the Navier Stokes equation is

$$\rho \left(\frac{\partial \mathbf{u}}{\partial t} + \mathbf{u} \cdot \nabla \mathbf{u} \right) = -\nabla p + \nabla \cdot \mathbf{T} + \rho \mathbf{g}, \tag{3.30}$$

where $\mathbf{g}$ represents body acceleration.
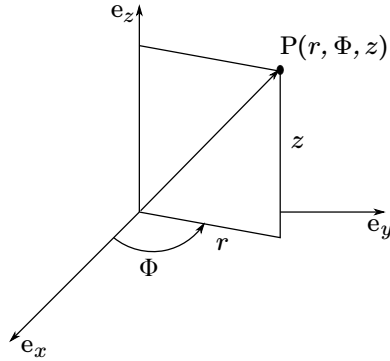
Figure 3.5: Cylindrical coordinate system ($x = r \cos \Phi$, $y = r \sin \Phi$, $z = z$)

In order to use the Navier Stokes equation in the cylindrical coordinate system, the relationship between the cylindrical basis vectors ($\mathbf{e}_r$, $\mathbf{e}_\Phi$, $\mathbf{e}_z$) and the cartesian basis vectors ($\mathbf{e}_x$, $\mathbf{e}_y$, $\mathbf{e}_z$) should be shown

$$\mathbf{e}_x = \cos \Phi \mathbf{e}_r - \sin \Phi \mathbf{e}_\Phi, \quad \mathbf{e}_y = \sin \Phi \mathbf{e}_r + \sin \Phi \mathbf{e}_\Phi, \quad \mathbf{e}_z = \mathbf{e}_z. \tag{3.31}$$
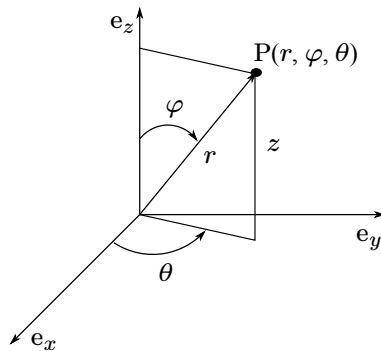
Figure 3.6: Spherical coordinate system ($x = r \sin \varphi \cos \theta$, $y = r \sin \varphi \sin \theta$, $z = r \cos \varphi$)

The equations of motion in spherical coordinates can be obtained by the mathematical transformation from the cartesian basis vectors ($\mathbf{e}_x$, $\mathbf{e}_y$, $\mathbf{e}_z$) to the spherical basis vectors ($\mathbf{e}_r$, $\mathbf{e}_\varphi$, $\mathbf{e}_\theta$)

$$\mathbf{e}_x = \cos\theta(\sin\varphi\mathbf{e}_r + \cos\varphi\mathbf{e}_\varphi) - \sin\theta\mathbf{e}_\theta,$$
$$\mathbf{e}_y = \sin\theta(\sin\varphi\mathbf{e}_r + \cos\varphi\mathbf{e}_\varphi) + \cos\theta\mathbf{e}_\theta, \tag{3.32}$$
$$\mathbf{e}_z = \cos\varphi\mathbf{e}_r - \sin\varphi\mathbf{e}_\varphi.$$

The three components form (in cartesian, cylindrical and spherical coordinate systems) of the Navier Stokes equation is shown in Appendix A.

Chapter 4

Basic Principles of the Rheology

4.1   Rheology of the Materials

The name of rheology derives from the Greek words "rheo" and "logia", which means "flow" and "study of", respectively. The term rheology was coined in the 1920s by Eugene C. Bingham, who was a professor at Lafayette College [15]. Rheology describes the deformation and flow of all types of matter (fluids or solids) under the influence of applied stress or forces. It can be applied to many different fields; cosmetics, chemical industry, oil drilling, etc.. Rheology is also used to asses the quality of the materials and helps to define the flow behavior of materials. It is very well known that materials have a behavior range from solid like "ideal solid" to liquid like "ideal fluid". Fluid can be classified into three different groups according to their flow behavior: Newtonian fluids, non-Newtonian fluids time dependent "rheopecty" and "thixotropic", and non-Newtonian fluids time independent "shear thinning" and "shear thickening". The most-known Newtonian fluid is water, whose viscosity (the shear resistance of an ideal fluid) does not change with the rate of flow. On the other hand, some fluids such as foams, chocolate, ketchup, and mayonnaise do not follow the Newtonian flow laws. In non-Newtonian fluids, viscosity is not constant and can even be time-dependent. The viscosity of rheopectic fluids increases under an applied shear rate or shear stress, whereas thixotropic fluids decrease in their viscosity as the shear rate increases. However, some fluids' viscosity decreases with increasing shear stress. Corn starch in water or sand in water can be taken as dilatant fluids, or shear thickening fluids and fluids like ketchup and blood have a different flow behvior than dilatant fluids. Their viscosities decrease when the shear rate increases and these fluids are also called pseudoplastic materials.

4.1.1   Liquid Foam

Liquid foams have a complex rheological behavior depending on their micro-structure and physicochemical constitution [92]. In order to understand the characteristics of liquid foam, some factors, such as bubble size and shape, gas volume fraction, ambient temperature, and pressure that influence its char-acteristics should be considered. A liquid foam includes dispersion of gas in a liquid, and the form of the bubbles is polyhedral. Generally, the bubbles range from 10 μm to 1 cm in diameter. Shaving foam exhibits very similar properties to liquid foam, which can flow and deform by application of shear forces. A shaving foam is generated from the following chemical ingredients: stearic acid ($C_{18}H_{36}O_2$), propane (C_3H_8), isobutane (C_4H_{10}), triethanolamine ($C_6H_{15}NO_3$), butane (C_4H_{10}), 2,6-Di-t-butyl-p-cresol (BHT) ($C_{15}H_{24}O$), wa-ter, Laureth-23 and sodium lauryl sulfate ($CH_3(CH_2)_{11}(OCH_2CH_2)_nOSO_3Na$) [9]. The surfactants play an important role in foam generation and its stabil-ity. Steric acid is used to produce soap. Laureth-23 and sodium lauryl sulfate stabilize the foam [9, 95]. Isobutane and propane are colorless and compressed gases, which have ability of aerosol propellants. In addition, triethanolamine is used as a neutralizer. The role of the water as a solvent is also important in foam generation. It dissolves the ingredients in the shaving foam. The concentration and type of surfactants used also influences the characteristics of shaving foam. The characteristics of shaving foam can be investigated by light microscopy, giving knowledge about micro-scale structure. The diameter of bubbles can be calculated and used for rheological experiments. Addition-ally, aging of foam (coarsening, coalescence and drainage) can be observed by microscopy, showing the deformation of foam bubbles. Many researchers have investigated rheological behavior of liquid foam with their microstructure and defined it as a non-Newtonian fluid [59, 64].

4.2   Rheometer and Rheological Experiments

4.2.1   History of Rheometer

Rheometry is used for the investigation of the rheological behavior of materials. It is used in many rheological experiments and gives us possibility to under-stand the flow behavior of materials (solid or fluid). The history of the rheome-ter starts with the viscometer, which is a very simple device used to measure the viscosity of fluids. The principles of the viscometer have been explained by MacMichael [70]: "The time required to produce a definite relative movement of the fluid particles under a given force. The force required to produce a defi-nite relative movement of the fluid particles in a given time". Barnes et al. [11] mentioned, in their historical review paper, that the earliest controlled-strain viscometer is the MacMichael controlled-strain viscometer, made in 1915. This

machine was manufactured by Eimer and Amend of Newyork, USA and has a 60 mm diameter disc and various cylindirical rotating cups with a rotational speed of 20 rpm. The rotational speed of this machine has been improved between the range of 10 to 38 rpm. Between 1909 and 1912, the controlled-stress viscometer was invented by Stormer and Searle [11]. However, these intruments were not controlled electrically and they only had some simple tools, such as "weight, pulleys and a stopwatch" to measure shear stress. In the 1968s, more elctronic devices were added to viscometers by Jack Deer and Peter Finlay. Then, around 1980, the viscometer became a modern instruments that was controlled by a micro-computer. Hence, rheological experiments can be performed automatically by this machine and the precision of the results has been greatly improved [11]. Nowadays, there are many different modern rheometers that are electrically controlled-stress or controlled-strain instruments [11, 17]. Modern rheometers have many different devices like air-bearing which make rheological experiments very simple. A modern rheometer has a high accuracy, wide shear-rate range and different geometry types, such as cone-plate, plate-plate, and cup & bob geometries. On the other hand, temperature and pressure of a sample can also be controlled by rheometer.

4.2.2   A Modern Rheometer

In our labrotory, we use a rotational rheometer, the Physica MCR 301 from Anton Paar GmbH (Figure 4.1), which works with the Physica RheoPlus software. It includes a configuration system (Toolmaster) that transfers geometry data and control parameters to the Rheoplus EPROM-based, for the measuring and temperature control systems.

Figure 4.1: The Physica MCR 301 rheometer with plate-plate device

A very rigid air bearing with synchronous motor is in this rheometer, which makes it possible to get low torque capabilities. For precise measurements of the angular deflection, a high-resolution optical encoder is used in combination with real time position control in oscillation. Therefore, there is no limit to the upper value of the amplitude. This rheometer has the highest efficiency and it is suitable for all Controlled Shear-Stress (CSS) and Controlled Shear-Rate (CSR) tests over large stress, strain, and frequency ranges (Table 4.1). On the other hand, the absolute torque of the upper tool (plate, cone and bob devices) can be calibrated due to the linear relationship between the electro-magnetic motor torque and the stator current.

Table 4.1: Specification of the Physica MCR 301 rheometer

Bearing	air	$-$
Torque rotation(min.)	0.05	μNm
Torque oscillation (min.)	0.01	μNm
Normal force range	$0.01 - 50$	N
Angular frequency (min.)	10^{-5}	rad/s
Angular frequency (max.)	628	rad/s
Temperature range	$123.15 - 1273.15$	°K
Torque rotation / oscillation (max.)	200	mNm

Table 4.1 shows some properties of the Physica MCR 301. As explained above, there are different types of geometries that can be used for different samples (suspensions, water, chocolate, honey, polymer etc.). Rheological experiments, such as flow curve tests, relaxation tests, creep tests, and oscillation tests, can be classified into two groups: amplitude sweep and frequency sweep tests. These tests can be performed by the Physica MCR 301 rheometer. Some special tests, such as the time temperature sweep test and Dynamical Mechanical Thermal Analysis (DMTA) can be also performed for solid polymers in the Physica MCR 301 rheometer; of course, in combination with other tools (Solid Rectangular Fixture "SRF").

Tests for Controlled Shear Rate (CSR)

The angular velocity ω is given as an input parameter to calculate the shear rate $\dot{\gamma}$, which depends on the plate-plate geometry gap distance h and the angular velocity ω. In addition, instead of the angular velocity ω when the range of shear rate $\dot{\gamma}$ for material is known, the shear rate $\dot{\gamma}$ can be set directly, and the effective viscosity η can be obtained as an output parameter (Figure 4.2). In controlled shear rate tests, the yield stress τ_y of a material cannot be measured directly. In order to determine the yield stress τ_y, different models, such as
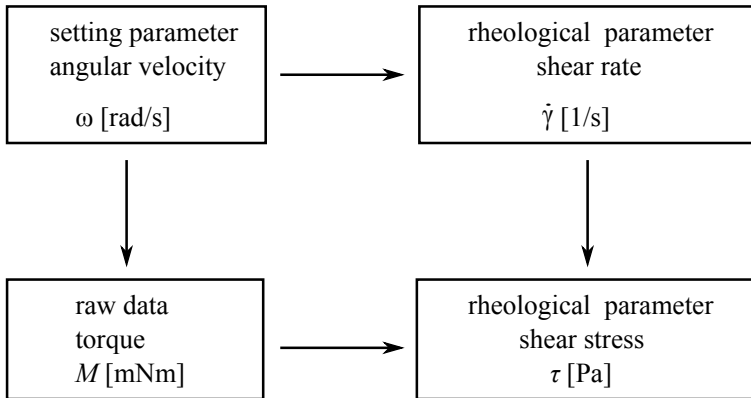
Figure 4.2: Rotational tests for controlled shear rate

Herschel-Bulkley, Casson etc., can be used by curve fitting [81].

Tests for Controlled Shear Stress (CSS)
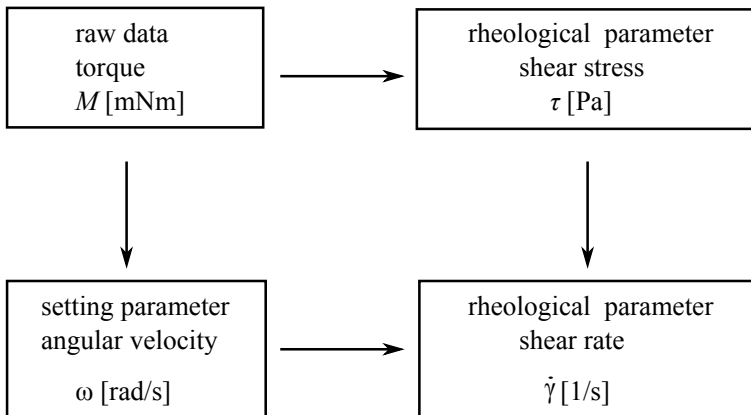
Figure 4.3: Rotational tests for controlled shear stress

The torque M determines the shear stress τ for rotational tests. It is also possible to give the shear stress τ as an input parameter directly. The shear rate $\dot{\gamma}$ is determined by the angular velocity ω with the appropriate measuring system factor, (cf. Figure 4.3). The cotrolled shear stress test can be used to observe the yield stress of a material directly.

4.2.3 Basic Terms of Rheometry
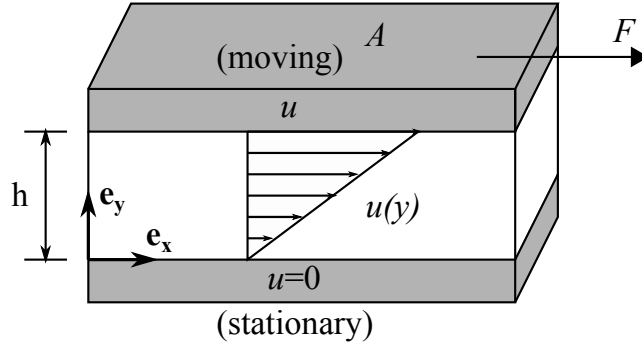
Figure 4.4: Simple shear flow. u is the velocity in the $\mathbf{e}_x$ direction; maximum velocity at the top plate and a velocity of zero at the bottom plate.

The parallel plate model is the simplest model to explain the basic terms of rheometry easily. As can be seen from Figure 4.4, two plates are used for parallel plate rheometer; the bottom plate is fixed and the top plate is moved by a force. The layer (lamina) next to the stationary (bottom) plate is stationary and it moves with the moving plate. In this case, the velocity of flow is zero at the bottom plate and is at its maximum at the top of the plate due to the no-slip condition. Therefore, the fluid closest to the wall moves at the velocity of the wall [10]. To measure any fluid flow by rheometer, the fluid is put over the bottom plate, and the top plate moves downward, touching the sample. The movement should continue until the measure point (distance) is reached. The distance between plates, which is filled with sample, is called the gap distance and is symbolized by h [mm]. In rheometry, this phenomenon is described by the viscosity. It is described in terms of shear stress τ [Pa] and shear rate $\dot{\gamma}$ [s^{-1}]. The term shear stress is the ratio of applied force F [N] to the movement of the layer of a given area A [mm^2]

$$\tau = \frac{F}{A}.\tag{4.1}$$

Shear rate (rate of deformation) is the movement of the fluid between layers

$$\dot{\gamma} = \frac{u}{h},\tag{4.2}$$

where u is the velocity in the $\mathbf{e}_x$ direction and h is the gap distance between the plates. In laminar (a fluid moves in parallel layers) and ideal-viscous flow, the velocity difference $\mathrm{d}u$ between neighbouring layers and the thickness

difference dh of all the layers are constant, which means that the shear rate is constant across the whole shear gap

$$\dot{\gamma} = \frac{\mathrm{d}u}{\mathrm{d}h} = const. \tag{4.3}$$

Generally, shear tests are performed by using a rotational rheometer. In contrast to the parallel plate rheometer, the movement of the top plate is rotational. In order to determine the dynamic viscosity η, the shear stress, τ, is divided by the shear rate $\dot{\gamma}$

$$\eta = \frac{\tau}{\dot{\gamma}}. \tag{4.4}$$

The typical dynamic viscosities of water, petrol, and honey are 1 mPas, 0.65 mPas, and 10^4 mPas at 293°K, respectively. In addition, the kinematic viscosity [m^2/s], which is related to the dynamic viscosity through the density ρ [kg/m^3] of the material, can be calculated by

$$\mu = \frac{\eta}{\rho}. \tag{4.5}$$

There are some factors, such as temperature, pressure, and shear rate, that affect viscosity. When a liquid heats up, the heating energy causes a disconnection of binding between the molecules. This phenomenon allows the liquid to become more fluid and its viscosity decreases. For example, when we put a visco-elastic fluid like nutella in the refrigerator, it gets hard and its viscosity increases with decreasing temperature. Contrary to the influence of temperature, effect of the pressure can be neglected for viscosity. The reason for this is that fluids are almost incompressible at low or medium pressures. On the other hand, for most liquids, the viscosity increases with increasing pressure. This fact can be explained by the decreased amount of free volume in the internal structure due to compression [81]. The shear rate also affects the viscosity of most fluids, especially non-Newtonian fluids.

4.2.4 Types of Geometry

Cone-Plate Geometry

Cone-plate geometry has a cone-type upper tool and plate-type lower tool (Figure 4.5). The cone part is rotating, while the plate part is stationary. The cone part can be either truncated or untruncated. Generally, truncated cones are used to overcome specific challenges. Firstly, an untruncated cone apex can
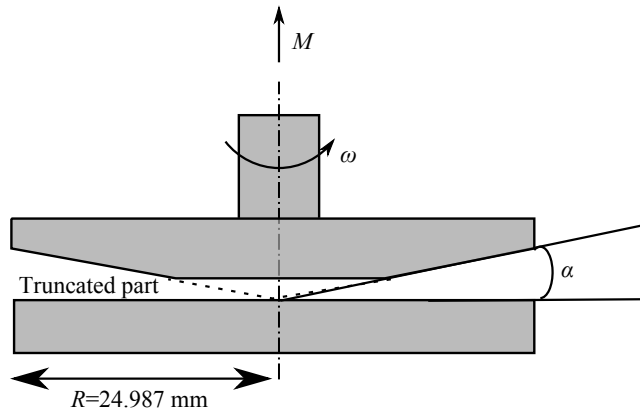
Figure 4.5: Cone-plate geometry

be easily damaged and the particles, which are inside the suspensions, may be at the lower plate at the small gap of the center. Therefore, we use truncated cone parts with a truncation of 208 μm. For truncated cone-plate geometry, the gap distance is determined by the imaginary cone apex in the measurement position. The cone angle α and diameter ($D=2R$) of it are exactly 1.993° and 49.974 mm, respectively. If the angle of the cone is less than 3°, it results in a uniform shear rate in the gap due to the independence of radial position [46].

On the other hand, cone-plate geometry has some advantages in rheological experiments. They are cleaned and filled easily and can be used for low sample volumes. However, they are only suitable for homogeneous samples, such as gels, concentrated suspensions etc.
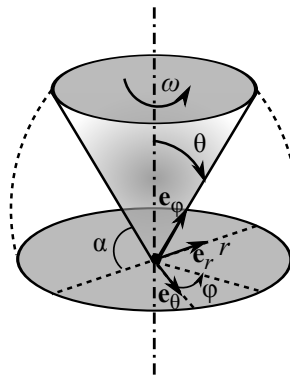
Figure 4.6: Schematic of cone-plate geometry [113]

The schematic of cone-plate geometry with the cone angle α and the angular velocity ω was shown in Figure 4.6. The proper coordinate system is the spherical coordinate for the cone-plate geometry [71]. The spherical coor-

dinates are denoted as r, θ, φ and usually used for the cone-plate geometry. It is assumed that the flow between the cone-plate is steady, laminar and isothermal and the body forces are negligible. The velocity of the cone-plate in spherical coordinates is

$$\mathbf{u} = u_r \mathbf{e}_r + u_\theta \mathbf{e}_\theta + u_\varphi \mathbf{e}_\varphi. \tag{4.6}$$

The zero and non-zero velocity components of the cone are given by

$$u_r = 0, \qquad u_\theta = 0, \qquad u_\varphi \neq 0. \tag{4.7}$$

The boundary conditions on the velocity field are

$$u_\varphi(\frac{\pi}{2}) = 0, \qquad u_\varphi(\frac{\pi}{2} - \alpha) = \omega r \sin(\frac{\pi}{2} - \alpha) = \omega r \cos \alpha, \tag{4.8}$$

where $\cos \alpha \approx 1$ for $\alpha < 3°$. In spherical coordinates, the velocity gradient is

$$\operatorname{grad}\mathbf{u} = \begin{bmatrix} \frac{\partial u_r}{\partial r} & \frac{\partial u_r}{\partial \theta} & \frac{\partial u_r}{\partial \varphi} \\[2mm] \frac{\partial u_\theta}{\partial r} & \frac{\partial u_\theta}{\partial \theta} & \frac{\partial u_\theta}{\partial \varphi} \\[2mm] \frac{\partial u_\varphi}{\partial r} & \frac{\partial u_\varphi}{\partial \theta} & \frac{\partial u_\varphi}{\partial \varphi} \end{bmatrix} \mathbf{e}_i \otimes \mathbf{e}_j = \begin{bmatrix} 0 & 0 & 0 \\ 0 & 0 & 0 \\ 0 & \dot{\gamma} & 0 \end{bmatrix} \mathbf{e}_i \otimes \mathbf{e}_j. \tag{4.9}$$

The rate of deformation tensor has the form

$$\mathbf{D} = \frac{1}{2} \begin{bmatrix} 0 & 0 & 0 \\ 0 & 0 & \dot{\gamma} \\ 0 & \dot{\gamma} & 0 \end{bmatrix} \mathbf{e}_i \otimes \mathbf{e}_j. \tag{4.10}$$

The component of the deformation tensor ($D_{\theta\varphi} = D_{\varphi\theta}$) is

$$D_{\theta\varphi} = D_{\varphi\theta} = \frac{1}{2} \left(\frac{\sin\theta}{r} \frac{\partial}{\partial \theta} \left(\frac{u_\varphi}{\sin\theta} \right) + \underbrace{\frac{1}{r\sin\theta} \frac{\partial u_\theta}{\partial \varphi}}_{=0} \right). \tag{4.11}$$

From Eqn. 4.11, the shear rate in spherical coordinates is given by

$$\dot{\gamma} = 2D_{\varphi\theta} = 2\frac{1}{2}\left(\frac{\sin\theta}{r}\frac{\partial}{\partial\theta}\left(\frac{u_{\varphi}}{\sin\theta}\right)\right). \tag{4.12}$$

The equations of motion in spherical coordinates with the components (r, θ and φ) for the cone-plate flow reduce to

$$\rho\frac{(u_{\varphi})^2}{r} = \frac{1}{r^2}\frac{\partial(r^2\tau_{rr})}{\partial r} - \frac{\tau_{\theta\theta} + \tau_{\phi\phi}}{r}, \tag{4.13}$$

$$-\rho\frac{(u_{\varphi})^2}{r} = \frac{1}{r\sin\theta}\frac{\partial(\tau_{\theta\theta}\sin\theta)}{\partial\theta} - \frac{\tau_{\varphi\varphi}\cot\theta}{r}, \tag{4.14}$$

$$0 = \frac{1}{r}\frac{\partial\tau_{\theta\varphi}}{\partial\theta} + \frac{2}{r}\cot\theta\ \tau_{\theta\varphi}. \tag{4.15}$$

The third component of the equations of motion (Eqn. 4.15) can be integrated to give

$$\tau_{\theta\varphi} = \frac{C_1}{\sin^2\theta}, \tag{4.16}$$

where C_1 is a constant parameter of integration. The constant parameter can be expressed by the applied torque on a cone-plate surface. A torque balance on the cone-plate surface is determined by

$$M = \int_0^{2\pi}\int_0^R r^2\ \tau_{\theta\varphi}\ dr\ d\varphi. \tag{4.17}$$

The shear stress $\tau_{\theta\varphi}$ is

$$\tau_{\theta\varphi} = C_1 = \tau_{\theta\varphi}(\theta)\sin^2\theta. \tag{4.18}$$

From Eqn. 4.17, the constant integration parameter is

$$C_1 = \frac{3M}{2\pi r^3}\sin^2\theta. \tag{4.19}$$

Eqn. 4.8 is inserted in the shear rate (Eqn. 4.12)

$$\dot{\gamma} = \frac{1}{r}\frac{\partial}{\partial \theta}(\frac{\omega r}{1}), \tag{4.20}$$

where $\sin\theta = 1$ at small angles. In order to determine a good approximation, the shear rate is given by

$$\dot{\gamma} = \frac{1}{r}\frac{\partial}{\partial \theta}(\omega \ r \ (\frac{\frac{\pi}{2} - \theta}{\alpha})). \tag{4.21}$$

From Eqn. 4.21, the shear rate is

$$\dot{\gamma} = \frac{\omega}{\alpha}. \tag{4.22}$$

Plate-Plate Geometry
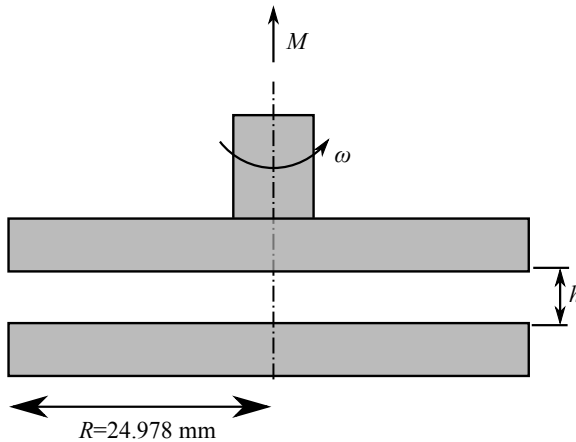
Figure 4.7: Plate-plate geometry

The plate-plate geometry working principle is similar to that of cone-plate geometry. The upper plate is rotating, whilst the lower plate remains stationary (Figure 4.7). This used system has two parallel plates, each 49.956 mm in diameter ($D = 2R$). The gap distance h of the plate-plate geometry is not constant and depends on the particles contained in the material. On the other hand, the gap distance should be at least five times greater than the diameter of particles in the sample. For a rheological test of the shaving foam, the mean bubble diameter $\bar{D}$ of 51.8 μm, which is shown in Chapter 5, should be considered for the gap distance. It cannot be set randomly. For instance, when the gap distance of the plate-plate geometry is setting for shaving foam, the gap distance is

$$h \geq 5\bar{\text{D}}. \tag{4.23}$$

From Eqn. 4.23, the gap distance should be at least 259 μm for shaving foam. This phenomenon shows that the microstructure of the material affects the rheological behavior of foams on a macro-scale. For plate-plate geometry, the shear rate varies from zero, at the center of the upper plate, to its maximum at the outer diameter D.

The advantage of the plate plate system is that it can be filled and cleaned easily. The disadvantage of this system is the shear rate. In contrast to the cone plate system, the shear rate depends on the gap distance. Furthermore, this system is limited to small sample sizes.

The plate-plate flow with the continuum based theorie can be explained in cylindrical coordinates system.
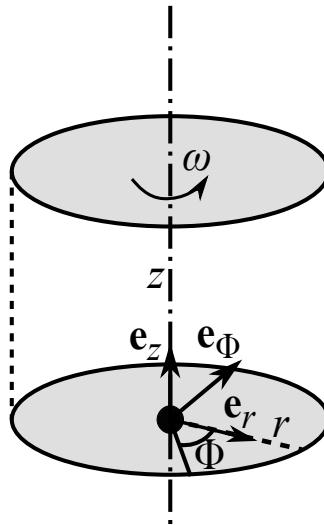
Figure 4.8: Schematic of plate-plate geometry with cylindrical coordinates

As seen in Figure 4.8, the plate plate geometry is shown in a cylindrical coordinate system which has the axes Φ, z and r. The plate-plate flow is assumed that steady, laminar and isothermal. In addition, the body forces are also negligible. The velocity of the plate-plate geometry can be written with respect to cylindrical coordinates as,

$$\mathbf{u} = u_\Phi \mathbf{e}_\Phi + u_z \mathbf{e}_z + u_r \mathbf{e}_r. \tag{4.24}$$

Fluid between plate-plate geometry flows in the axis of Φ direction, thus the non-zero and zero components of the velocity are

$$u_\Phi \neq 0, \qquad u_z = 0, \qquad u_r = 0. \qquad (4.25)$$

In cylindrical coordinates, the velocity gradient is

$$\text{grad}\mathbf{u} = \begin{bmatrix} \frac{\partial u_\Phi}{\partial \Phi} & \frac{\partial u_\Phi}{\partial z} & \frac{\partial u_\Phi}{\partial r} \\[2mm] \frac{\partial u_z}{\partial \Phi} & \frac{\partial u_z}{\partial z} & \frac{\partial u_z}{\partial r} \\[2mm] \frac{\partial u_r}{\partial \Phi} & \frac{\partial u_r}{\partial z} & \frac{\partial u_r}{\partial r} \end{bmatrix} \mathbf{e}_i \otimes \mathbf{e}_j = \begin{bmatrix} 0 & \dot{\gamma} & 0 \\[2mm] 0 & 0 & 0 \\[2mm] 0 & 0 & 0 \end{bmatrix} \mathbf{e}_i \otimes \mathbf{e}_j. \qquad (4.26)$$

The rate of deformation tensor for the velocities in cylindrical coordinates is

$$\mathbf{D} = \frac{1}{2} \begin{bmatrix} 0 & \dot{\gamma} & 0 \\[2mm] \dot{\gamma} & 0 & 0 \\[2mm] 0 & 0 & 0 \end{bmatrix} \mathbf{e}_i \otimes \mathbf{e}_j. \qquad (4.27)$$

From the deformation tensor, the non-zero component $D_{\Phi z} = D_{z\Phi}$ is

$$D_{\Phi z} = D_{z\Phi} = \frac{1}{2} \left(\frac{\partial u_\Phi}{\partial z} + \underbrace{\frac{1}{r}\frac{\partial u_z}{\partial \Phi}}_{=0} \right). \qquad (4.28)$$

The shear rate can be determined by

$$\dot{\gamma} = 2D_{\Phi z} = 2\frac{1}{2}\left(\frac{\partial u_\Phi}{\partial z} \right). \qquad (4.29)$$

Integration of Eqn. 4.29 can be written as

$$u_\Phi = \dot{\gamma} z + C_1, \qquad (4.30)$$

where C_1 is the constant of integration. As it is known, in order to determine the rheological parameters (shear rate, shear stress etc.) simply, "no slip" boundary condition is assumed for the plate-plate flow. In this study, we consider two boundary conditions: boundary condition without slip effect and boundary condition with slip effect. The boundary condtions are also related

with the rheological experiments which were shown in Chapter 5 and 6. For
the rheological experiments, the plate-plate without sandpaper (slip) and with
sandpaper no slip) were used to compare the results in two boundary condi-
tions. Therefore, two boundary condtions are also handled analytically for the
plate-plate flow.

When we consider "no slip" boundary condition for the plate-plate flow,
$u_\Phi = 0$ at the bottom plate $z = 0$, thus the constant parameter C_1 is equal to
zero from Eqn. 4.30

$$C_1 = 0. \tag{4.31}$$

The velocity u_Φ can be written by

$$u_\Phi = \dot{\gamma} h, \tag{4.32}$$

where z is equal to h. From Eqn. 4.32, the apparent shear rate ($\dot{\gamma}_{app}$) is
expressed as

$$\dot{\gamma}_{app} = \frac{\omega r}{h}. \tag{4.33}$$

The plate-plate flow with slip effect was investigated by Yoshimura et al.
[121] and they draw the figure of the slip effect for the plate-plate flow. In
order to understand the slip velocity (u_s) obviously, the sketch of the slip
effect (Figure 4.9) was taken to show it for the plate-plate flow.
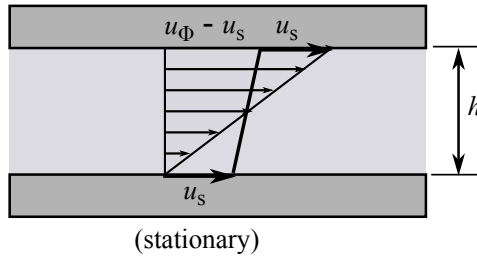
Figure 4.9: Plate-plate flow with slip effect [121]

From Eqn. 4.30, the constant parameter C_1 was determined at slip bound-
ary condition,

$$z = 0, \qquad u_\Phi = u_s, \qquad C_1 = u_s. \tag{4.34}$$

If C_1 is substituted in Eqn. 4.30, the equation will be

$$u_\Phi = \dot{\gamma}z + u_s. \tag{4.35}$$

The velocity (u_Φ) is

$$u_\Phi - u_s = \dot{\gamma}h + u_s, \tag{4.36}$$

where z is equal to h. From Eqn 4.36, the velocity is written by

$$\omega r = \dot{\gamma}h + 2u_s. \tag{4.37}$$

Therefore, the apparent shear rate with slip effect can be expressed as

$$\dot{\gamma}_{app} = \dot{\gamma}(\tau_{\Phi z}) + \frac{2u_s(\tau_{\Phi z})}{h}. \tag{4.38}$$

The equations of motion in cylindrical coordinates with the components (Φ, z and r) for the plate-plate flow reduce to

$$\frac{\partial \tau_{\Phi z}}{\partial z} = 0, \tag{4.39}$$

$$\frac{\partial \tau_{zz}}{\partial z} = 0, \tag{4.40}$$

$$-\rho\frac{u_\Phi^2}{r} = \frac{1}{r}\frac{\partial}{\partial r}(r\ \tau_{rr}) - \frac{\tau_{\Phi\Phi}}{r}. \tag{4.41}$$

In order to determine the shear stress ($\tau_{\Phi z}$), the first component of the equation of motion (Eqn. 4.39) in cylindrical cordinates was integrated

$$\tau_{\Phi z} = C_2. \tag{4.42}$$

The shear stress can be a function of shear rate ($\dot{\gamma}$) [71]

$$\tau_{\Phi z} = \tau_{\Phi z}(\dot{\gamma}). \tag{4.43}$$

The torque M can be written as

$$M = 2\pi \int_0^R r^2 \ \tau_{\Phi z} \ \mathrm{d}r. \tag{4.44}$$

The variable of integration from r to $\dot{\gamma}_{app}$ can be expressed as

$$M = \frac{2\pi R^3}{\dot{\gamma}_{app}^3} \int_0^{\dot{\gamma}_{app}} \tau_{\Phi z}(\dot{\gamma}_{app}) \ \mathrm{d}\dot{\gamma}_{app}. \tag{4.45}$$

Eqn. 4.45 is differentiated by using Leibniz rule [35] and obtained

$$\tau_{\Phi z} = \frac{M}{2\pi R^3} \left[3 + \frac{\mathrm{d}\ln M}{\mathrm{d}\ln\dot{\gamma}_{app}} \right]. \tag{4.46}$$

Cup and Bob Geometry

In cup and bob geometry, measuring systems have two measuring principles; the Searle principle and the Couette principle. The Searle principle depends on the rotating bob while the cup remains constant. In contrast, the cup rotates while the bob is stationary for the Couette principle. In this study, we are using the cup and bob geometry that works with the Searle principle. Figure 4.10 shows the cup and bob measuring system with bob radius R_i, cup radius R_e, gap distance h and gap length L.
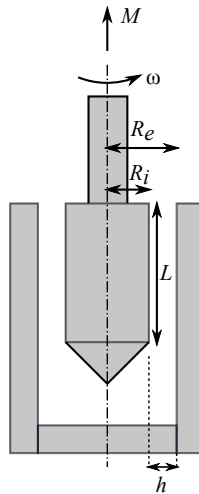
Figure 4.10: Schematic representation of Cup and bob measuring system

In order to determine shear rate for the cup and bob geometry (coaxial cylinder measuring system), the velocity gradient across the gap should be considered cautiously. For this measuring system, the velocity gradient is non-linear and the size of the gap should be small for non-Newtonian fluids.
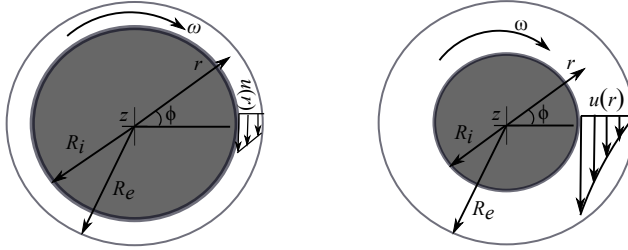
Figure 4.11: The ratio of radii influencing the non-linearity of the speed drop across the gap of Cup and bob measuring system [81]

When the gap size is large, the velocity gradient of the non-Newtonian fluids becomes much more non-linear than Newtonian fluids (Figure 4.11). Therefore, the gap size should be small for cup and bob geometry. In order to delimit the gap size, the ratio of radii is specified through:

$$\frac{R_e}{R_i} \leq 1.08, \tag{4.47}$$

where $R_e = 13.5$ mm and $R_i = 12.5$ mm in the ISO 3219. For the cup and bob geometry, the flow of a fluid is described in cylindrical coordinates system. The flow is assumed steady, laminar and isothermal. Eqn. 4.26 can also be taken as the velocity of the cup and bob geometry. The components of the velocity are

$$u_\Phi \neq 0, \qquad u_z = 0, \qquad u_r = 0. \tag{4.48}$$

In cylindrical coordinates, the velocity gradient can be written as,

$$\text{grad}\mathbf{u} = \begin{bmatrix} \frac{\partial u_\Phi}{\partial \Phi} & \frac{\partial u_\Phi}{\partial z} & \frac{\partial u_\Phi}{\partial r} \\ \frac{\partial u_z}{\partial \Phi} & \frac{\partial u_z}{\partial z} & \frac{\partial u_z}{\partial r} \\ \frac{\partial u_r}{\partial \Phi} & \frac{\partial u_r}{\partial z} & \frac{\partial u_r}{\partial r} \end{bmatrix} \mathbf{e}_i \otimes \mathbf{e}_j = \begin{bmatrix} 0 & 0 & \dot{\gamma} \\ 0 & 0 & 0 \\ 0 & 0 & 0 \end{bmatrix} \mathbf{e}_i \otimes \mathbf{e}_j. \tag{4.49}$$

From the velocity gradient, the rate of deformation tensor is

$$\mathbf{D} = \frac{1}{2} \begin{bmatrix} 0 & 0 & \dot{\gamma} \\ 0 & 0 & 0 \\ \dot{\gamma} & 0 & 0 \end{bmatrix} \mathbf{e}_i \otimes \mathbf{e}_j. \tag{4.50}$$

The non-zero component of the deformation tensor $D_{\Phi r} = D_{r\Phi}$ is

$$D_{\Phi r} = D_{r\Phi} = \frac{1}{2} \left(r \frac{\partial}{\partial r} (\frac{u_\Phi}{r}) + \underbrace{\frac{1}{r} \frac{\partial u_r}{\partial \Phi}}_{=0} \right). \tag{4.51}$$

The shear rate can be determined by the deformation tensor

$$\dot{\gamma} = 2 D_{\Phi r} = 2 \frac{1}{2} \left(r \frac{\partial}{\partial r} \left(\frac{u_\Phi}{r} \right) \right). \tag{4.52}$$

Eqn. 4.52 can be written in the form of

$$\dot{\gamma} = r \frac{\partial \omega}{\partial r}, \tag{4.53}$$

where $u_\Phi = \omega r$. In order to determine the shear stress of the cup and bob geometry, the equations of motion in cylindrical coordinates with the components (Φ, $z = 0$ and r) reduce to

$$0 = \frac{1}{r^2} \frac{\partial (r^2 \, \tau_{r\Phi})}{\partial r}, \tag{4.54}$$

$$-\rho \frac{u_\Phi^2}{r} = \frac{1}{r} \frac{\partial (r \, \tau_{rr})}{\partial r} - \frac{\tau_{\Phi\Phi}}{r}. \tag{4.55}$$

Eqn. 4.54 was integrated to determine the shear stress between the cup and bob

$$\tau_{r\Phi} = \frac{C_1}{r^2}, \tag{4.56}$$

where C_1 is the integration constant and can be obtained by a torque balance. As it is discussed before, the bob (inner cylinder) is rotating, while

the cup (outer cylinder) is stationary. Thus, the torque balance for inner cylinder is

$$\frac{M_i}{R_i} = \tau_{r\Phi} \ 2\pi \ L \ R_i \tag{4.57}$$

and the shear stress is equal to

$$\tau_{r\Phi} = \frac{M}{2\pi \ L \ R_i^2}. \tag{4.58}$$

In this measuring system, relatively large sample volumes (16-19 ml) are needed. This system is also difficult to clean; however, it can be used for low viscosity materials and has a greater sensitivity due to its large surface area.

4.2.5 Rheological Experiments

Flow Curve Test

The rotational experiment is conducted by rotating the upper plate according to the given range of shear rate. During the experiment, the sample is subjected to increasing and decreasing shear rates. Viscosity is then calculated using the respective torque and shear stress values according to $\eta = \frac{\tau}{\dot{\gamma}}$. Hence, the flow type of the sample is obtained by performing the flow curve experiment. A typical flow curve test is conducted with shear stress-shear rate or viscosity-shear rate curves.

Oscillation Test

Two methods, the dynamic and the static method, are used for determining viscoelastic behavior of materials. For the dynamic method, the harmonically varying stress or strain is applied on the system. The dynamic method includes oscillation tests (amplitude sweep and frequency sweep tests), whereas the static method includes creep and relaxation tests. The static method involves the imposition of a step change in the stress or strain and the observation of the subsequent development of the strain or stress as a function of time [12]. By performing an oscillation test, the sinusoidal oscillation stress or strain is determined while fixed/varying period stress or strain is applied to the sample. Through this method, it is possible to obtain information about the dynamic behavior (viscoelastic fluid, idealelastic, and etc.) of the material.

For an oscillation controlled strain test procedure, a preset strain γ_0 is given as an input parameter (Figure 4.12). If a sinusoidal strain is applied, the shear strain is a function of time and it can be written as
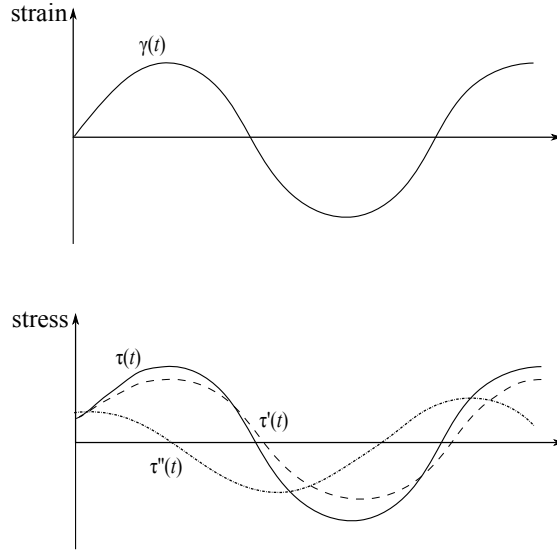
Figure 4.12: Decomposition of the measured stress into an in phase $(\tau'(t))$ and out of phase $(\tau''(t))$ component [36]

$$\gamma(t) = \gamma_0 \sin(\omega t), \tag{4.59}$$

where γ_0 is the strain amplitude and ω is the frequency. The responding shear stress is measured as a function of time with a phase angle δ

$$\tau(t) = \tau_0 \sin(\omega t + \delta). \tag{4.60}$$

The responding shear stress can be decomposed into two harmonic responses with the same frequency, one in phase with the strain response $(\sin \omega t)$, and the other out of phase $(\pi/2)$ with the strain response $(\cos \omega t)$ [36]

$$\tau(t) = \tau'(t) + \tau''(t) = \tau' \sin(\omega t) + \tau'' \cos(\omega t). \tag{4.61}$$

The applied shear strain $\gamma(t)$ can be written as imaginary part of a complex strain γ^* from the Euler's relation $(\exp(i\omega t) = i \sin(\omega t) + \cos(\omega t))$ with $i = \sqrt{-1}$

$$\gamma^* = \gamma \exp\left(i\omega t\right) = \gamma \cos \omega t + i\gamma \sin \omega t, \tag{4.62}$$

where $\gamma \sin \omega t = \gamma(t) = \text{Im}[\gamma \exp\left(i\omega t\right)]$.

From the Euler's formula, the in phase shear stress response can be written as imaginary part $\tau^{'}(t) = \tau^{'} \sin \omega t = \text{Im}[\tau^{'} \exp(i\omega t)]$, while the out of shear stress response can be expressed as real part $\tau^{''}(t) = \tau^{''} \cos \omega t = \text{Re}[\tau^{''} \exp(i\omega t)]$. The complex stress function and complex strain function are

$$\gamma^* = \gamma \exp(i\omega t), \qquad\qquad \tau^* = \tau \exp(i(\omega t + \delta)). \qquad (4.63)$$

The ratio of the complex stress and complex strain provides the complex modulus

$$G^* = \frac{\tau^*}{\gamma^*} = \frac{\tau \exp(i(\omega t + \delta))}{\gamma \exp(i\omega t)} = \frac{\tau}{\gamma} \exp(i\delta) = \frac{\tau}{\gamma} \cos \delta + i\frac{\tau}{\gamma} \sin \delta. \qquad (4.64)$$

From Eqn. 4.64, the complex modulus is divided into two parts, the real part is the storage modulus G' and the imaginary part is the loss modulus G''

$$G^* = G' + iG''. \qquad (4.65)$$

In order to get information about the elasticity of the material, the storage modulus is considered. On the other hand, the loss modulus accounts for the viscosity of the material. The storage modulus is the ability of the material to store elastic energy

$$G' = \frac{\tau}{\gamma} \cos \delta. \qquad (4.66)$$

The loss modulus is the ability of the material to dissipate energy

$$G'' = \frac{\tau}{\gamma} \sin \delta. \qquad (4.67)$$

The ratio between the loss modulus and storage modulus gives the loss factor $\tan \delta$

$$\tan \delta = \frac{G''}{G'}. \qquad (4.68)$$

If the loss factor is around 1, the material is regarded as viscoelastic, meaning that it has both viscous and elastic properties at the same time (Figure 4.13, c). Contrarily, if the loss factor is equal to 0, the material becomes ideal-elastic (Figure 4.13, a). Having infinity for the loss factor implies ideal viscous fluid (Figure 4.13, b).
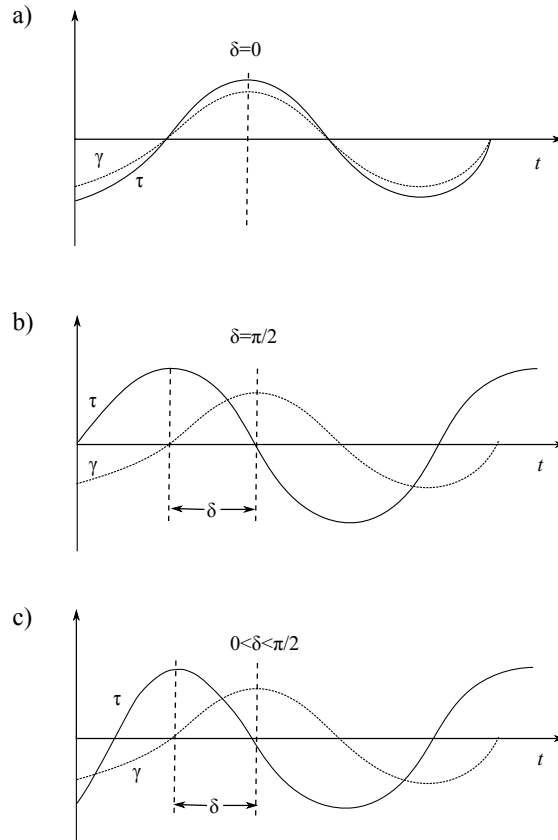
Figure 4.13: (a) Harmonic tests of an ideal elastic solid , (b) a Newtonian fluid and (c) a viscoelastic fluid [104]

Amplitute Sweep Test

The Amplitude Sweep test (AS) is applied to the sample with a varying range of deformation (amplitude) at constant frequency. In order to explain the amplitude sweep, an example test of shaving foam (Gillette Classic Sensitive, Procter & Gamble UK) is shown in Figure 4.14.

For the analysis, the storage modulus G' and the loss modulus G'' are plotted against the deformation γ. When the storage and loss modulus are constant at low deformation, the sample structure is not destroyed and this region is called the linear viscoelastic region (LVE). At the end of this region the storage modulus starts to decrease and the loss modulus becomes greater than the storage modulus. In Figure 4.14, the storage modulus is greater than the loss modulus in the LVE region, meaning that the shaving foam behaves like a viscoelastic solid. On the contrary, if the loss modulus is greater than the storage modulus in the LVE region, the sample has viscoelastic fluid properties.
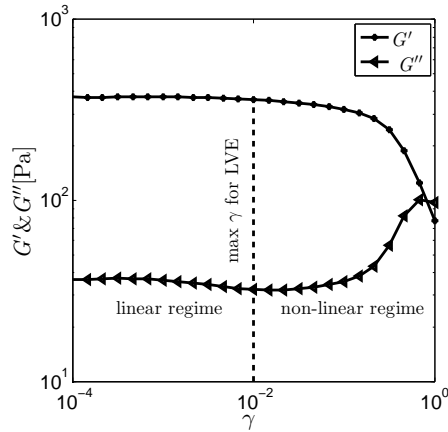
Figure 4.14: Storage and loss moduli are dependent on the shear rate obtained from the amplitude sweep test. The so-called LVE is characterized by the vertical dashed line.

A decrease in storage modulus can be explained by an increase of the applied stress. When the applied stress reaches its highest value, disruption of structure appears. That is the reason why the storage modulus decreases and becomes smaller than the loss modulus. In addition, the yield point can be determined by the amplitude sweep test. The intersection point of the two moduli gives the yield stress, when the storage and loss modulus are plotted with respect to the shear stress.

Frequency Sweep Test

The amplitude sweep test provided the critical deformation point observed as the intersection point of linear and non-linear viscoelastic areas. As the critical deformation point was found in linear regime and carried out in the frequency sweep test, the material behavior can be observed in the safe range.

For the frequency sweep test, the amplitude is given as constant with varying frequency. Therefore, the amplitude sweep test is very important to perform before the frequency sweep test. Storage and loss moduli are plotted with respect to frequency. This test can be performed at different temperatures and the results of storage or loss moduli can be superimposed to determine master curves. The data of storage and loss moduli, which are measured at different temepratures, can be horizontally shifted to generate master curves. Thus, the master curve shows the time dependence (in terms of frequency) of the material. However, the frequency test with varying temperature is used es-
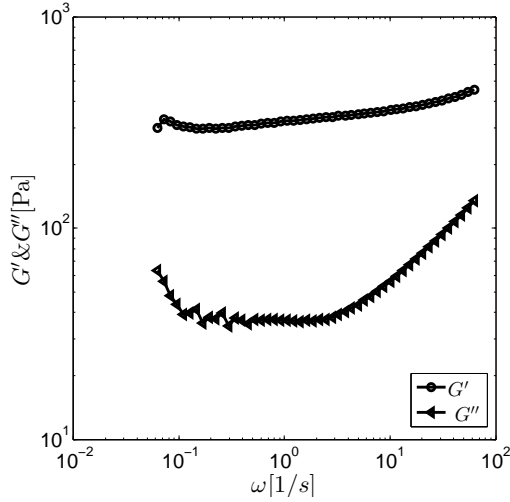
Figure 4.15: Frequency sweep test of the shaving foam

pecially for polymer melts. Performing the frequency sweep test on shaving foam yielded storage and loss modulus vs. angular frequency curves, as seen in Figure 4.15. The frequency sweep test also shows that shaving foam has a solid like behavior at $\gamma = 1e-3$, since the storage modulus, G', is always bigger than the loss modulus, G''. Furthermore, the solid-fluid transition with frequency sweep data cannot be seen on shaving foam at low strain amplitudes.

Relaxation (Strain-driven) Test

In the relaxation test, the sample is subjected to constant deformation (strain) and stress is measured as a function of time. The shear relaxation modulus, $\bar{G}(t)$, is calculated by

$$\bar{G}(t) = \frac{\tau(t)}{\gamma}, \tag{4.69}$$

where γ is the applied strain. The relaxation modulus can be transformed to a complex modulus (Eqn. 4.65). In this case, the Maxwell model, which is in a series connection of a Hookean spring ($\tau_s = G\gamma_s$, τ_s and γ_s are the spring stress and strain, and G $[N/m^2]$ is the spring constant (the shear modulus) and a Newtonian dashpot ($\tau_d = \eta\dot{\gamma}_d$, τ_d is the spring stress, η is the viscosity and $\dot{\gamma}_d$ is the shear rate), can be represented to drive the mathematical models for viscoelastic behavior.

In Figure 4.16, the ratio of the viscosity to the shear modulus is the stress relaxation time ($\lambda = \eta/G$). For the Maxwell model, the summation of the
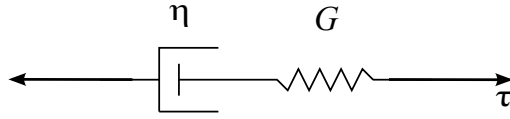
Figure 4.16: The Maxwell model

strain in the spring and the strain in the dashpot is the total strain, while the spring stress and the dashpot stress are equal to imposed stress

$$\gamma = \gamma_s + \gamma_d, \qquad\qquad \tau = \tau_s = \tau_d. \qquad (4.70)$$

Eqn. 4.70 can also be written in the form of shear rate

$$\dot{\gamma} = \dot{\gamma}_s + \dot{\gamma}_d = \frac{\dot{\tau}}{G} + \frac{\tau}{\eta}. \qquad (4.71)$$

Eqn. 4.71 can be multiplied by G and the equation $(\eta = G\lambda)$ can be used to derive Eqn. 4.72

$$G\dot{\gamma} = \dot{\tau} + \frac{\tau}{\lambda}. \qquad (4.72)$$

For the relaxation test, the shear rate must be zero $(\dot{\gamma} = 0)$, due to constant strain. Thus, Eqn. 4.72 is

$$\frac{\mathrm{d}\tau}{\mathrm{d}t} = -\frac{\tau}{\lambda}. \qquad (4.73)$$

When we integrate Eqn. 4.73, it can be written as

$$\int_{\tau_0}^{\tau} \frac{\mathrm{d}\tau}{\tau} = -\frac{1}{\lambda} \int_{0}^{t} \mathrm{d}t. \qquad (4.74)$$

Eqn. 4.74 becomes

$$\ln \tau - \ln \tau_0 = -\frac{t}{\lambda} \qquad \ln(\frac{\tau}{\tau_0}) = -\frac{t}{\lambda} \qquad \tau(t) = \tau_0 \exp(-t/\lambda). \qquad (4.75)$$

Eqn. 4.69 can be written by using Eqn. 4.75

$$\bar{G}(t) = \frac{\tau_0}{\gamma} \exp(-t/\lambda), \tag{4.76}$$

where $\bar{G}(t)$ was obtained directly. For the oscillation test, the stress and the strain, which are dependent on time, should be in the form of exponential expression ($\exp(i\omega t)$). Thus, the exponential expression can be written in Eqn. 4.72,

$$G\frac{\mathrm{d}\gamma(\exp(i\omega t))}{\mathrm{d}t} = \frac{\mathrm{d}\tau(\exp(i\omega t))}{\mathrm{d}t} + \frac{\tau \exp(i\omega t)}{\lambda}. \tag{4.77}$$

Eqn. 4.77 becomes

$$G(i\omega)\gamma^*(\exp(i\omega t)) = (i\omega)\tau^* \exp(i\omega t) + \frac{\tau^* \exp(i\omega t)}{\lambda}. \tag{4.78}$$

The complex modulus G^* can be also derived from Eqn. 4.78,

$$G^* = \frac{\tau^*}{\gamma^*} = G(i\omega)(\exp(i\omega t)) = ((i\omega) + \frac{1}{\lambda})\exp(i\omega t) = \frac{G(i\omega\lambda)}{1 + i\omega\lambda}. \tag{4.79}$$

The storage G' and loss modulus G'' can be expressed by multiplying Eqn. 4.79 with $(1 - i\omega\lambda)$

$$G^* = G' + iG'' = \frac{G\omega^2\lambda^2}{1 + \omega^2\lambda^2} + \frac{G\omega\lambda}{1 + \omega^2\lambda^2}i. \tag{4.80}$$

As explained above, the material behavior (viscoelastic fluid, viscoelastic solid and elastic solid) can be identified by using an oscillation test, but it is not the only way to obtain this rheological information. By performing the relaxation test, it is also possible to determine the material behavior and the differences of viscous liquids, viscoelastic materials, and elastic solid curves, as shown schematically in Figure 4.17. When deformation is applied on elastic materials, they are immediately deformed. However, viscous materials begin to relax with strain loading. Viscoelastic solids gradually relax and have an equilibrium stress which is not zero [34]. Viscoelastic fluids have a continuous deformation as long as the stress is maintained, while viscoelastic solids do not continue to deform, rather they have an equilibrium deformation. In order to understand the relaxation test, shaving foam was used to perform the relaxation test at 0.01 (Figure 4.18). The shear stress decreases with time at constant deformation and it approaches zero stress level. It shows that shaving foam behaves like viscoelastic fluid. The both amplitude sweep and relaxation experiments show viscoelastic behavior. On the other hand, the micro-structure of the shaving foam is fluidized in 10 min.
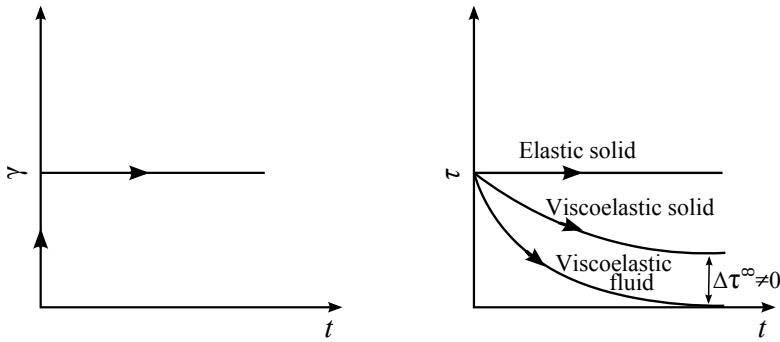
Figure 4.17: Schematic illustration of relaxation (strain-driven) test for different types of materials. Strain (left) and shear stress (right) as a function of time
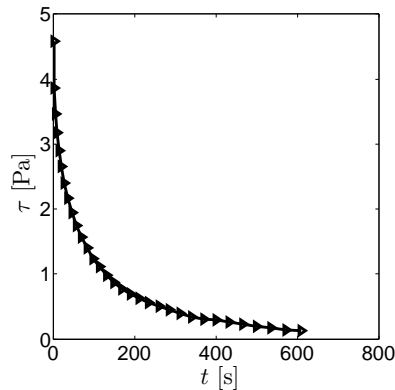
Figure 4.18: Shear stress as a function of time for shaving foam

Creep and Recovery (Stress-driven) Test

Another technique that is used for measuring the viscoelastic response of materials is the creep and recovery test. This test is the opposite of the relaxation test. It is performed by applying constant shear stress to the sample and unloading the stress so that the material starts to creep and recover (Figure 4.19). The viscoelastic properties of materials can be determined by using creep and recovery tests at very long loading times. This test distinguishes between the viscous and elastic portions of fluids and solids, respectively. When we compare the creep and recovery test with the harmonic test, the loading time of the creep and recovery test is longer than the harmonic test. For the creep test of the material, the stress-strain relations can be explained by simple models
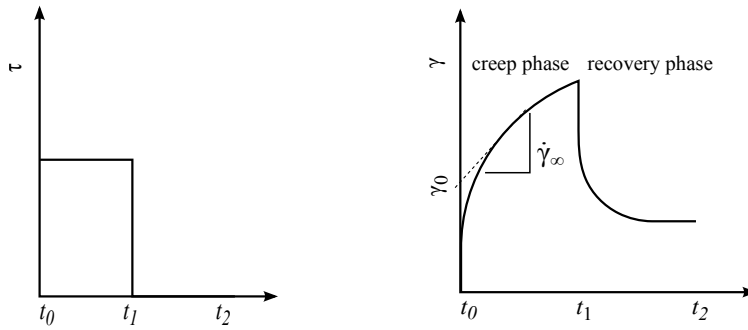
Figure 4.19: Creep and recovery test of a viscoelastic fluid

like Hooke, Newtonian and etc.. If we consider Hookes law (ideal solid), the elastic shear modulus G is calculated from

$$G(t) = \frac{\tau}{\gamma(t)}, \tag{4.81}$$

where $G(t)$ is inversly proportional to creep compliance $J(t)$. When the Maxwell model was used for creep test, Eqn. 4.72 becomes

$$G\dot{\gamma} = \frac{\tau}{\lambda}, \tag{4.82}$$

due to constant stress. Additionally, Eqn. 4.82 can be written as the shear viscosity

$$\eta = \frac{\tau}{\dot{\gamma}}, \tag{4.83}$$

which is the observation of a Newtonian fluid. Thus, the Maxwell model is not an appropriate mathematical model for the description of the creep test since it models strain as linear function of time [116].

The significance of creep test can be explained by the response of ideal elastic and viscous materials. In this case, the Kelvin-Voigt model, which is the combination of a spring and a dashpot in parallel, may be used as a mathematical model for creep test (Figure 4.20). For the Kelvin-Voigt model, the summation of the shear stress in the spring and the shear stress in the dashpot is the total shear stress, while the spring shear strain and the dashpot shear strain are identical

$$\tau = \tau_s + \tau_d, \qquad\qquad \gamma = \gamma_s = \gamma_d. \tag{4.84}$$
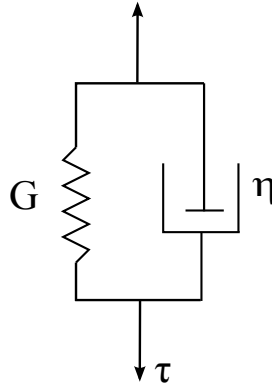
Figure 4.20: The Kelvin-Voigt model

Eqn. 4.84 can be written as

$$\tau = G\gamma + \eta\dot{\gamma}. \tag{4.85}$$

Eqn. 4.85 is divided through by η,

$$\frac{\tau}{\eta} = \frac{G}{\eta}\gamma + \frac{\mathrm{d}\gamma}{\mathrm{d}t}. \tag{4.86}$$

As it is explained in the part of relaxation test, $\frac{G}{\eta}$ is equal to $\frac{1}{\lambda}$. However, the constant λ is called retardation time in the creep test. In order to solve the differential equation (Eqn. 4.86), $(\exp\left(\int \frac{1}{\lambda}\mathrm{d}t\right) = \exp(t/\lambda))$ is multiplied by Eqn. 4.86,

$$\exp(t/\lambda)\frac{\tau}{\eta} = \exp(t/\lambda)\frac{1}{\lambda}\gamma + \exp(t/\lambda)\frac{\mathrm{d}\gamma}{\mathrm{d}t}. \tag{4.87}$$

Eqn. 4.87 is

$$\exp(t/\lambda)\frac{\tau}{\eta} = \frac{\mathrm{d}}{\mathrm{d}t}(\exp(t/\lambda)\gamma). \tag{4.88}$$

Integration form of Eqn. 4.88 is

$$\exp(t/\lambda)\frac{\tau}{\eta}\lambda + \mathrm{C} = \exp(t/\lambda)\gamma, \tag{4.89}$$

where C is a constant of integration. To determine C, the initial condition (the shear strain is zero at time t = 0) can be used for creep test. From Eqn. 4.89, C will be

$$\text{C} = -\frac{\tau}{\eta}\lambda = -\frac{\tau_0}{G}.$$
(4.90)

If the both sides of Eqn. 4.89 is divided to exponential term and Eqn. 4.90 is written into Eqn. 4.89, the shear strain will be

$$\gamma = \frac{\tau_0}{G} - \frac{\tau_0}{G}\exp(-t/\lambda).$$
(4.91)

4.3   Newtonian and non-Newtonian Fluids

As mentioned at the begining of the chapter, fluids can be classified into two groups: Newtonian and non-Newtonian fluids. The types of non-Newtonian fluids are: pseudoplastic (shear thinning), dilatant (shear thickening), rheopectic, and thixotropic.

Newtonian Fluids

Newtonian fluids, or linearly viscous fluids, have a constant viscosity (η), meaning that the slope of the shear stress (τ) versus shear rate ($\dot{\gamma}$) curves is constant.

$$\eta = \frac{\tau}{\dot{\gamma}} = \text{const.}$$
(4.92)

As it is explained before, a viscous fluid behavior is described by a dashpot (Figure 4.21) and a constant shear rate is produced by a constant applied stress.
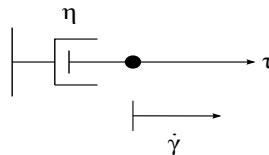
Figure 4.21: Rheological model of a Newtonian dashpot. The dashpot represents the viscous material behavior.

Another way to describe Newtonian fluids is that they flow without changing their viscosity when a great stress is applied. It means that viscosity is

Table 4.2: Measuring System: plate-plate, cone-plate, Couette cell

Type of geometry	unit	plate-plate	cone-plate	Couette cell
Diameter, D	[mm]	49.96	49.97	-
Bob diameter, D_i	[mm]	-	-	26.67
Cup diameter, D_o	[mm]	-	-	28.92
Measuring gap, h	[mm]	1	0.210	1.130
Cone angle, α	-	1.993°	120°	
Cone truncation, d	[μm]	-	210	-
Volume of material	[ml]	1.96	1.15	16

independent of the shear rate. Water, silicon oil, sugar solution, air, etc. are examples of Newtonian fluids. Additionally, a Newtonian fluid with known viscosity is measured to check the precision of a rheometer and this fluid is called as calibration or test fluid.
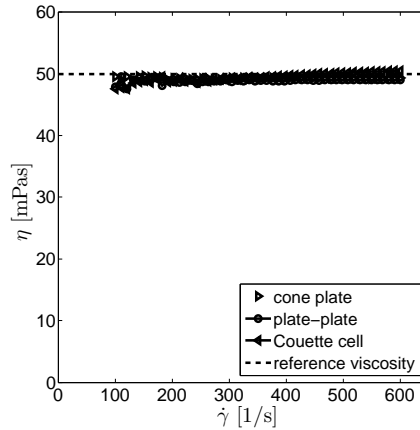
Figure 4.22: Viscosity curve of a Newtonian fluid (APN26 standard calibration sample, Anton Paar GmbH)

For this purpose, APN26 (Anton Paar GmbH) was used to calibrate cone-plate, plate-plate and Couette cell (Figure 4.22). The calibration test was performed three times to check the repeatability by using APN26, at 293 °K and atmospheric pressure. The viscosity of APN26 shown as a reference viscosity in Figure 4.22 is 50.30 [mPas]. The viscosity (η) vs. shear rate ($\dot{\gamma}$) curve was measured by three different types of geometry, such as cone-plate,

plate-plate and Couette cell. As it is seen in Figure 4.22, the type of geometry does not effect Newtonian fluids. The viscosity is constant for each type of geometry (Table 4.2). In addition, this type of flow is constant at a constant temperature and pressure.

Pseudoplastic (Shear-thinning)

Contrary to the Newtonian fluids, the apparent/effective viscosity of non-Newtonian fluids depends on the shear rate. If the viscosity decreases with increasing shear rate, the fluid is called pseudoplastic, or shear thinning. Some gels, pastes, liquid foam, whipped cream, and syrup are pseudoplastic fluids. They behave like a solids at rest,and when a critical shear stress is reached, they flow like a fluid. In order to understand the pseudoplastic materials, toothpaste is the best example. When we squeeze (apply shear stress) the tube of the toothpaste, it starts to flow like a fluid and its viscosity becomes lower than before. Otherwise, it cannot flow like a solid. In Figure 4.23, the shear stress and the viscosity versus shear rate curves of liquid foam (Gillette Classic Sensitive, Procter & Gamble UK) are given as an example to show pseudoplastic (shear thinning) behavior. The viscosity of liquid foam, which is not constant, decreases with increasing shear rate.
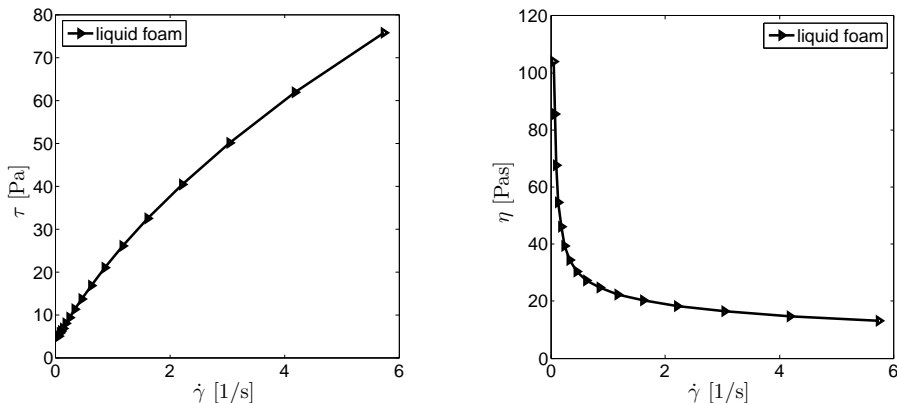
Figure 4.23: Shear stress (left) and Viscosity (right) curves of pseudoplastic fluid (liquid foam)

Many pseudoplastic fluids exhibit Newtonian behavior at extreme low and high shear rates, which cannot be observed for liquid foam. A typical pseudoplastic fluid having Newtonian region at low and high shear rates is shown in Figure 4.24, when η is plotted against $\dot{\gamma}$. The reason why liquid foam (Gillette Classic Sensitive, Procter & Gamble UK) does not exhibit Newtonian region

will be explained in Chapter 5. This Newtonian region has approximately constant viscosity while the viscosity decreases between the two Newtonian regions. The decreasing part is the power-law region and it is mathematically described by Ostwald De Waele [44]:

$$\eta = K\dot{\gamma}^{n-1}, \tag{4.93}$$

where $K[\text{Pas}^n]$ is the exponential constant parameter, and n is the power law index (which is smaller than "1" for pseudoplastic materials).
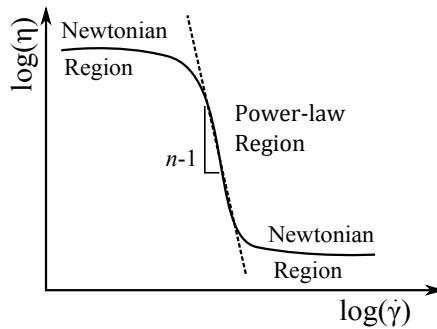
Figure 4.24: Viscosity-shear rate curve with Newtonian region for pseudoplastic fluids

In the power-law region, the behavior can be shown by

$$\log(\eta) = \log(K) + (n-1)\log(\dot{\gamma}), \tag{4.94}$$

where $(n-1)$ is the slope (Figure 4.24).

Dilatant (Shear-thickening)

If the viscosity of fluids increases with an increasing shear rate, the fluids are called dilatant or shear-thickening. Fluids with dilatant behavior are rather seldom. However, some examples, such as clay slurries, corn starch, solutions of certain surfactants, and several ceramic suspensions have dilatant behavior. Furthermore, the solid sand-water mixture is a good example to explain dilatant behavior. The peoples' feet will start to sink while they stand on wet sand. If they start to run, the water-sand mixture behaves as a solid (viscosity increases) due to greater shear stress. Thus, their feet do not sink in [117]. A typical shear stress vs. shear rate and viscosity vs. shear rate curve is shown in Figure 4.25.
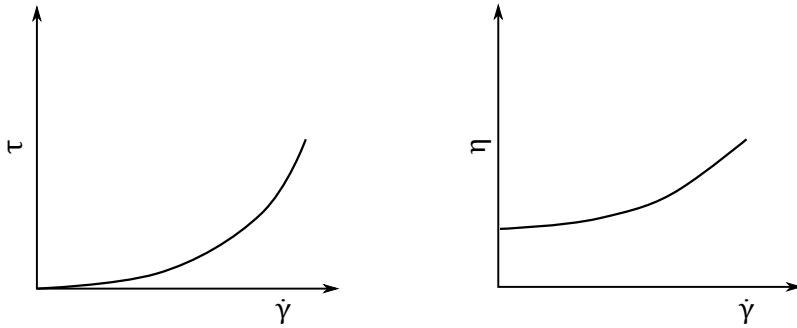
Figure 4.25: Shear stress-shear rate (left) and viscosity-shear rate (right) curves for dilatant fluids

Rheopectic and Thixotropic Fluids

The time dependent fluid behavior can be classified into two types, thixotropy and rheopexy. This fluid behavior is the dependency of viscosity on the micro-structure of the fluid. Thixotropic materials have a viscosity that decreases with constant shear rate, such as yoghurt, paints, tomato ketchup etc. When we shake ketchup, it becomes thinner and can flow more easily. The reason for this is that the viscosity of thixotropic materials decreases with an applied force. They can return to their original viscosity by unloading force. Thixotropic behavior is a very common property. However, rheopectic materials are very rare. For rheopectic materials, the viscosity increases with constant shear rate. The time dependent effects are caused by the breakdown or buildup of ordered structure within the flowing matter.

Deborah Number

Deborah number, which is dimensionless number, is used to characterize the fluidity of a material. The number is symbolized by De and is defined as

$$De = \frac{\lambda}{t_p}, \tag{4.95}$$

where λ is the stress relaxation time of the material and t_p is the characteristic flow time which is investigated. Deborah number defines the difference between solids and fluids. If the relaxation time is smaller than the characteristic flow time, material flows like a fluid. However, if the relaxation time is larger than the characteristic flow time, material is a solid [96].

4.3.1 Generalized Newtonian Fluid in Simple Shear

The Generalized Newtonian Fluid can be explained by modifying Newton's law of viscosity. In order to generalize the Newtonian fluid, one replaces the constant viscosity by a viscosity function which depends on the magnitude of the deformation rate tensor ($\mathbf{D}$) or, in general, depends on the scalar invariants of the deformation rate tensor ($\mathrm{I} = \mathrm{tr}\mathbf{D}; \mathrm{II} = \mathrm{tr}\mathbf{D}^2; \mathrm{III} = \mathrm{tr}\mathbf{D}^3$)[100]. However, the first invariant (I) is zero for incompressible fluid and the third invariant (III) vanishes for shear flows. Therefore, the viscosity depends on the second invariant (II) and the generalized Newtonian fluid follows a constitutive equation

$$\mathbf{T} = -p\,\mathbf{I} + \eta_g(\mathrm{II})\mathbf{D}, \qquad (4.96)$$

where p represents the pressure and $\mathbf{I}$ is the second order unit tensor. However, considering incompressible fluid, the pressure term does not reflect any rheological property.

As it is discussed before, for simple shear flow (Figure 4.4), $u = u_x$ depends on the coordinate in the $\mathbf{e}_x$ direction, $u_x = \dot{\gamma}x$ and u_y, u_z are equal to zero, $u_y = u_z = 0$. In this problem, the velocity gradient is determined as

$$\mathrm{grad}\mathbf{u} = \begin{bmatrix} 0 & \dot{\gamma} & 0 \\ 0 & 0 & 0 \\ 0 & 0 & 0 \end{bmatrix} \mathbf{e}_i \otimes \mathbf{e}_j. \qquad (4.97)$$

By using the velocity gradient, the rate of deformation tensor is calculated

$$\mathbf{D} = \frac{1}{2} \begin{bmatrix} 0 & \dot{\gamma} & 0 \\ \dot{\gamma} & 0 & 0 \\ 0 & 0 & 0 \end{bmatrix} \mathbf{e}_i \otimes \mathbf{e}_j. \qquad (4.98)$$

The second invariant of deformation rate tensor is

$$\mathrm{II} = \frac{1}{2}((\mathrm{tr}\mathbf{D})^2 - (\mathrm{tr}(\mathbf{D}^2)) = -\frac{\dot{\gamma}^2}{4}. \qquad (4.99)$$

A non-negative quantity, such as S, is used instead of the second invariant, $S = -4\mathrm{II}$. In other words, S is equal to $\dot{\gamma}^2$ ($S := \dot{\gamma}^2$) in simple shear flow.

Thus, the constitutive equation (Eqn. 4.96) without pressure term can be written as

$$\mathbf{T} = \begin{bmatrix} T_{xx} & T_{xy} & T_{xz} \\ T_{yx} & T_{yy} & T_{yz} \\ T_{zx} & T_{zy} & T_{zz} \end{bmatrix} \mathbf{e}_i \otimes \mathbf{e}_j = \eta_g \frac{\dot{\gamma}}{2} \begin{bmatrix} 0 & 1 & 0 \\ 1 & 0 & 0 \\ 0 & 0 & 0 \end{bmatrix} \mathbf{e}_i \otimes \mathbf{e}_j. \tag{4.100}$$

From Eqn. 4.100, the only non-zero components of $\mathbf{T}$ are

$$T_{xy} = T_{yx} = \eta_g \frac{\dot{\gamma}}{2}, \tag{4.101}$$

where T_{xy} is the shear stress. The normal stresses of $\mathbf{T}$ are

$$T_{xx} = T_{yy} = T_{zz} = 0. \tag{4.102}$$

For describing the rheological behavior of a fluid, three viscometric functions (the shear stress function, the first normal stress difference and the second normal stress difference) are needed

$$\tau(\dot{\gamma}) = T_{xy} = \eta_g \frac{\dot{\gamma}}{2}, \quad N_1 = T_{xx} - T_{yy} = 0, \quad N_2 = T_{yy} - T_{zz} = 0. \tag{4.103}$$

From Eqn. 4.103, the shear stress can be written as,

$$\eta \dot{\gamma} = \eta_g \frac{\dot{\gamma}}{2}. \tag{4.104}$$

Thus, $\eta_g = 2\eta$ and the Cauchy stress tensor $\mathbf{T}$ is

$$\mathbf{T} = -p\,\mathbf{I} + 2\eta(\mathrm{II})\mathbf{D}. \tag{4.105}$$

4.3.2　Non-Newtonian Constitutive Models

Power-Law Model

As it is explained before, power-law model or Ostwald-de Waele relationship [44] (Eqn. 4.93) describes the data of shear-thinning and shear-thickening fluids. The shear stress of the power-law model can be written as:

$$\tau = K_p\,\dot{\gamma}^n, \tag{4.106}$$

where n is the power law index and K_p is called the consistency. The viscosity of the power-law model is determined by the derivative $\left(\frac{\mathrm{d}\tau}{\mathrm{d}\dot{\gamma}}\right)$ of Eqn. 4.106

$$\eta(\dot{\gamma}) = \frac{\mathrm{d}\tau}{\mathrm{d}\dot{\gamma}} = K_p \, n \, \dot{\gamma}^{n-1}. \tag{4.107}$$

In order to express fluid models, simple shear flow, which is mentioned above, is used. For the three dimensional representation, S is written instead of $\dot{\gamma}$ and the viscosity is

$$\eta(S) = K_p \, n \, S^{\frac{n-1}{2}}, \tag{4.108}$$

where $S := \dot{\gamma}^2$. For shear-thinning fluid, the viscosity is infinite at zero shear rate and is zero at infinite shear rate,

$$n < 1, \qquad \lim_{S \to 0} \eta(S) = \infty, \qquad \lim_{S \to \infty} \eta(S) = 0, \tag{4.109}$$

$$n > 1, \qquad \lim_{S \to 0} \eta(S) = 0, \qquad \lim_{S \to \infty} \eta(S) = \infty. \tag{4.110}$$
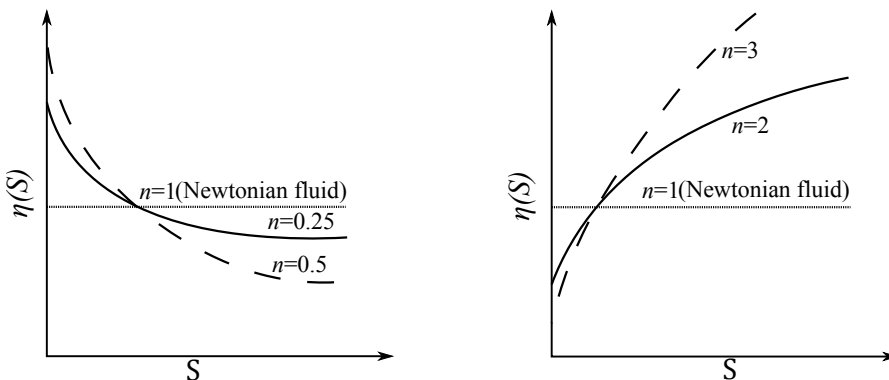
Figure 4.26: Power-law fluids for n less than 1 or equal to 1 (shear-thinning or Newtonian) (left) and Power-law fluids for n greater than 1 or equal to 1 (shear-thickening or Newtonian) (right)

Bingham Fluid Model

The Bingham fluid is a viscoplastic fluid and the proportionality between the shear stress and the shear rate is linear. The Bingham fluid can be treated as Newtonian fluid for zero yield stress (Figure 4.27).
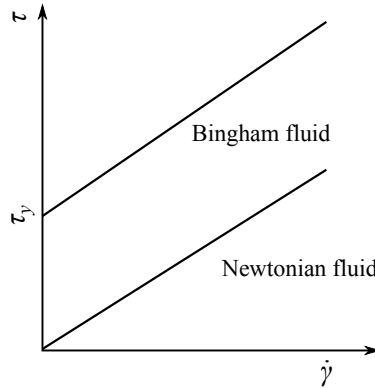
Figure 4.27: Bingham fluid model

The Bingham model can be represented as

$$\tau = \tau_y + \dot{\gamma} \ K_B, \tag{4.111}$$

where τ_y is a constant material parameter and called the yield stress. From Eqn. 4.111, the effective viscosity can be obtained as

$$\eta(\dot{\gamma}) = \frac{d\tau}{d\dot{\gamma}} = K_B. \tag{4.112}$$

If the shear stress is greater than the yield stress, the shear rate is

$$\tau > \tau_y, \qquad \dot{\gamma} = \frac{\tau - \tau_y}{K_B}. \tag{4.113}$$

On the other hand, the fluid does not flow ($\dot{\gamma}$ is zero), when the shear stress is equal to or smaller than the yield stress

$$\tau \le \tau_y, \qquad \dot{\gamma} = 0. \tag{4.114}$$

The Modified Bingham-Papanastasiou Model

The modified Bingham model was proposed by Papanastasiou [90] and Papanastasiou's modification is given by

$$\tau = \dot{\gamma} \, K_{BP} + \tau_y \, (1 - \exp(-m\dot{\gamma})), \qquad (4.115)$$

where m and K_{BP} are constant material properties. This model was used for the behavior of visco-plastic materials [55]. The visco-plastic behavior is possible for all cases that may occur in debris flow modelling [102]. In Schneider et al. [102], viscosity function, which is independent on the third invariant (III) in simple shear flow, was restricted with yield stress. For the incorporation of the yield stress, the modification of the Bingham model is used to avoid the discontinuity in the flow curve (Figure 4.28). The model includes an exponential term to permit the use of one equation for the flow curve upper and below the yield stress τ_y [71].
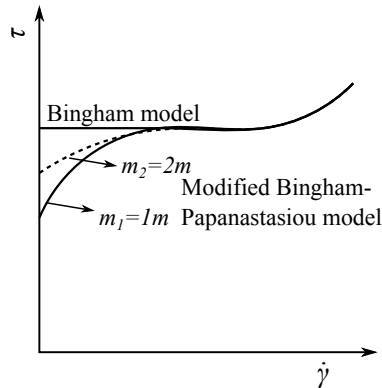
Figure 4.28: Papanastasiou's modification for a Bingham model according to the exponential part for different values of the regularization parameter m (log-log plot)

The effective viscosity function, which is a function of shear rate $\dot{\gamma}$, is defined as

$$\eta(\dot{\gamma}) = \frac{d\tau}{d\dot{\gamma}} = K_{BP} + m \, \tau_y(\exp(-m\dot{\gamma})). \qquad (4.116)$$

In simple shear flow, S is written instead of $\dot{\gamma}$ and the viscosity is

$$\eta(S) = K_{BP} + m \, \tau_y(\exp(-m \, S^{\frac{1}{2}})). \qquad (4.117)$$

From Eqn 4.118, the viscosity function has a constant viscosity at zero and an infinite shear rate

$$\lim_{S \to 0} \eta(S) = K_{BP} + m \ \tau_y, \qquad \lim_{S \to \infty} \eta(S) = K_{BP}. \qquad (4.118)$$

Herschel-Bulkley Model

The Herschel-Bulkley model is mostly applied to non-Newtonian fluids. When the yield stress is added in the power law model ($\dot{\gamma}^n \ K_{HB}$), the model is known as the Herschel-Bulkley model

$$\tau = \tau_y + \dot{\gamma}^n \ K_{HB}. \qquad (4.119)$$

The viscosity of the model can be expressed as

$$\eta(\dot{\gamma}) = \frac{d\tau}{d\dot{\gamma}} = n \ K_{HB} \ \dot{\gamma}^{(n-1)}. \qquad (4.120)$$

In the simple shear flow, the viscosity can be derived by

$$\eta(S) = n \ K_{HB} \ S^{(n-1)/2}. \qquad (4.121)$$

A fluid defined by the Herschel-Bulkley model can be either shear thickening or shear thinning. The distinction between these two terms lies in the value of the flow behavior parameter n. Values of n that are less than 1 implies shear thinning, whereas the reciprocal indicates shear thickening. The viscosity in the limit of vanishing S and in the limit of S tending to infinity can be written as

$$n < 1, \qquad \lim_{S \to 0} \eta(S) = \infty, \qquad \lim_{S \to \infty} \eta(S) = 0, \qquad (4.122)$$

$$n > 1, \qquad \lim_{S \to 0} \eta(S) = 0, \qquad \lim_{S \to \infty} \eta(S) = \infty. \qquad (4.123)$$

When n is 1, the viscosity is constant and fluid behaves as a Newtonian fluid.

$$n = 1, \qquad \eta(S) = n \ K_{HB} \quad \text{(Newtonian)}. \qquad (4.124)$$

The Modified Herschel-Bulkley-Papanastasiou Model

In the current study, the modified Herschel-Bulkley-Papanastasiou model was used for rheological experiments (flow curve tests) of particle foam mixtures in order to match with experimental results (see Chapter 5). As it is mentioned in [102], some models (Herschel-Bulkley-Papanastasiou, Hesrchel-Bulkley, Bingham etc.) are appropriate for particle laden flows with low solids concentration. However, they are not useful for high solids concentration due to frequent frictional contact between the particles. The Herschel-Bulkley model has an infinite viscosity at zero shear rate (Eqn. 4.122), which is physically unrealistic [102]. Therefore, a regularized Herschel-Bulkley model was proposed by Papanastasiou [90]. The modified Herschel-Bulkley-Papanastasiou model is

$$\tau = K \ \sqrt{\dot{\gamma}} + \tau^* \ (1 - \exp(-a \ \dot{\gamma})), \tag{4.125}$$

where a, K and τ^* are constant material parameters. The effective viscosity can be derived from the shear stress τ and is written as

$$\eta(\dot{\gamma}) = \frac{d\tau}{d\dot{\gamma}} = \frac{1}{2} \ K \ \dot{\gamma}^{-\frac{1}{2}} + \tau^* \ a \ (\exp(-a \ \dot{\gamma})). \tag{4.126}$$

In addition, the viscosity can be also written in simple shear form. A mathematical equation of the modified Herschel-Bulkley-Papanastasiou model is

$$\eta(S) = \frac{1}{2} \ K \ S^{-\frac{1}{4}} + \tau^* \ a \ (exp(-a \ S^{\frac{1}{2}})). \tag{4.127}$$

For the modified Herschel-Bulkley-Papanastasiou model, the shear rate ($\dot{\gamma}$) was calculated with the constant power law index $n = \frac{1}{2}$, meaning that n is less than 1 and the constitutive equation is shear thinning. The viscosity of the modified Herschel-Bulkley-Papanastasiou model in the limit of vanishing S and in the limit of S tending to infinity are:

$$\lim_{S \to 0} \eta(S) = \infty, \qquad \lim_{S \to \infty} \eta(S) = 0. \tag{4.128}$$

The model has also a disadvantage, like the Herschel-Bulkley model. For low shear rate regions, the model does not describe viscosity of a material. At low shear rates, viscosity goes to infinity rather than to a constant viscosity [71]. However, when the modified Herschel-Bulkley-Papanastasiou model is applied on the liquid foam or particle-foam mixture, the transient viscosity effect (see Chapter 5) is considered to neglect constant viscosity (Newtonian plateau) at low shear rate. Thus, the disadvantage of this model can be neglected for the rheological experiments of the liquid foam and particle-foam mixture.

The Modified Herschel-Bulkley-Papanastasiou Model for Cone-Plate Geometry

In cone-plate geometries, the shear flow for the modified Herschel-Bulkley-Papanastasiou model at small angle can be obtained by Eqn. 4.115. The only non-zero component of the stress tensor is

$$\ln \tau_{\theta\varphi} = \ln\left(K\sqrt{\dot{\gamma}}\right) + \ln\left(\tau^*(1 - \exp(-a\,\dot{\gamma}))\right). \tag{4.129}$$

Eqn. 4.129 (Derivation of Eqn. 4.130 was schown in Appendix B) can be expressed by

$$\tau_{\theta\varphi} = K\,\dot{\gamma}^{\frac{1}{2}}\,\exp(a\dot{\gamma}). \tag{4.130}$$

The partial derivative can be used to determine the viscosity

$$\eta = \frac{\partial \tau}{\partial \dot{\gamma}} = n\frac{\partial m}{\partial \dot{\gamma}} + m\frac{\partial n}{\partial \dot{\gamma}}, \tag{4.131}$$

where $m = K\,\dot{\gamma}^{\frac{1}{2}}$, $\frac{\partial m}{\partial \dot{\gamma}} = \frac{1}{2}\,K\dot{\gamma}^{-\frac{1}{2}}$ and $n = \exp(a\dot{\gamma})$, $\frac{\partial n}{\partial \dot{\gamma}} = a\exp(a\dot{\gamma})$. From Eqn. 4.131, the viscosity is

$$\eta = \exp(a\dot{\gamma})\,\frac{1}{2}K\,\dot{\gamma}^{-\frac{1}{2}} + K\,\dot{\gamma}^{\frac{1}{2}}\,a\,\exp(a\dot{\gamma}). \tag{4.132}$$

When $\dot{\gamma} = \frac{\beta}{\omega}$ (Eqn. 4.22) and $\exp(a\dot{\gamma}) = \frac{\tau_{\theta\varphi}}{K\,\dot{\gamma}^{\frac{1}{2}}}$ were inserted in Eqn. 4.132, the viscosity of the modified Herschel-Bulkley-Papanastasiou model for cone-plate flow is

$$\eta = \exp(a\dot{\gamma})K(\frac{1}{2}\dot{\gamma}^{-\frac{1}{2}} + a\dot{\gamma}^{\frac{1}{2}}) = \tau_{\theta\varphi}\left(\frac{1}{2}(\frac{\beta}{\omega})^{-\frac{1}{4}} + a\right). \tag{4.133}$$

On the other hand, from Eqn. 4.16, the viscosity can be also described by

$$\eta = \frac{C_1}{K\sin^2\theta}\left(\frac{1}{2}(\frac{\beta}{\omega})^{-\frac{1}{4}} + a\right). \tag{4.134}$$

The Modified Herschel-Bulkley-Papanastasiou Model for Plate-Plate Geometry

If the modified Herschel-Bulkley-Papanastasiou model is derived for shear flow in plate-plate geometries, Eqn. 4.130, which is the non-zero component of the stress tensor, was used

$$\tau_{\Phi z} = K \ \dot{\gamma}^{\frac{1}{2}} \ \exp^{a\dot{\gamma}}. \tag{4.135}$$

At "no slip" boundary condition ($\dot{\gamma} = \frac{\omega r}{h}$), the viscosity with $\exp^{a\dot{\gamma}} = \frac{\tau_{\phi z}}{K \ (\dot{\gamma})^{\frac{1}{2}}}$ is

$$\eta = \exp(a\dot{\gamma})K(\frac{1}{2}\dot{\gamma}^{-\frac{1}{2}} + a\dot{\gamma}^{\frac{1}{2}}) = \tau_{\Phi z}\left(\frac{1}{2}(\frac{\omega r}{h})^{-\frac{1}{4}} + a\right). \tag{4.136}$$

At "slip" boundary condition ($\dot{\gamma} = \dot{\gamma} + \frac{2u_s}{h}$), the viscosity is

$$\eta = \tau_{\Phi z}\left(\frac{1}{2}(\dot{\gamma} + \frac{2u_s}{h})^{-\frac{1}{4}} + a\right). \tag{4.137}$$

Chapter 5

Rheology of Particle-Foam Mixtures

5.1 Introduction

Liquid foam consists of gas bubbles surrounded by a liquid cell wall or thin film [76]. It has a linear viscoelastic behavior under small shear stresses and shows viscous liquid behavior under large stresses [59]. Another phenomenon is the jamming of foam suspensions, which is the transition from freely flowing to rigid phase [66]. In this study, we investigate the jamming point of foam suspensions (particle-foam mixture) with volume fraction of particles through the rheological experiments. Haffner et al. [49] determined the drainage velocity, in which the drainage stops due to a suspensions jam. The jamming of the suspension within the interstitial foam was explained by high volume fraction of particles. The phenomena are not easy to understand, though foam and its properties have been researched in different areas. Many authors investigated liquid foam with respect to its rheological and mechanical behavior, such as body care, oil well drilling, food and tunneling etc. Durian [26] focused on the mechanics of foam, which explains the linear elastic properties as a function of bubble volume fraction. Besides, Durian et al. [27] considered suspensions of hard spheres (emulsions and foam). In [27], the jamming behavior, which is the function of particle concentration and shear stresses, was studied. In addition, Katgert et al. [56] dealt with the jamming scenario for foams, including the differences between the mechanics of disordered foams and ordered models. In Rio et al. [97], liquid foam was mentioned that is thermodynamically unstable. The instability of liquid foam may occur due to temperature. The temperature causes the rupture of thin films in the liquid foam [109]. Another mechanism of liquid foam instability may be explained by the aging of foam (coarsening) because of Ostwald ripening (disproportionation) [101]. Large bubbles grow in size at the expense of smaller ones in course of time. This phenomenon was

first described by Wilhelm Ostwald in 1896. Several chemists reported that foams can be stabilized by particles [25, 38, 106]. The stability of liquid foam was taken into account in [106], which explains the increase in the stability of the liquid foam by adding fumed silica nanoparticles. On the other hand, few papers are about the rheological behavior of particle stabilised liquid foam mixtures. The viscoelastic properties of particle laden foam are investigated by Cohen-Addad et al. [21]. The experiments were performed using shaving foam (Gillette Classic Sensitive, Procter & Gamble UK) and solid particles (glass beads, carbon beads and talc platelets) of different average diameters. Hereby, the volume fraction of glass beads ($n_0^s = dv_0^s/dv$) were increased up to only 0.39 in the same study.

The rheological behavior of particle-liquid foam mixture has not been completely uncovered because of its high complexity. Therefore, many experiments, such as flow curve tests and oscillation tests (amplitude sweep), have been performed for particle stabilised liquid foam. Nevertheless, the volume fraction of particles n_0^s can be taken up to 0.30 due to noisy data occuring for higher values. The noisy data is unpredictable and meaningless data when a measurement is repeated and none of the results can be preferred over the others. The challenge was explained by the jamming point and the influence of particles that cause jamming transition, was proven with the capillary rise method. The method is the measurement process of contact angle between small particles and liquid interface. As it was mentioned in [87], the method depends on direct measurements of interfacial energies.

To solve this challenge, particles were mixed with distilled water before mixing with foam. The volume fraction of wetted particles n_0^{w+s} (up to 0.64) are mixed with liquid foam. Consequently, the purpose of this experimental study was to show the stability effect of particles in liquid foam and to develop a better understanding of the rheological behavior of particle-liquid foam mixtures with high volume fraction of particles n_0^s by rheological flow curve and amplitude sweep tests (plate-plate conditions).

5.2   Preparation and Characterization

5.2.1   Preparation of Particle-Foam Mixtures

In order to study the effect of particles in liquid foam and capture their rheological behavior, the strategy shown in Chapter 2, Figure 2.3 has been applied during experimental work. The effective rheology of particle-foam mixtures depends on the volume fractions of the constituents.

Firstly, the particle-liquid foam mixtures have been used by increasing the volume fraction of dry solid particles ($n_0^s = dv_0^s/dv_0$), where dv_0^s is the volume of the biphasic mixture. $\rho^\alpha = dm^\alpha/dv^\alpha$ represents the partial density with $\alpha \, \epsilon$ $\{s, f\}$ in the unit cell with total volume dv_0. In addition, the volume fraction

of the liquid foam is symbolised by n_0^f and is determined by $\mathrm{d}v_0^f/\mathrm{d}v_0$. The total volume $\mathrm{d}v_0 = \sum_\alpha \mathrm{d}v_0^\alpha$ has been kept constant at 40 cm^3 before mixing the components. After the mixing process, the total volume, $\mathrm{d}v$, does not remain constant ($\mathrm{d}v \neq \mathrm{d}v_0$). This case, which has a high volume of foam and low volume of glass particles, can be seen in Table 5.1. The values of $\mathrm{d}v$ are given in Table 5.1 for different volume fractions of solid particles. In addition, FIR discussed in Chapter 2 can also be seen in Table 5.1.

Table 5.1: The volume fraction of dry particle-foam mixtures ($t_1 > t_0$), $\mathrm{d}v_0 = 40$ cm^3

Case	1	2	3	4	5	6	7	8
$\mathrm{d}v_0^s$[cm^3]	0	2	4	6	8	10	12	14
$\mathrm{d}v_0^f$[cm^3]	40	38	36	34	32	30	28	26
n_0^s	0	0.05	0.10	0.15	0.20	0.25	0.30	0.35
n_0^f	1	0.95	0.90	0.85	0.80	0.75	0.70	0.65
$\mathrm{d}v$[cm^3]	46.3	48.6	48.6	48	41.3	39.6	39.3	38
FIR[vol%]	-	1900	900	566	400	300	233	186

In order to modify the contact angle between particles, they should be wet by means of distilled water. It moves through the solid particles due to gravity, separating them from each other. The volume fraction of the distilled water $n_0^w = \mathrm{d}v_0^w/\mathrm{d}v_0$ and solid particles $n_0^s = \mathrm{d}v_0^s/\mathrm{d}v_0$ have been kept constant at 0.30 and 0.70, respectively. The total mass of solid particles $\mathrm{d}m^s$ is equal to 49.8 g and the density of solid particles ρ^{sR} is 2.5 g/cm^3. The volume of solid particles without air can be calculated as the ratio of the total mass of solid particles to the density of solid particles ($\mathrm{d}v_0^{s-a} = \frac{\mathrm{d}m^s}{\rho^{sR}} = \frac{49.8}{2.5} = 20$ cm^3), so subtracting it from the volume of solid particles with air $\mathrm{d}v_0^s = 37$ cm^3 gives the volume of air $\mathrm{d}v_0^a = 17$ cm^3. The porosity ϕ is the ratio of the volume of air to the volume of solid particles with air ($\phi = \frac{\mathrm{d}v_0^a}{\mathrm{d}v_0^s} = \frac{17}{37} = 0.46$) and the water saturation S_w is defined as the ratio of the volume fraction of water to the porosity ($S_w = \frac{n_0^w}{\phi} = \frac{0.30}{0.46} = 0.65$). For volume of the wetted solid particles-liquid foam mixtures $\mathrm{d}v_0^{w+s+f}$, volume of the wetted particles $\mathrm{d}v_0^{w+s}$ was increased, whereas the volume of the foam $\mathrm{d}v_0^f$ was kept at 20 cm^3. The volume fraction of the wetted solid particles can be determined by $n_0^{w+s} = \mathrm{d}v_0^{w+s}/\mathrm{d}v_0^{w+s+f}$, where $\mathrm{d}v_0^{w+s}$ is the volume of triphasic mixture ρ^β with $\beta \, \epsilon \, \{w, s, f\}$. The total volume $\mathrm{d}v^{w+s+f}$, which is the volume after mixing the components, is higher than $\mathrm{d}v_0^{w+s+f}$ because of wet particles (Table 5.2). In order to obtain reliable results and to reduce the deviation of them, all cases shown in Table 5.1 and Table 5.2 were carried out three times.

Table 5.2:   The volume fraction of surface wetted particle-foam mixtures $(t_2 > t_1)$

Case	1	2	3	4
$dv_0^s[\text{cm}^3]$	37	37	37	37
$dv_0^{s-a}[\text{cm}^3]$	20	20	20	20
ϕ	0.46	0.46	0.46	0.46
$dv_0^w[\text{cm}^3]$	16	16	16	16
$dv_0^{w+s}[\text{cm}^3]$	6	10	20	36
$dv_0^f[\text{cm}^3]$	20	20	20	20
n_0^{w+s}	0.23	0.33	0.50	0.64
n_0^f	0.77	0.67	0.50	0.26
$dv_0^{w+s+f}[\text{cm}^3]$	28	34	46	56.6
$FIR[\text{vol}\%]$	333	200	100	67

5.2.2   Surface Properties of Glass Beads

As mentioned above, the total volume of the mixture decreases with an increase in volume fractions of dry solid particles. The increase in contact among the particles causes the particle-liquid foam mixture to behave more like a solid. To understand interaction between particle and liquid foam, contact angles are measured. This phenomenon may be explained by the wettability of a material (hydrophobic and hydrophilic surfaces). Hydrophobic surface: the contact angle ($\theta > 90°$) is greater than 90° which has high wettability. Hydrophilic surface: liquids are attracted to solid surfaces (adhesion) more strongly than to other liquid molecules (cohesion), exhibit a small contact angle, and correspond to low wettability [122]. Accordingly, the contact angle of the glass particles should be known and it is possible with the capillary rise method (Figure 5.1).
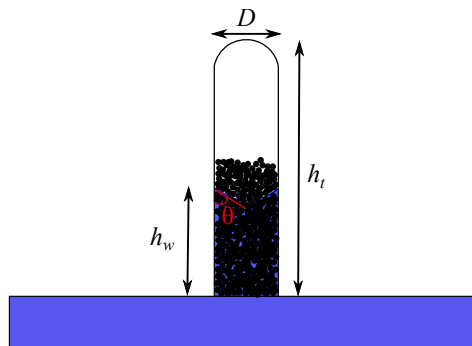
Figure 5.1: Capillary rise method

This is a useful method to determine the contact angle of the powders. The method is expressed by the Washburn theory [119]

$$h_w^2 = \bar{r}\frac{\overline{\gamma}\cos\theta}{2\eta}t,$$ (5.1)

where $\bar{r}$ is constant and called radius of the capillary. $\overline{\gamma}$, t, θ and η are surface tension, time, contact angle and viscosity, respectively. For the capillary rise method, a capillary tube with 15 mm height h_t and 3 mm diameter D, distilled water and hexane ($CH_3(CH_2)_4CH_3$) were used. Especially, hexane was used due to its very low surface energy which assumed completely wet ($\theta = 0°$, $\cos\theta = 1$)[23]. The constant parameter, $\bar{r}$, can be determined and used to find the yet unknown contact angle for the investigated glass particles. To determine $\bar{r}$, particles were filled in the capillary tube and then filter paper was put at the outlet of the capillary tube to prevent particles falling from the tube. The capillary tube filled with particles was put into cup filled with hexane. It was observed that the hexane rised into the capillary tube and the height of the wet part ($h_w = 4.75$ mm) was measured in 1 min. The viscosity and the surface tension of hexane are $\eta_H = 3 \ 10^{-4}$ Pas and $\overline{\gamma}_H = 18 \ 10^{-3}$ Nm^{-1}, respectively [87]. The constant $\bar{r} = 263.9 \ 10^{-8}$ m was determined, which will be used for determination of contact angle. The same procedure was done for distilled water and the height of the part is equal to 5.5 mm in 1.19 min. The value of contact angle was calculated and is equal to 36.87°. It shows that the contact angle smaller than 90° which means the glass particles are hydrophilic.

5.2.3 Morphological Characterization of Foam, Particle and Particle-Foam Mixtures

The microstructure of liquid foam has been analysed by many researchers [64, 86, 120]. A liquid foam consists of bubbles, films, and plateau borders, which effect the physical properties, like temporal stability. The stability of foam, which was handled in [60], depends on the bubble size distribution. In addition, Chu [20] showed that the stability of liquid foams increased with increasing the amount of hydrophilic solid particles. In our experiment, solid glass beads (Silibeads® Glass Beads Type S) were mixed with liquid foam. Due to its polymer stability and easy accesibility, shaving foam (Gillette Classic Sensitive, Procter & Gamble UK) was used as liquid foam. As it has been revealed in the literature, that the microstructure of foam determines the effective rheological properties [61]. The size, shape, and distribution of foam bubbles/cells and particles were characterized by lasergranulometer (CILAS 1090 L, Fa. Quantachrome GmbH) and light microscope (Carl Zeiss Microscopy GmbH) with camera (AxioCam MRc Rev.3 FireWire (D)) and the modular

a)   b)
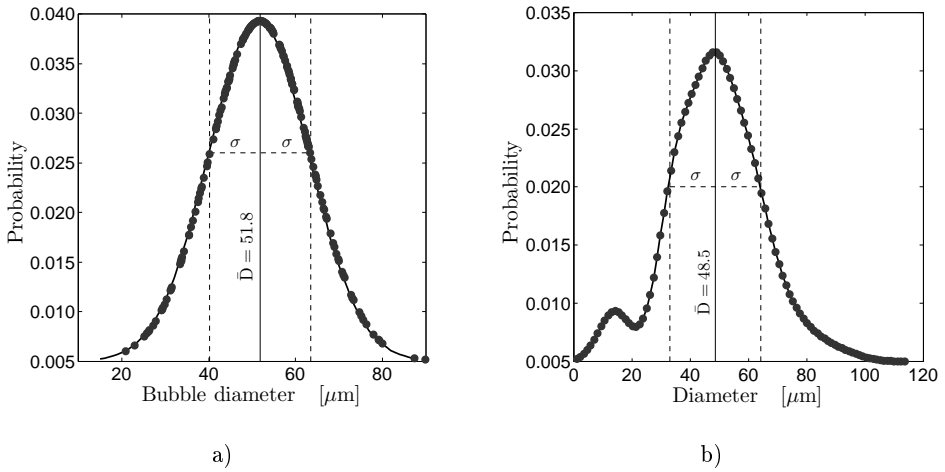
Figure 5.2: (a) Probability density function of foam bubble size (left) [89] and glass beads diameter. (b) Mean value of particle diameter ($\bar{D} = 48.5$ μm) and bubble size ($\bar{D} = 51.8$ μm). Standard deviation of the bubble size ($\sigma = 11.6$ μm) and the diameter of particles ($\sigma = 15.58$ μm)

design of SteREO Discovery.V12 (motorized 12x zoom)[89], Figure 5.2. The mean diameter of the glass beads ($\bar{D} = 48.5$ μm) is close to that of the mean bubble diameter $\bar{D}$, which is equal to 51.8 μm. The distributions of both solid particle diameters and bubble sizes are Gaussian-like.

a)   b)
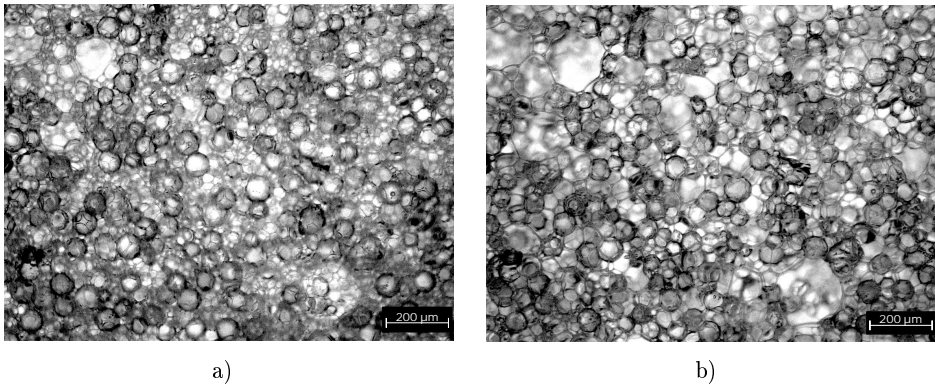
Figure 5.3: (a) Microstructure of dry particle-liquid foam mixture with volume fraction of dry particles ($n_0^{s7} = 0.30$) after 2 min. and (b) after 57 min.

To analyse the microstructure of dry glassbeads-liquid foam and surface wetted glass beads-liquid foam mixtures, light microscope images were captured, (see Figure 5.3 and 5.4). The microstructures are shown in Figure 5.3

for dry solid glass beads-liquid foam mixtures with $n_0^{s7} = 0.30$ after 2 min. (a) and 57 min. (b).

a)

b)

c)
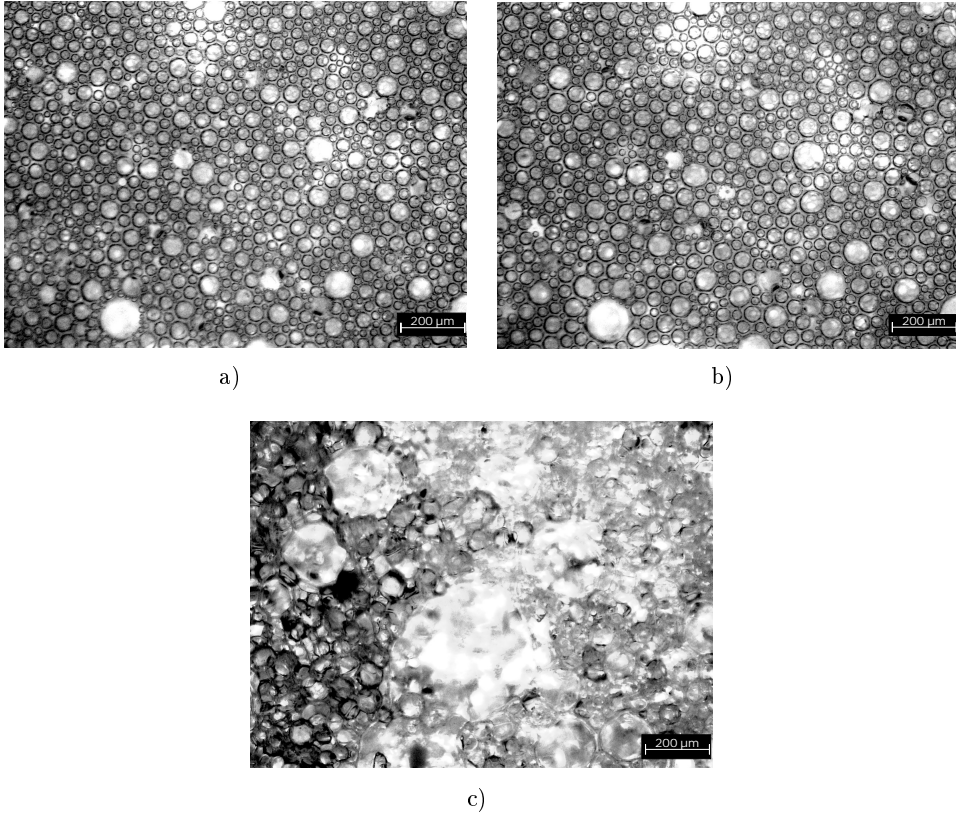
Figure 5.4: Microstructure of surface wetted particle-liquid foam mixture with surface wetted particles ($n_0^{(s+w)4} = 0.64$) (a) after 1 min., (b) after 10 min. and (c) after 1 hour.

The glass beads surrounded by bubbles, prevent the coalescence of the liquid foam. They also restrain coarsening of foam bubbles. The coarsening of foam bubbles can be explained by the Laplace pressure. The Laplace pressure, which is the pressure difference between the inside and the outside of a curved surface, occurs between the small and larger foam bubble due to Ostwald ripening [109]. Hence, small bubbles, which have high pressure, cannot grow easily with time. The reason is that the particles reduce surface energy of bubbles. At the same time, the bubbles and dry solid particles squeezed together and the bubbles change from a free flowing state to a jammeu state. In order to observe the microstructural change, light microscope images at different times have been captured out. In Figure 5.4, the microstructures of wetted particles-liquid foam compared with Figure 5.3. The volume fraction of mixture is $n_0^{(s+w)4} = 0.64$ for Figure 5.4 (a) after 1 min., (b) after 10 min.

and (c) after 1 hour. From Figure 5.4, it is clearly seen that the bubbles did not deform in 10 min., but the structure of surface-wetted particles foam mixture deterioated completely after 1 hour. Only the microstructure of glass beads can be seen in Figure 5.4 (c). The water coming from wetted particles (absorbed by solid glass beads) causes deformation of the liquid foam during time. Consequently, the rigidity of the liquid foam decreases, and bubbles lose contact.

5.2.4 Rheological Characterization of Foam and Particle-Foam Mixtures

In this study, a rotational rheometer (Anton Paar, MCR301) was used for each rheological experiment, in combination with a plate-plate geometry, with 50 mm diameter. All experiments were conducted at room temperature, constant at $296\pm1°$K. However, it should be noted that the plate-plate geometry causes a slip effect at the interface between the foam and metal plate. Hence, the slip effect, which decreases the shear stress and thereby disrupts the continuity of flow, was decreased by using ordinary sand paper (P320) glued on the surface of the plate-plate geometry. It has a very fine grain diameter of 46.2 μm, and is water proof. Moreover, it can be glued easily onto the plate, where the gap distance between two plates was adjusted as $h = 1$ mm.
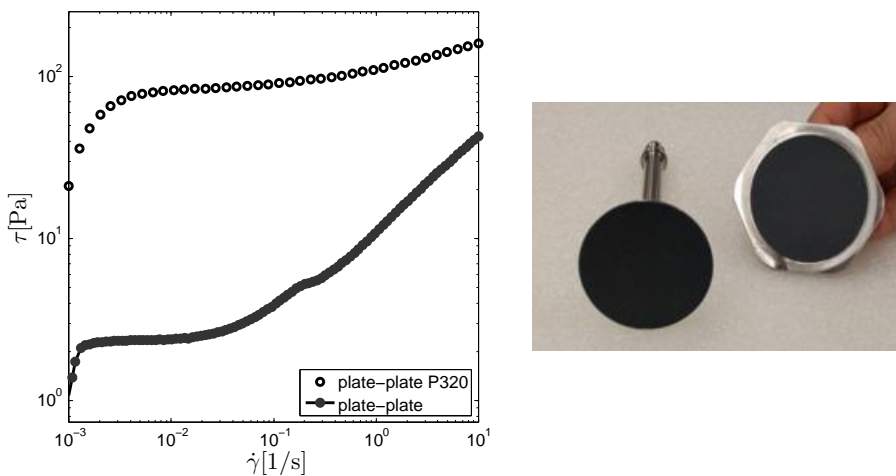
Figure 5.5: Flow curve test of liquid foam by using smooth plate-plate geometry and rough plate-plate geometry (with sandpaper P320).

The flow curve test shows two performances of both smooth and rough (P320) plate-plate geometries (Figure 5.5). The flow curve, which is obtained by using rough plates, is higher than the other. Two rheological experiments have been performed: Flow curve tests and oscillation tests (amplitude sweep

tests). For the flow curve test, the shear rate was given in a range from 0.0001 1/s to 10 1/s, and the total time of the experiment was 8 min. The amplitude sweep test was applied to the sample with varying range of deformation (strain) and constant frequency. The input strain ($\gamma = s/h$) was in a range from 0.01 % to 100 %, where s is the deflection during oscillation of the upper plate and h is the shear gap. The frequency has been kept constant at 1 Hz. Each rheological experiment was performed three times to check the repeatability, and the mean values of them were accepted as final results.

5.3 Results of Plate-Plate Investigation

5.3.1 Dry Particle-Foam Mixture

As explained in the second part, the dry particles were mixed with foam for 1 min. To perform all the experiments under the same conditions, pure foam was mixed for 1 min., too. Despite the mixture of the total volume dv was taken constant, after the mixing process, dv decreases due to decreasing volume of foam. Figure 5.6 shows that the biggest difference of the total volume is in the range between $n_0^{s4} = 0.15$ to $n_0^{s5} = 0.20$. Maybe, it can be explained by the jamming of the particles in the mixture. Over this range, solidity appears near critical volume fraction below which the material is a fluid whose viscosity or shear stress increases [53]. Hence, the solidity behavior of the mixtures prevents the performance of a flow curve test over $n_0^{s7} = 0.30$ volume of solid particles.
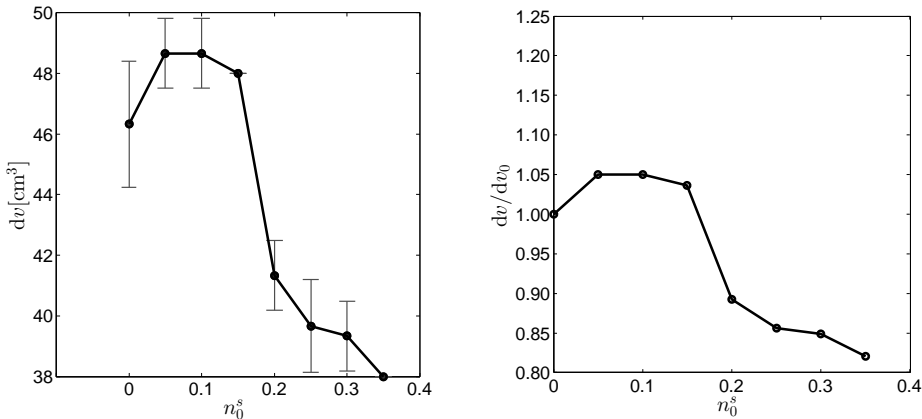
Figure 5.6: Total volume and normalized total volume of dry particle-liquid foam mixtures vs. volume fraction of dry particles

Flow Curve Test
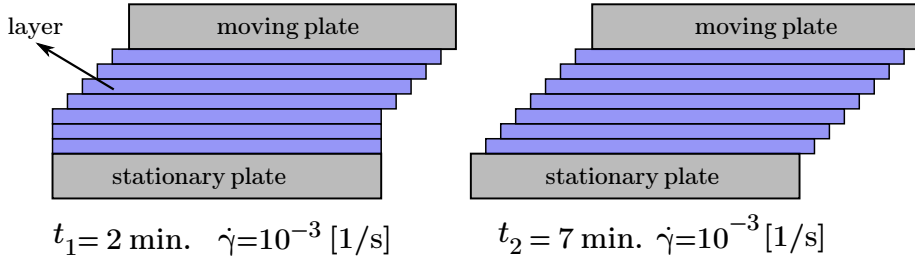
Figure 5.7: Transient viscosity effect for plate-plate flow

A flow curve of pseudoplastic materials, which was explained in Chapter 4, includes three regimes: A low-shear Newtonian plateau (constant viscosity), shear-thinning and second Newtonian plateau. However, the first regime (low-shear Newtonian plateau) can suppose a "transient viscosity peak", which occurs due to short measuring point durations [81]. For the plate-plate geometry, some layers, which are close to the moving upper plate, are shifted and other layers (near stationary bottom plate) need a certain period of time to move together (Figure 5.7). Therefore, to avoid the transient effect, the measuring point duration was set as a long period of time in the low-shear range.
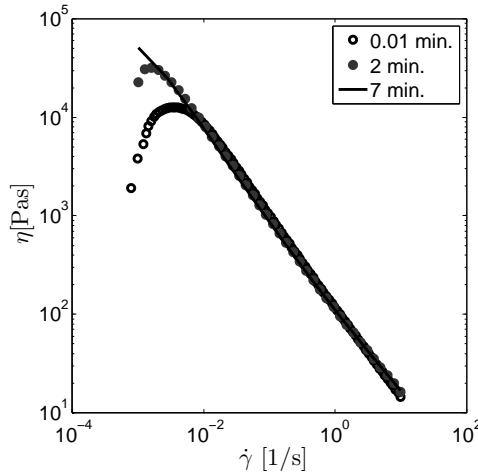
Figure 5.8: Transient viscosity peak in the low-shear range

As it is seen in Figure 5.8, the transient viscosity peak was avoided by using a longer time period for low-shear rate. If the curve, which has been obtained in short time, was taken as a result, it might be considered a Newtonian plateau,

and the results would have an error during fitting with rheological model. Thus, the flow curve tests have been performed without transient viscosity effect under a controlled shear rate. In order to show the influence of the solid particles on the liquid foam, the mixture of dry solid glass beads and liquid foam have been used with different volume fractions of glass beads up to n_0^{s7}. In Figure 5.9, the volume fraction of solid particles effects the flowability of the mixture; the shear stress increases with the increase in the amount of solid particles. For volume fraction $n_0^s > n_0^{s7}$, noisy data was collected. This phenomenon may be explained by the jamming point, which represents the transition from the freely flowing to the jammed state [115]. The mixture behaves more solid-like as far as the flowability is concerned.
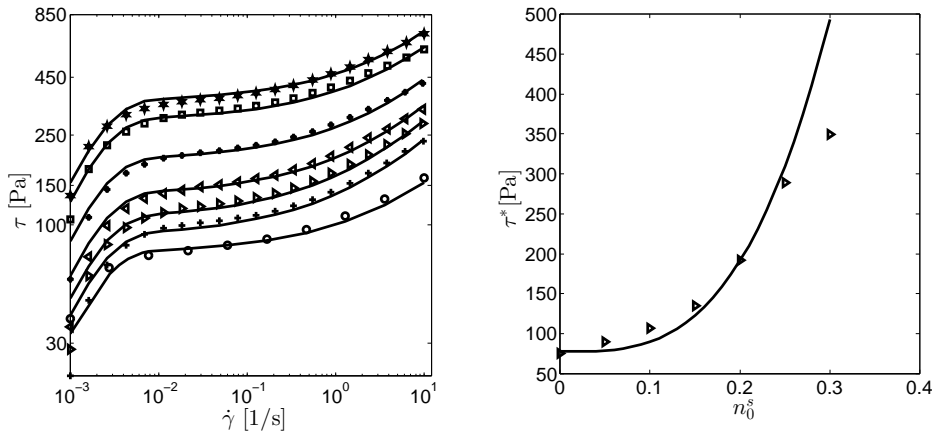
Figure 5.9: Herschel-Bulkley-Papanastasiou model fitted to the flow curve for different volume fraction of dry solid particle-liquid foam mixtures (left). From up to down; $n_0^{s7} = 0.3$, $n_0^{s6} = 0.25$, $n_0^{s5} = 0.2$, $n_0^{s4} = 0.15$, $n_0^{s3} = 0.1$, $n_0^{s2} = 0.05$, $n_0^{s1} = 0$. The shear stress τ^* vs. volume fraction of dry solid particles n_0^s, it shows that τ^* increases with increasing n_0^s (right).

In this flow curve test, the yield stress was determined by applying the modified versions of the Herschel-Bulkley-Papanastasiou model [90], cf. Eqn. 4.126 to the measured curves. The Herschel-Bulkley-Papanastasiou function gives infinite viscosity in the limit of zero shear rate and zero viscosity for infinite shear rate (Chapter 4). The function is not useful for some materials that have Newtonian plateaus in the low-shear rate. However, it is the best one for our flow curves. As it is mentioned above, viscosity does not have a constant value for longer periods of time and only the shear thinning regime was observed in our flow curve experiment. Hence, this function matches our experimental results very well.

This model (Eqn. 4.126) describes non-Newtonian behaviour after yielding

$$\tau = K \; \sqrt{\dot{\gamma}} + \tau^* \; (1 - \exp(-a \; \dot{\gamma})), \qquad (5.2)$$

where a is the exponent, K is fluid consistency, $\dot{\gamma}$ and τ^* are the shear rate and yield stress, respectively. The values of a, which controls the exponential growth of the stress [41], remained constant for pure foam and all mixtures (Table 5.3). Besides, the fluid consistency K varied for each flow curve, but it only effects the slope (viscosity) after the yield point. The composition of the particle-foam mixtures does not have any effect on the variety of the fluid consistency. The modification of this model depends on the function τ^*, which is dependent on the volume fraction of dry solid particles n_0^s. Figure 5.9 shows that the function τ^* increases with increasing the volume fraction of n_0^s. Equation 5.3 shows a relationship between τ^* and n_0^s where $A = 19606.9 \, \text{Pa}$ and $B = 77.29 \; \text{Pa}$

$$\tau^* = A \; (n_0^s)^{3.2} + B. \qquad (5.3)$$

The relation can be established by means of the non-linear equation and was obtained by using the yield points determined from flow curve test (Figure 5.9). Moreover, it might also be valid for different yield stresses, but this generalization requires further investigations through more rheological experiments.

Table 5.3: Fitting parameter from Herschel-Bulkley-Papanastasiou model

Case	1	2	3	4	5	6	7
$K[\text{Pas}^{1/2}]$	24.97	47.56	58.26	64.21	78.47	102.54	116.52
$\tau^*[\text{Pa}]$	75.12	89.23	106.38	134.65	192.49	288.69	349.57
$a[\text{s}]$	560	560	560	560	560	560	560

Amplitude Sweep Test

During oscillation tests (amplitude sweep test), the sinusoidal oscillation stress or strain is measured while varying (fixed) stress or strain signal is applied. After performing the oscillation test, the complex moduli are determined. They are divided into two parts which is explained for the complex shear modulus G^*; the real part is the storage modulus $G^{'}$ and the imaginary part is the loss modulus $G^{''}$. To gain insight about the stored elastic energy of the material, the storage modulus is considered and the loss modulus accounts for the viscous loss (of energy) of the material. Thereby, it is possible to obtain the viscoelastic behavior of the material. Thus, the amplitude sweep test was performed to determine the linear viscoelastic regime of the mixture at different volume
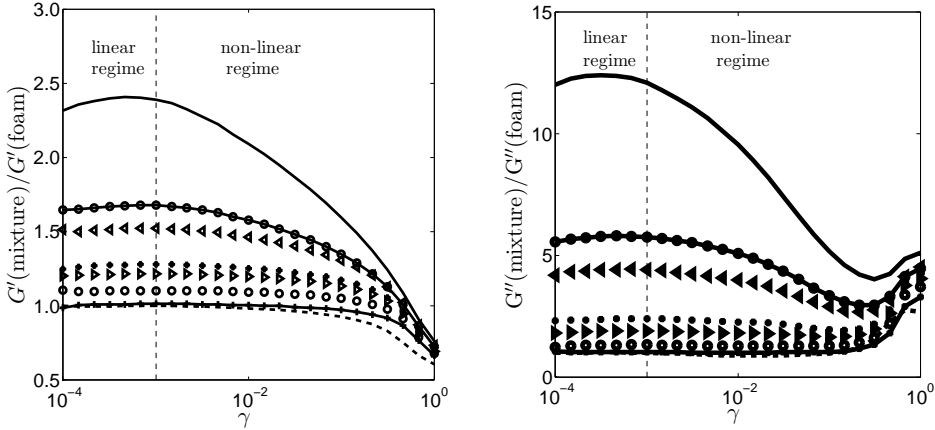
Figure 5.10: Amplitude sweep test: Normalized storage $G'(\text{mixture})/G'(\text{foam})$ and normalized loss modulus $G''(\text{mixture})/G''(\text{foam})$ vs. strain γ for different volume fraction of dry solid particles. From down to up; the curves are related to n_0^{s1}, n_0^{s2}, n_0^{s3}, n_0^{s4}, n_0^{s5}, n_0^{s6}, n_0^{s7}, and n_0^{s8}.

fractions n_0^s (dry solid glass beads and liquid foam mixture) containing particles of n_0^{si} ($i = [1, ..., 8]$).

In Figure 5.10, the storage modulus and loss modulus of each mixture were normalized by the storage and loss modulus of the pure liquid foam n_0^{s1}. The storage modulus is higher than the loss modulus for each mixture, which indicates the solid-like behavior of the mixture. Mardaru et al. [75] investigated liquid foam (Gillette Classic Sensitive, Procter & Gamble UK) and experimentally found that the storage and loss modulus are constant from 0.001 to 0.1 strain. The linear and non-linear regimes of pure liquid foam (n_0^{s1}) and particle-liquid foam mixtures are depicted in Figure 5.10 for shear strain γ from 10^{-4} to 10^0. The initial drop in the storage modulus represents non-linearity and structural breakdown. While the storage modulus decreases with increasing shear strain, γ, the loss modulus becomes higher than the storage modulus, explained by the transition from solid-like to liquid-like behavior of the mixtures (structural breakdown). In addition, the storage and loss modulus increase as n_0^s of particle increases. As it is seen in Figure 5.10, that the linear regime for the storage and loss modulus was obtained and shown until the vertical dashed line. On the other hand, values of storage and loss moduli are very close to each other for varying volume fractions n_0^{si} ($i = [1, ..., 5]$).

The values of the normalized storage and loss modulus were taken from a shear strain amplitude $\gamma = 0.001$ (cf. Figure 5.10), and at this value, a relationship was observed between both the normalized storage and loss modulus, and the volume fraction of particles, n_0^s (Figure 5.11). At the same strain value, the
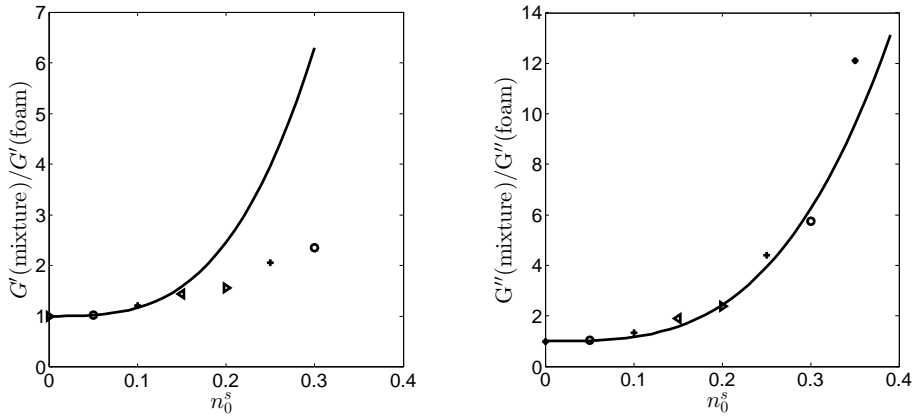
Figure 5.11: The storage and loss modulus were determined by using shear stress which is obtained from Eqn. 5.2 - 5.3 and fitted to the normalized storage $G'(\text{mixture})/G'(\text{foam})$ and normalized loss modulus $G''(\text{mixture})/G''(\text{foam})$ vs. n_0^s using linear scaling at $\gamma = 0.001$.

storage and loss modulus will provide the same results, if room temperature, pressure and volume fraction of the testing sample are constant. However, the experiments have been performed for different volume fraction of solid particles, and the moduli increased by the volume fraction of solid particles. In Figure 5.11, the solid curve of the storage and loss modulus was obtained by using the Herschel-Bulkley-Papanastasiou model and τ^* (Eqn. 5.2 and 5.3). Before fitting the obtained values to the experimental data (from storage and loss modulus vs. strain curves), they were first normalized w.r.t. the lowest one. The normalized storage modulus, in dependence to the volume fraction n_0^s, did not fit well for higher volume fractions of the particles, whereas the normalized loss modulus fitted well. This can be explained by the function of the yield stress (Eqn. 5.3) and Herschel-Bulkley-Papanastasiou model (Eqn. 5.2). Figure 5.11 shows that they can be used until n_0^{s4} for storage modulus.

5.3.2   Surface Wetted Particle-Foam Mixture

Flow Curve Test

The flow curve test has also been carried out for the wetted solid glass beads-liquid foam mixture. By using the wetted particles, the occurence of jamming effect can be shifted to a higher volume fraction, so that the shear stress of the high volume fraction of particles could be determined and the rheological behavior of them revealed. It was observed that the shear stress decreased,
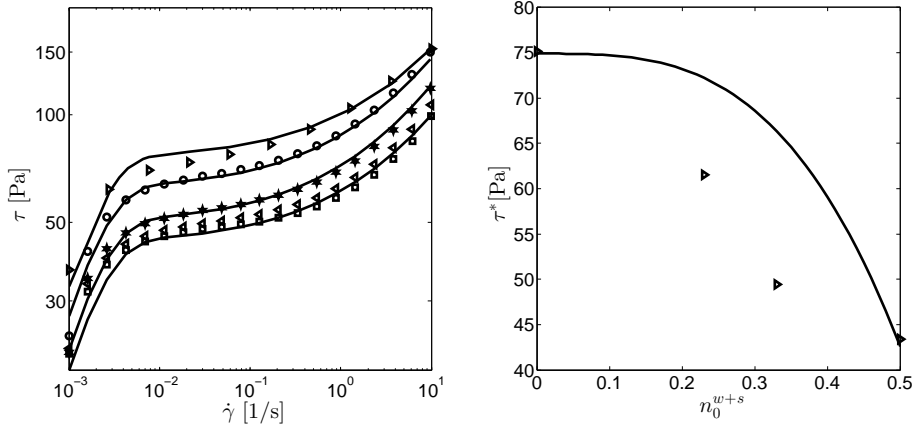
Figure 5.12: Modified Herschel-Bulkley-Papanastasiou model fitted to the flow curve test of the wetted particle-liquid foam mixture. From up to down, the flow curves are; pure foam, $n_0^{(w+s)1}$, $n_0^{(w+s)2}$, $n_0^{(w+s)3}$ and $n_0^{(w+s)4}$. The same fitting curve was used for $n_0^{(w+s)3} = 0.5$ and $n_0^{(w+s)4} = 0.64$ (left). The function τ^* increases with decreasing volume fractions of surface wetted particles.

despite the increase in the amount of wet particles. In addition, the shear stress of pure foam is greater than that of the mixture of surface wetted particle-liquid foam. The decrease in shear stress can be associated with increasing the amount of water, retained on the solid particles by surface forces. Thereby, the mixture flows freely. Zhand-Parsa et al. [123] investigated water films around the soil particles and explained that water thickness around soil particles is large at greater soil-water content. This phenomenon can also be observed by performing the flow curve test (Figure 5.12). The smallest shear stress data was obtained by using $n_0^{(w+s)4} = 0.64$.

Table 5.4: Fitting parameter from Herschel-Bulkley-Papanastasiou model

Case	1	2	3	4
$K[\text{Pas}^{1/2}]$	26.16	22.59	17.87	17.87
$\tau^*[\text{Pa}]$	61.53	49.48	43.39	43.39
$a[\text{s}]$	560	560	560	560

Equation (Eqn. 5.1) was also used to determine the yield stress of the surface wetted particle-liquid foam mixture. However, the Herschel-Bulkley-Papanastasiou model did not fit the experimental results as well as the experimental results of dry particle-liquid foam mixtures (Figure 5.12). For the vol-

ume fraction of surface wetted solid particles, $n_0^{(w+s)3} = 0.5$ and $n_0^{(w+s)4} = 0.64$, they are very close to each other; thus, only one fiting curve was used for them. Table 5.4 shows the parameters that were determined for surface wetted particle-liquid foam mixtures. The surface wetted particle-foam mixture causes function τ^* to decrease with increasing the volume fraction of pre-wetted particles. Thus, the relationship between τ^* and n_0^{w+s} can be represented by

$$\tau^* = A \ (n_0^{w+s})^{3.2} + B, \qquad (5.4)$$

where A and B are -297.25 Pa and 74.9 Pa, respectively.

Amplitude Sweep Test
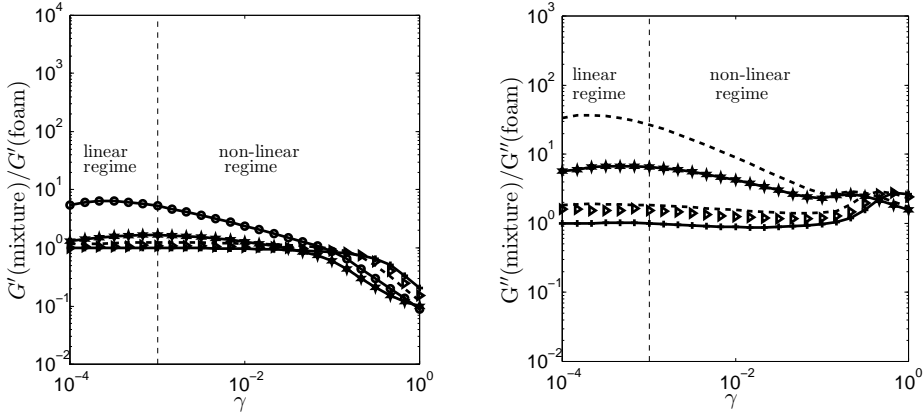
Figure 5.13: Normalized storage G'(mixture)$/G'$(foam) and normalized loss modulus G''(mixture)$/G''$(foam) vs. strain γ for $n_0^{(w+s)i}$. From down to up, n_0^{s1}, $n_0^{(w+s)1}$, $n_0^{(w+s)2}$, $n_0^{(w+s)3}$ and $n_0^{(w+s)4}$.

The normalized curves were obtained by performing amplitude sweep tests on up to $n_0^{(w+s)4} = 0.64$. After $n_0^{(w+s)4} = 0.64$, the linear regime disappears, and they change their solid-like behavior to liquid-like, more easily than other mixtures for small strains (Figure 5.13). Furthermore, the increase in the storage and loss modulus can be explained by increasing the amount of solid particles at the same strain. However, increasing the amount of particles increases the amount of water in the mixture as well, so that the mixture flowability increases simultaneously. Figure 5.14 shows the correlation between the volume fraction of particles, normalized storage, and loss modulus. Both the storage and loss modulus have a direct relation with the increase in the volume fraction of particles. The same equations, Herschel-Bulkley-Papanastasiou and

τ^*, were also used to fit experimental results for the pre-wetted particles-liquid foam mixtures but with different constant parameters.
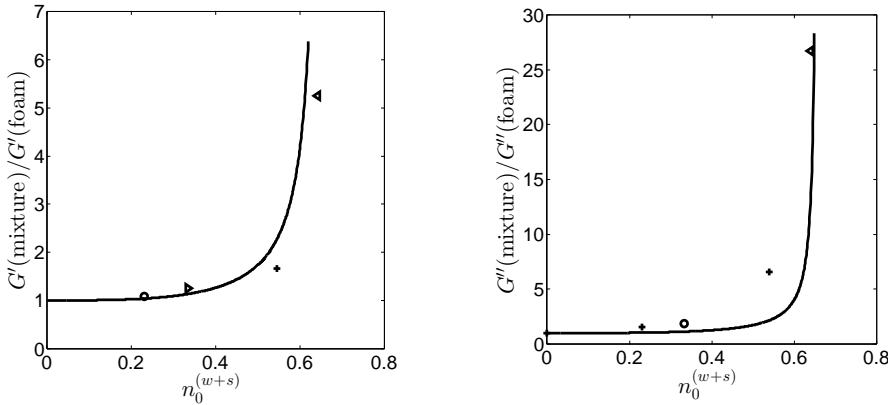
Figure 5.14: The storage and loss modulus determined by using shear stress which is obtained from Eqn. 5.2 - Eqn. 5.4 and fitted to the normalized storage $G'(\text{mixture})/G'(\text{foam})$ and normalized loss modulus $G''(\text{mixture})/G''(\text{foam})$ vs. n_0^{w+s} using linear scaling at $\gamma = 0.001$.

5.4 Discussion & Conclusion

The rheological model (Herschel-Bulkley-Papanastasiou model) has three constant parameters and enables us to match shear stress at very small shear rates. This model helps show the dependency of shear stress or viscosity on the volume fraction of the solid particles. A question arises from these results; are they really appropriate models and functions to use for different suspensions, such as hollow glass beads-foam mixtures? The dry particles (solid glass beads), liquid foam, and pre-wetted particles-liquid foam mixtures were investigated under strain rates in the rotational rheometer. The linear and non-linear viscoelastic regimes could be verified by the amplitude sweep tests. The rheological parameter (yield stress) of the mixtures were determined by Herschel-Bulkley-Papanastasiou model, which was used to fit with experimental results. The experimental data show a correlation between the normalized modulus and volume fraction of solid particles. The volume fraction of solid particles was increased until the mixture became rigid, indicating the jamming point. The flowability of the mixture was decreased and the shear stress could not be measured for the volume fractions of dry solid particles n_0^s greater than 0.3. To investigate the rheological behavior of the solid particles in a high volume fraction, water was added and the influence of it was obtained by performing rheological tests.

Chapter 6

Slip Effect on Particle-Foam Mixtures

6.1 Introduction

Liquid foam has wall slip effect on the rheological experiments. Shear flow profile with slip velocity u_s is shown in Figure 6.1. The wall slip effect is a big challenge for non-Newtonian fluids and the exhibition of the slip effect causes mistakes in the results of viscosity or measured shear stress. The viscosity measured with slip effect, is called the apparent viscosity. Two assumptions we are denoted as the Mooney and Oldroyd-Jastrzebski methods deal with slip effect [54, 85]. While the slip velocity depends on the shear stress for Mooney hypothesis, Oldroyd & Jastrzebski's hypothesis explain that the slip velocity depends both the shear stress and diameter on the pipe (gap distance between plate-plate geometry).
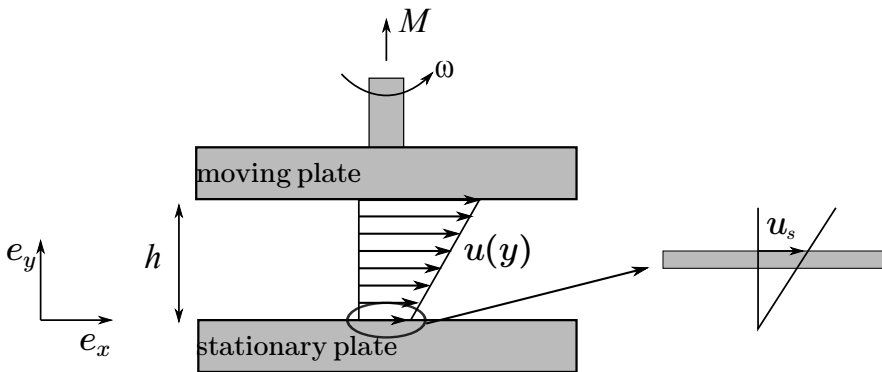
Figure 6.1: Shear flow geometry with slip velocity u_s, gap distance h, torque M and angular velocity ω.

The slip effect has been investigated in various papers [51, 78, 121] and both assumptions have been compared by many researchers. To avoid the slip effect, they usually used a grooved plate-plate geometry or serrated couette cell. Ahuja et al. [6] researched the slip velocity for concentrated suspensions of non-colloidal particles in Couette flow. They used both serrated and smooth types of Couette geometries (stationary cup and rotating bob) with the controlled rate mode. They showed that the apparent viscosity is much lower than the true viscosity for non-Newtonian fluid. On the other hand, Herzhaft [51] investigated the rheology of liquid foam with wall slip effect. They used parallel plate geometry, with a diameter of 35 mm, on a Haake Rotovisco RT20 rheometer. They performed the rheological experiments with different gap sizes (2 mm & 3 mm) for both smooth and grooved parallel plate geometries. The shear stress results, which were measured by the smooth type of plate geometry for different gap sizes, did not match due to slip effect. However, the experiments performed on different gap sizes on the grooved plate were superposed; therefore, they minimized the slip effect on the rheological experiments with rough surfaces. In addition, the Mooney and Oldroyd & Jastrzebski hypotheses were used and compared to determine slip velocity in [51]. They proved that the Mooney model cannot be applied to foam due to inconsistency with the experimental data obtained by means of grooved surface. On the other hand, aqueous foam with the slip effect was deeply researched by Marze et al. [78]. Their rheological measurements were obtained with a MCR 300 Rheometer (Anton Paar). A homemade cone plate geometry was used with polydisperse sand grains having a mean diameter of 100 μm. The cone diameter and angle are 175 mm and 0.175 rad, respectively. The experiments were performed at controlled shear rates. In [78], the experimental results (shear stress τ) of rough plate surfaces are 10x larger than the results of smooth plate for small shear rate and they proved it with flow curve tests. Yoshimura et al. [121] showed the slip effect for oil-in-water emulsions by using Rheometrics System IV rheometer with parallel disks of 26.85 mm radius and different gap distances: 0.5 mm and 0.75 mm. Although the experiments have not been performed with rough surfaces, they determined the slip velocity and showed that it depends on shear stress. Thus, they followed Mooney's hypothesis. After Yoshimura et al. [121], the slip effect of oil-in-water emulsion was researched by Bertola et al. [13]. At the same time, they also investigated commercial shaving foam by using a Rheologica Stress-Tech stress-controlled rheometer with a parallel disk geometry (40 mm diameter). The rheological experiments have been performed with smooth and rough plate surfaces. They compared the experimental results of the shear stress-appearent shear rate curves with theoretical results.

Many recent works have been pointed out the slip effect of liquid foam, both theoretically and experimentally. However, slip effect of surface wetted glass particles-foam mixture has not yet been reasearched with a visualization

method for rheological experiments. To determine the slip velocity in time, a camera (Imagesource DFK 31 BU 03.H) were used with 7x precision Zoom lenses and light source (Schott S80-55 (1021526)). In this study, we investigated the slip effect of shaving foam (Gillette Classic Sensitive, Procter & Gamble UK) and the surface wetted glass particles-foam mixture, by using glass plate-plate and metal plate-plate geometry with and without rough surfaces. Before the investigation of liquid foam and its mixture, we calibrated the type of geometry. To be more precise, we used standard fluid (APN145 and APN26) from Anton Paar GmbH having calibration certificate that gives the exact viscosity at the same temperature. Thus, the type of geometry can be easily calibrated with calibration fluid. On the other hand, the plate-plate with sandpaper geometry has been used to show the influence of roughness surfaces on the wall slip effect. Flow curve tests have been performed with three different gap distances (0.75 mm, 1.00 mm and 2.00 mm).

6.2   Rheological Experiments

6.2.1   Materials and Methods

APN26 (Anton Paar GmbH) is the calibration fluid used, with a dynamic viscosity and a density $\eta = 50.30$ mPas and $\rho = 0.8205$ g/ml at 293°K, respectively. Aditionally, APN145 (Anton Paar GmbH) was also used to measure the viscosity for small shear rate. The dynamic viscosity of APN145 is $\eta = 1105$ mPas at 293°K. All experiments were performed at room temperature $296° \pm 1°$K, except the calibration test. It was performed at $293° \pm 1°$K. However, we focused on the slip effect of shaving foam (Gillette Classic Sensitive, Procter & Gamble UK) and surface wetted glass particles-foam mixture. The average diameter of liquid foam and glass-particles, which was determined in [88], were $\bar{D} = 51.8$ μm and $\bar{D} = 48.5$ μm, respectively. A MCR 301 rotational rheometer (Anton Paar GmbH) was used with glass plate-plate and metal plate-plate geometries to perform rheological experiments. The geometries, such as glass plate-plate (g.p.p), metal plate-plate (p.p), and plate-plate with sandpaper (p.p sandpaper) were calibrated by using calibration fluid.

Table 6.1: Measuring System

Type of geometry	p.p	g.p.p	p.p sandpaper
Diameter, D [mm]	49.96	50	50
Measuring gap, h [mm]	1	1	1
Grain size diameter [μm]	-	-	46.2
Volume of material [ml]	1.96	1.96	1.96

As it is seen in Table 6.1, the measuring system is given for each geometry type with their properties. The sandpaper (P320) was cut as a circle, with diameter of 50 mm, and glued on top and bottom plate. The rheological experiments were performed for shaving foam and surface-wetted particle-foam mixture. The flow curve test was used to calibrate the type of geometries with calibration fluid. In order to show the effect of gap distances on the wall slip, the shear stresses of shaving foam and its mixture were measured in g.p.p, p.p and p.p sandpaper geometries with different gap distances; 0.75 mm, 1.00 mm and 2.00 mm. On the other hand, visualization method was used to determine slip velocity of the foam bubbles and particles close to the wall of the plate. The main idea of this method is that the slip velocity of the visualization method and the slip velocity of the flow curve tests can be compared easily.

6.2.2   Calibration of Different Type of Geometries
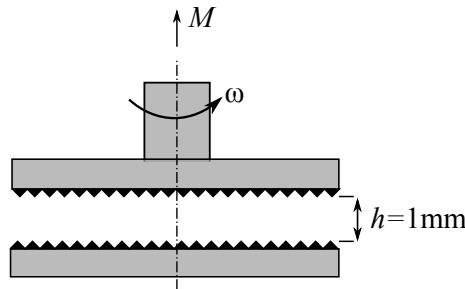
Figure 6.2: Gap distance for p.p sandpaper

Before starting the calibration test, the gap distance should be given as setting parameter for g.p.p, p.p and p.p sandpaper. The gap distance of g.p.p (Figure 6.2), p.p and p.p sandpaper was set at 1 mm. In order to get accurate results, the gap should be filled completely. However, the sample can flow out of the gap and also lead to mistakes in rheological tests. It should be trimmed to prevent the mistake during the tests.

As it is known the dynamic viscosity of a Newtonian fluid does not depend on the type of geometry. When rheological tests are carried out at the same conditions with different geometries for the same Newtonian fluid, the viscosity should always be identical, otherwise something is missing in the setup of the rheometer. Therefore, APN26, which is a Newtonian fluid, was used to calibrate the geometries. The flow curve tests were carried out to determine shear stress and viscosity vs. shear rate curves in Figure 6.3. The apparent shear rate $\dot{\gamma}$ was varied logarithmically over a range of 100 1/s - 600 1/s. Below 100 1/s with the torque M from 10^{-8} Nm to 10^{-3} Nm, the viscosity of the APN26 may be measured, but in this range, it gives noisy data (some negative results) because of low viscous sample. In order to measure the viscosity of the
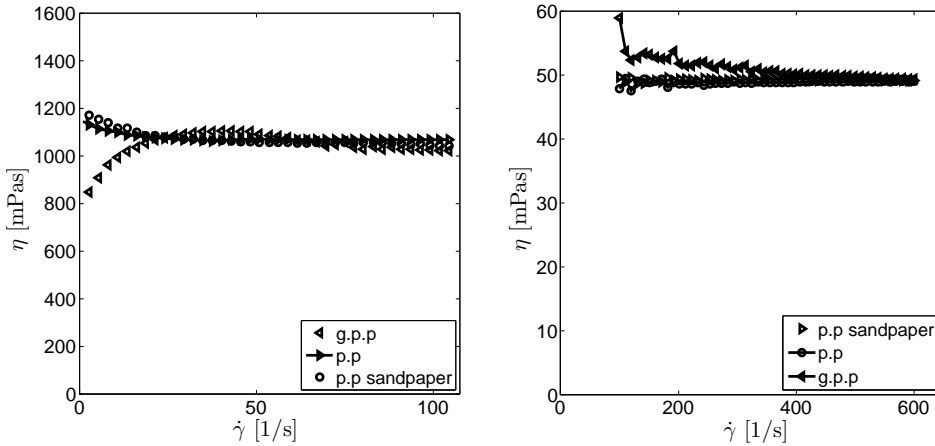
Figure 6.3: The viscosity-shear rate curves for APN145 (left) and for APN26 (right) by different surface of geometry

material below 100 1/s, the APN145 was used. The results of all geometries for same calibration fluid are closed each other and give approximately the same viscosity. It shows that the type of geometries were calibrated and can be used for different samples like non-Newtonian fluids. Even though the viscosity vs. shear rate test of g.p.p gives approximately the same data as p.p and p.p sandpaper, the viscosity, which was measured by g.p.p, has different values at the begining of the experiment. The deviation between the g.p.p and p.p sandpaper (Figure 6.3, right) might be caused by local flow on rough surface. It should be noted that the sandpaper was glued to the plates which were also produced for these experiments and have the exactly same dimensions compared to the original ones.

6.2.3 Flow Curves of Liquid Foam and Surface Wetted Particle-Foam Mixture

In Figure 6.4, we carried out flow curve tests for foam and surface wetted particle-foam mixtures at room temperature. Different type of geometries were used to compare shear stress of foam over shear rate. The shear rate was given as an input parameter and varied logarithmically for each test. We know that liquid foam behaves like a non-Newtonian pseudo-plastic material, which can be described by the Herschel-Bulkley-Papanastasiou, the Bingham, or the power law model. In this study, we wanted to show the variety of flow curves, by measuring rough and smooth surfaces on p.p and g.p.p. The variety of the experimental results occurs due to complexity (slip effect) of the non-Newtonian fluid. When the slip effect is minimized, the shear stress increases
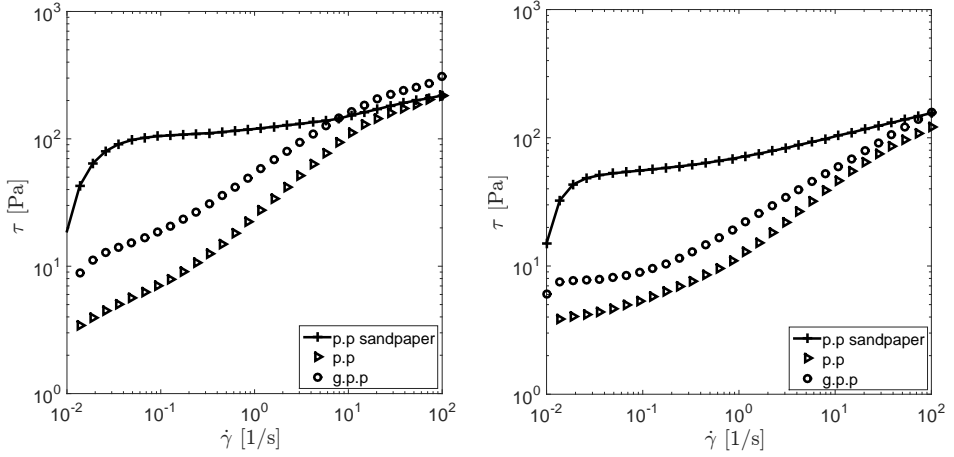
Figure 6.4: Flow curves for pure foam (left) and surface wetted particle-foam mixtures (right) obtained with different measurement devices (plate-plate).

at small shear rate (Figure 6.4). The shear stress, which was obtained by p.p device, is approximately 10 times larger than the shear stresses measuring by smooth surfaces (p.p and g.p.p). This result is qualitatively as same as the result of Marze et al. [78] for Sodium Dodecyl Sulfate (SDS) foam. They compared shear stress versus shear rate curves by using smooth and rough plate surfaces. In order to get a rough surface, they covered the cone-plate geometry with polydisperse sand grains. The slip effect can be seen for pure foam in Figure 6.4 on the left and surface wetted particle-foam mixture in Figure 6.4 on the right. The surface wetted particle consists of $n_0^w = 0.55$ volume fraction of distilled water and $n_0^s = 0.45$ volume fraction of solid glass beads. From this mixture, $n_0^{(w+s)1} = 0.23$ volume of wetted solid glass beads was taken to mix with $n_0^{f1} = 0.77$ volume of shaving foam. Although the shear stress vs. shear rate curves have different values, p.p and g.p.p show same attitude for both pure foam and its mixture.

Wall Slip Effect on Liquid Foam and Surface Wetted Particle-Foam Mixture

The wall slip velocity is a non-zero tangential velocity of the fluid at the wall. The wall slip is a big challenge during rheological tests, especially for liquid foam due to its complex flow behavior and the existence of a thin liquid film near the wall. The foam bubbles could have been sliding at the interface between the plate-plate geometry. This phenomenon causes a lower effective measure of shear stress and viscosity. The slip effect also disrupts continuity of flow and it can be divided into two groups; "true slip" and "apparent slip".

True slip is a discontinuity in velocity at the wall and especially, it can be seen in polymer melts. However, apparent slip occurs due to large velocity gradients and it can be seen in gels, foam and concentrated suspensions etc. Walls et al. [118] explained that a thin liquid film exists next to the wall with the particles either not interacting with the wall or interacting weakly in suspensions. The slip effect on the liquid foam was handled by many researchers. Besides, we handled the slip effect on liquid foam and on wetted particle-foam mixtures. The no-slip condition between a fluid and a solid boundary in contact with the fluid is one of the most classical assumptions in fluid mechanics. Therefore, we need to minimize or eliminate the slip effect which is possible with sandpaper. In order to minimize the slip effect, we should use rough surfaces. The surface of the plate-plate geometry can be ribbed, or sandpaper can be glued on it. We used sandpaper for our experiments. On the other hand, to determine slip effect three different gap distances (0.75 mm, 1.00 mm and 2.00 mm) are used with smooth and rough surfaces. In order to use a smooth surface, the experiments have been performed with a plate-plate geometry made out of metal and glass surfaces. The glass surface was used to get visualization of the sample easily.

The slip velocity was determined with two hypotheses of Mooney and Oldroyd-Jastrzebski [54, 85]. For the Mooney model, the slip velocity depends only on the shear stress ($u_s = \alpha\tau$). However, the slip velocity depends on the both the shear stress and pipe diameter or gap distance D_p ($u_s = (\beta/D_p)\tau$) for the Oldroyd-Jastrzebski model. The parameters α and β are proportionality constants. Yoshimura et al. [121] investigated the slip effect of the oil water emulsion by following Mooney's hypothesis. They researched the slip effect with two different gap distances. The actual "$\dot\gamma_{ac}$" and appearent "$\dot\gamma_{app}$" shear rates were also explained and a mathematical equation for the correction of the wall slip was obtained with the slip velocity u_s (Figure 4.9)

$$\dot\gamma_{app} = \dot\gamma_{ac} + \frac{2u_s}{h}. \tag{6.1}$$
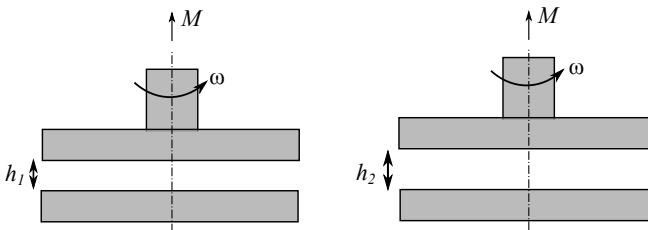
Figure 6.5: Plate-plate geometry with different gap distances

The actual shear rate can be determined by two diferrent gap distances

$$\dot{\gamma}_{ac} = \frac{h_1 \; \dot{\gamma}_{app1}(\tau) - h_2 \; \dot{\gamma}_{app2}(\tau)}{h_1 - h_2}, \tag{6.2}$$

where h_1 is the first gap distance and h_2 is the second gap distance at the flow curve test (Figure 6.5). The viscosity and shear stress can be determined from the actual shear rate. The slip velocity depending on the shear stress (τ) can be seen in Eqn. 6.3.

$$u_s = \frac{\dot{\gamma}_{app1}(\tau) - \dot{\gamma}_{app2}(\tau)}{2(\frac{1}{h_1} - \frac{1}{h_2})}. \tag{6.3}$$

In [121], viscosity was determined by using a power law model which is the simplest way to obtain viscosity and shear stress. However, Enzendorfer et al. [29] and Herzhaft [51] revealed that the Mooney hypothesis cannot be applied to liquid foams, since it causes the determined negative actual shear rates which are nonphysical. Herzhaft [51] applied the Oldroyd-Jastrzebski model to their experiments and the apparent shear rate was written by using Eqn. 6.1

$$\dot{\gamma}_{app1} = \dot{\gamma}_{ac} + \frac{2\beta\tau}{h_1^2} \qquad \dot{\gamma}_{app2} = \dot{\gamma}_{ac} + \frac{2\beta\tau}{h_2^2}. \tag{6.4}$$

The actual shear rate can be determined with in the square of the two gap distances (h_1^2 and h_2^2)

$$\dot{\gamma}_{ac} = \frac{h_1^2 \; \dot{\gamma}_{app1}(\tau) - h_2^2 \; \dot{\gamma}_{app2}(\tau)}{h_1^2 - h_2^2}. \tag{6.5}$$

The wall slip effect of a shaving foam was also determined by Leong et al. [65]. They used the experimental data of the shaving foam from Bertola et al. [13]. Their experimental results (the steady shear data) were converted into a shear stress-shear rate function and shear stress-slip velocity function with Tikhonov regularization method.

In order to show the slip effect on the liquid foam, and especially on the surface wetted particle-foam mixture, the Oldroyd-Jastrzebski hypothesis was used. From the flow curve test, the appearent shear rates were obtained at the same shear stresses and used to calculate actual shear rate "$\dot{\gamma}_{ac}$". The slip velocities were calculated at 0.75 mm - 1 .00 mm and 2.0 mm. The liquid foam and the surface wetted particle-foam mixture was compared with their slip phenomena.

Wall Slip Effect Through Image Analysis

A visualization method was performed by some authors to get evolution of foam structure and slip velocity. Herzhaft [51] used a CCD camera to obtain the structure and size of the foam bubbles. In addition, the slip velocity was determined for foam. The slip effect in pastes of soft particles was also investigated by Meeker et al. [80]. They used a Haake RS 150 stress-controlled rheometer with cone-plate geometry and microgel pastes was imaged onto a camera with zoom lenses.
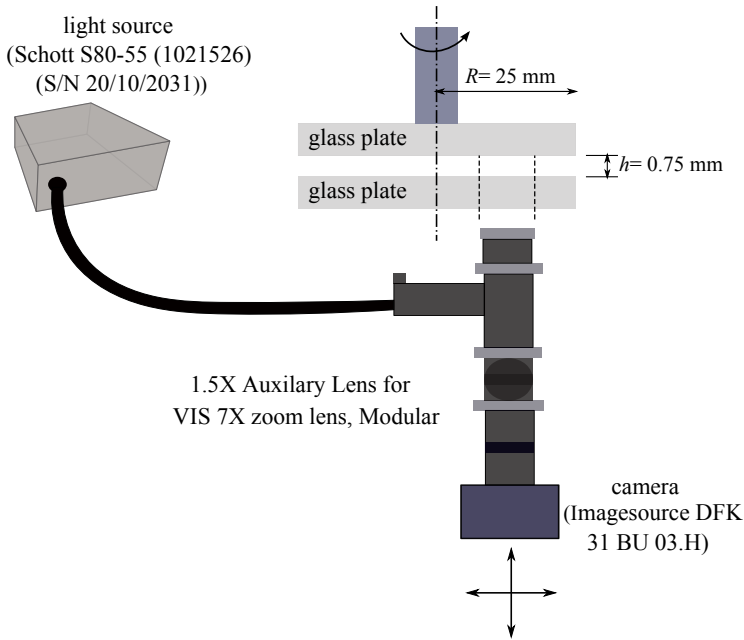
Figure 6.6: The sketch of the glass plate-plate with camera

In this study, visualization method is used to determine slip velocity of liquid foam (Gillette Classic Sensitive, Procter & Gamble UK) and pre-wetted glass particles-foam mixture during rheological measurements. To capture flow velocity fields, Particle Image Velocimetry (PIV) can also be used. However, it is not suitable compared to the visualization method due to its costs and need for specialised user.

Images were obtained by IC capture software. The software is manufactured by The Imaging Source, which includes video converters. By using this software, single images or image sequences can be saved manually. Additionally, it is also possible to save image sequences via a timer. A camera (Imagesource DFK 31 BU 03.H, The Imaging Source), which is connected to the software, was fixed under the glass plate (Figure 6.6), making it possible to see the movement of the particles and foam bubbles. Therefore, we can only show

images which were obtained with glass plate geometry.

Figure 6.7: Top view of the glass plate with printed transparent paper

For foam and particle visualization, the camera was used with 1.5X Auxiliary Lens for VIS 7X Zoom lenses (Edmund Optics (EO)). The magnification of the lens is 1.5X. The camera records 15 pictures per second and the dimension of the picture is 720*480 pixels. For calibration, pixels should be converted to mm. Thus, we drew circles with their centerline having a same centerpoint with different diameter (Figure 6.7). The center of the circles is overlapped with the center of bottom glass plate geometry. The circles were printed on transparent paper and the paper was put on the bottom of the glass plate (Figure 6.7). It was fixed up glass plate to visualize out of the center of the glass plate with the camera. The visualization was syncronized with the flow curve test to get the results at the same time. The shear rate range was used to measure the velocity of the bubbles and particles. For visualization method, we specified four points in the corners of the video frame (Figure 6.8, left). The edge from 1 to 2 is the bottom side and 3 to 4 is the top side of the image. The dimension of the video is in pixels and must be converted to mm. We determined that 1 pixel is equal to 0.14 mm. In order to get the tangential velocity (slip velocity) with visualization method, we need to determine angular velocity between two bubbles. As it is mentioned before, the non-zero tangential velocity at the wall gives the slip velocity. The tangential velocity can be determined

$$u_t = \omega r = \frac{2 \ \pi \ r \ \psi}{360(t_2 - t_1)}, \tag{6.6}$$

where r is the radius, ψ is the angle between two points from t_1 to t_2 and t is the time. The unity of the slip velocity is in mm/min. We convert it to mm/sec. From the tangential (slip) velocity, the actual shear rate was determined by Eqn. 6.4.
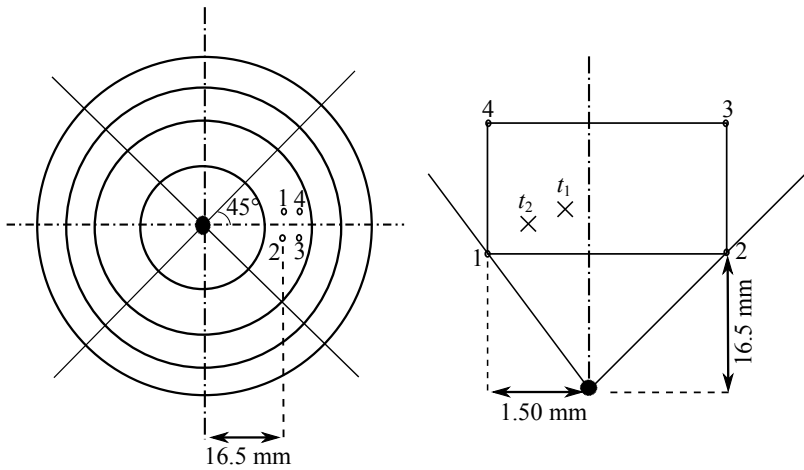
Figure 6.8: The fixed circles with a same centerpoint were printed out on the transparent paper (left). The locations of four points from 1 to 4 were obtained by using camera (right). The location of the center point was also fixed.

In order to determine the tangential velocity, the angle between two bubbles must be known. A fixed circle can be obtained by three points and one point is the center of the circle, which is seen in Figure 6.8. The other two points were obtained from the movement of the bubbles at fixed time.
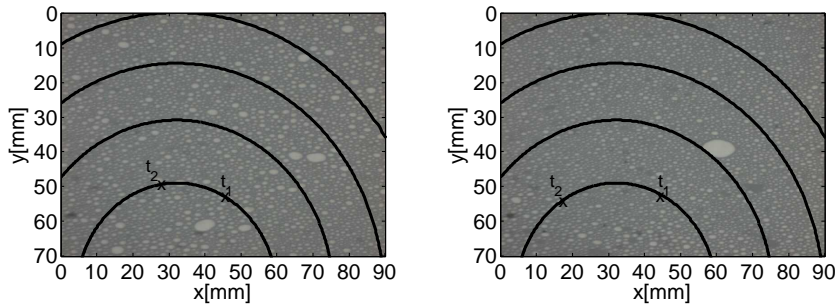
Figure 6.9: Images were obtained for pure foam (left) and surface wetted glass beads-foam mixture (right) by performing flow curve test at constant shear rate. The smooth glass plate with 0.75 mm gap distance is used for visualization method.

We focused on bubbles that flow at a constant shear rate and specifeid it in the video. The video at 0.04 min was saved as a jpeg file. By using the jpeg file in Matlab, the location of the bubble was found to be at 0.04 min. The

same procedure was also repeated for the same bubble at 0.12 min. The shear rate was taken constant for flow curve test to determine slip velocity easily. Different shear rates such as 0.1 1/s, 0.5 1/s, 1 1/s and 5 1/s were used to show the effect of the shear rate on the slip velocity for pure foam. Additionally, the shear rate 10 1/s was also applied to the surface wetted particle-foam mixture. The reason is that the shear rate 5 1/s corresponds to the shear stress 43 Pa is not possible to compare with high shear stresses. For each shear rate, the same procedure was applied. This visualization method was used for both pure foam and surface wetted particle-foam mixture. In Figure 6.9, an example for pure foam (left) and surface wetted particle-foam mixture were obtained with circles in Matlab. As explained above, when we determined the location of the bubble, specified time ($t_1 = 0.04$ min, $t_2 = 0.12$ min) was used, except the experiment at 5 1/s. The shear rates (5 1/s and 10 1/s) are very high to fix the location of the bubble; therefore, the time difference between two points (bubbles) was taken smaller than other shear rates. The second point was fixed at $t_2 = 0.06$ min for 5 1/s. On the other hand, the tests of the surface wetted particle-foam mixture show that the bubbles of mixture move faster than the bubbles of pure foam due to distillized water. Therefore, the time difference was taken as 0.01 min ($t_1 = 0.03$ min, $t_2 = 0.04$ min) for the highest shear rate (10 1/s).

6.2.4   Experimental Results
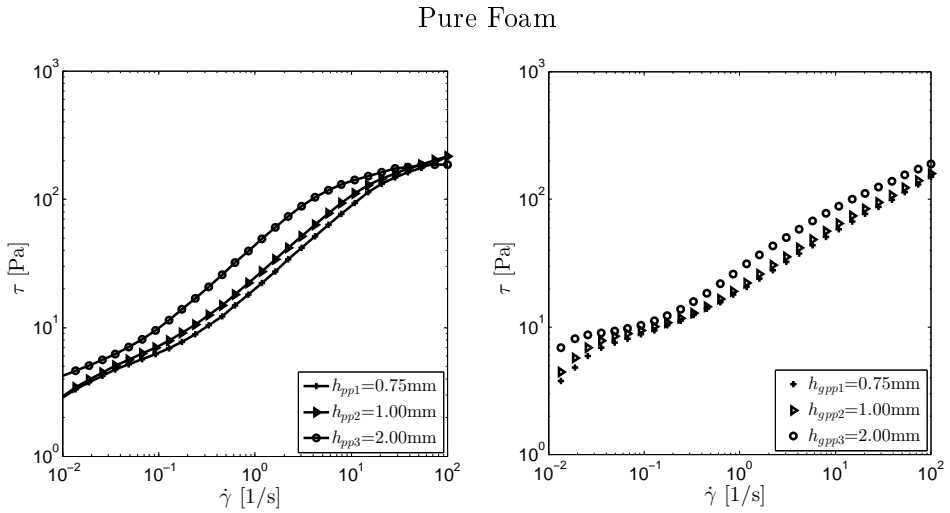
Figure 6.10: Flow curve test of liquid foam for different gap distances (0.75 mm, 1.00 mm and 2.00 mm) by using plate-plate (left) and glass plate-plate surfaces (right).

The experimental data of liquid foam with plate-plate and glass plate-plate

are presented in Figure 6.10. During the tests, the sample was subjected to shear rate that increased logarithmically with time from a low value to a high value of shear rate, and then the resulting shear stress was measured. As mentioned above, both of the flow curves show that the liquid foam behaves like shear-thinning (pseudo-plastic) materials. The shear stress increases with increasing the shear rate. Although the plate-plate and glass plate-plate geometries show a similar treatment for the flow behavior, the shear stresses of glass plate-plate are higher than the shear stresses of plate-plate. In order to check the flow curve test of the liquid foam for different gap distances, it is clear that different shear stresses were measured due to slip velocity. If the gap distance is increased, the shear stress increases for both metal and glass plate surfaces.

Glass Bead-Foam Mixture
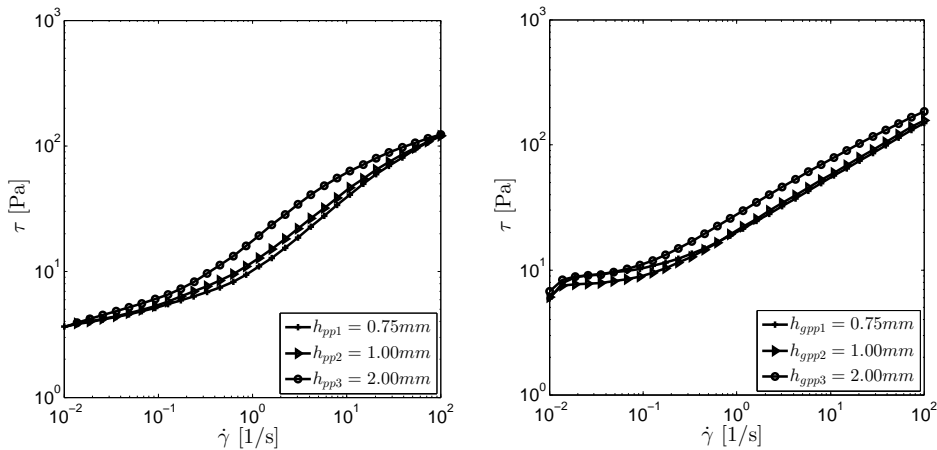
Figure 6.11: Flow curve test of surface wetted glass beads-foam mixture for different gap distances by using plate-plate (left) and glass plate-plate surfaces (right).

Slip effect increases complexity of the liquid foam. When we mixed it with pre-wetted particle, it became more complex in its slip behavior. Therefore, the test of the surface wetted particle-foam mixture has also been performed to show the rheological behavior with slip effect (Figure 6.11). Obviously, we can see that the shear stress of the mixture is smaller than the shear stress of the pure foam for both the plate-plate and the glass plate-plate geometries. It shows the effect of the distilized water, which decreases the viscosity and the shear stress of the mixture. In order to compare both smooth and grooved surfaces, the experiments of the pure foam and the surface wetted glass particles-foam mixture were done by using the plate-plate sandpaper geometry. In Figure 6.12, the shear stress for both materials, which is higher than the smooth geometries, starts at 10 Pa. It is very well known that the appear-

ent shear stress becomes smaller with the slip velocity. Hence, the rheological results of the grooved surfaces should be higher than the smooth surfaces. On the other hand, Figure 6.12 shows that variety of the gap distance does not effect on the grooved surfaces. In addition, the shear stress, which is obtained by different gap distance, is not the same value for very small shear rates. For both pure foam and surface wetted glass particle-foam mixture, the variation of shear stress is not huge between small and high shear rates.

Sandpaper Geometries
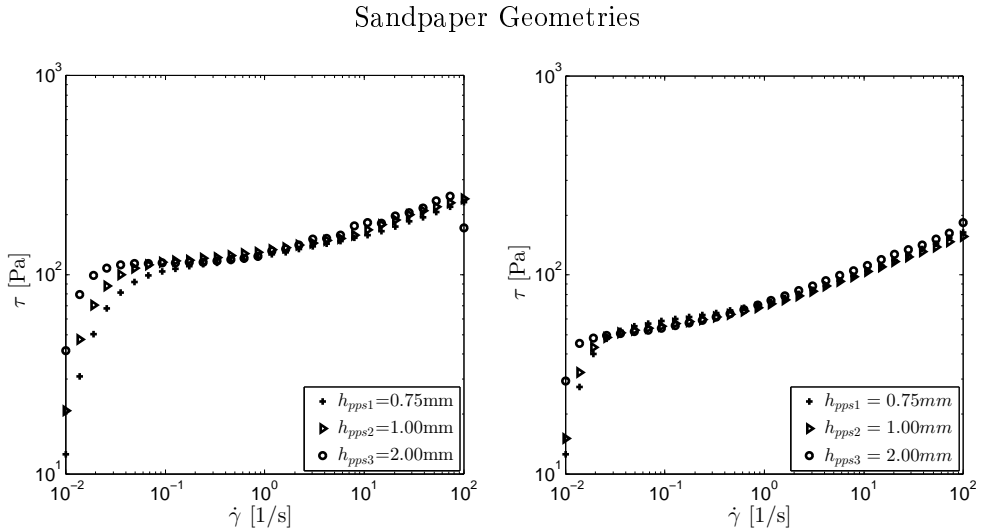
Figure 6.12: Flow curve test for different gap distances of liquid foam (left) and surface wetted glass beads-foam mixture (right) by using plate-plate sandpaper geometry.

The slope of the flow curve (viscosity) of the grooved surfaces is smaller than the viscosity of the smooth surfaces. On the contrary, the shear stress, which was measured by using smoooth surfaces, have a wide range of shear rate. The slip velocity has even more influence on the shear stress at small shear rate and few influence at high shear rate for smooth surfaces. Thus, the variety from the first to last shear stress is very high. The slip velocity of both plate-plate and glass plate-plate geometry is determined by using Eqn. 6.3 and the slip velocity from image analysis is calculated by Eqn. 6.6. The three different slip velocities, with respect to shear stress, can be seen with their error bars in Figure 6.13 (left). In order to determine the slip velocity, each flow curve test was performed three times with new samples. In addition, the slip velocities of the different gaps 0.75 mm-1.00 mm, 1.00 mm-2 mm and 0.75 mm-2.00 mm were summarized to calculate the average of slip velocity for plate-plate and glass plate-plate geometries (Figure 6.13). When the error bars of the plate-plate geometry are considered, the velocities of different gaps are the same at low and high shear stresses. For the glass plate geometry, the

error bars show that the slip velocities do not give the same values for different gap distances at high shear stress. However, they are nearly the same at very low shear stress. The slip velocity of the visualization method is the average of four rheological experiments. The slip velocity from visualization method is very close to the slip velocity of the glass plate-plate for pure foam.
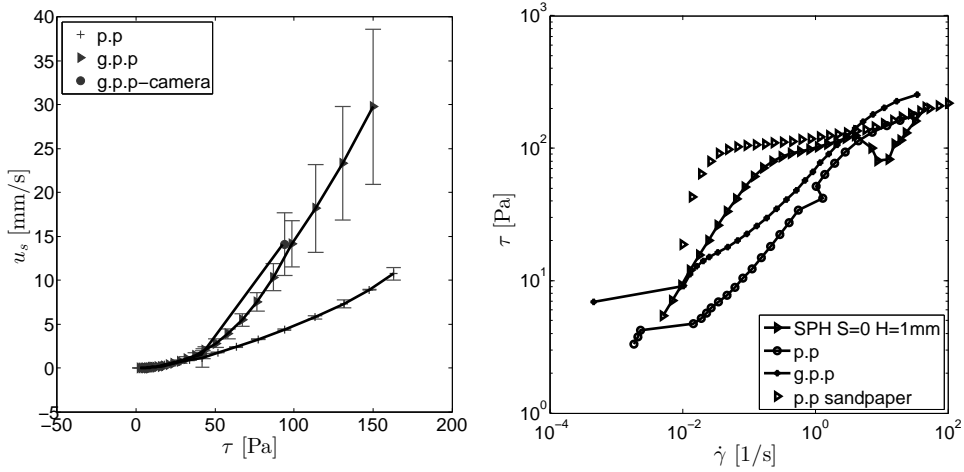
Figure 6.13: Average of the slip velocity for p.p, g.p.p and g.p.p with camera for liquid foam (left), corrected data for Jastrzebski & Oldroyd model by using g.p.p and p.p surfaces, determined data from SPH method (S = 0 (no slip)) and measured data by using p.p sandpaper geometry for liquid foam (right).

The actual shear rates have positive values for plate-plate (p.p) by using the Jastrzebski & Oldroyd model. Contrary to plate-plate (p.p), all the actual shear rates of glass plate-plate (g.p.p) are not positive, when the Mooney model was used. On the other hand, the actual shear rate, which is determined from visualization method, are also negative. Thus, they are not shown in Figure 6.13 (right). At low and high shear rates, the corrected data of the Jastrzebski & Oldroyd model is not consistent with the experimental data that was recorded by using plate-plate sandpaper (p.p sandpaper). In order to compare the corrected data at low and high shear rates, the Smoothed Particle Hydrodynamics (SPH) method [107] was used to determine the actual shear rate vs. shear stress curve for comparable systems. The SPH method was extended by a non-Newtonian [77, 124] and quasi-incompressible fluid flow, and a modified Herschel-Bulkley-Papanastasiou model. The modified Herschel-Bulkley-Papanastasiou model (Eqn. 5.2) has three constant parameters [88] for pure foam and particle-foam mixture $n_0^{(w+s)1} = 0.23$. The fluid consistency K is 24.97 Pas$^{1/2}$ and the exponent a is 560 s while the yield stress is 75.12 Pa for pure foam. In addition, K is 26.16 Pas$^{1/2}$ and a is 560 s while the yield

stress is 61.53 Pa for $n_0^{(w+s)1} = 0.23$. When we consider the range of shear rate from 0.01 1/s to 0.05 1/s, the flow curve from the SPH method is difficult to compare to the other curves (Figure 6.13, right). However, the SPH method shows that the curve for no slip matches the curve of p.p sandpaper very well over the 0.05 1/s shear rate. In Figure 6.13 (right), the noisy data of the SPH method can be explained by the inaccurateness of particle discretization. Although the Jastrzebski & Oldroyd model is used to determine the actual shear rate of the p.p, g.p.p and g.p.p with camera, they are not corrected well and they have already the slip effect. The Jastrzebski & Oldroyd model is not enough to minimize the slip effect in rheological experiments.
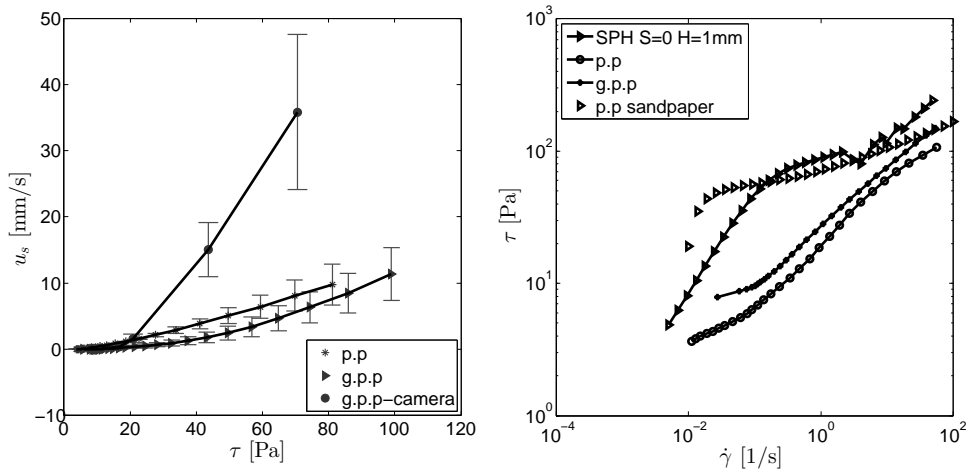
Figure 6.14: Average of the slip velocity for p.p, g.p.p and g.p.p with camera for pre-wetted particle-foam mixture (left), corrected data for Jastrzebski & Oldroyd model by using g.p.p and p.p surfaces, determined data from SPH method (S = 0 (no slip)) and measured data by using p.p sandpaper geometry for pre-wetted particle-foam mixture (right).

The slip velocities and the corrected data were also computed to surface wetted particle-foam mixture and can be seen in Figure 6.14. The slip velocities, which were determined for surface wetted particle-foam mixture, are smaller than the slip velocities of pure foam. It can be explained by the instability of the mixtures. The stability of foam increases with the particles. Furthermore, the influence of wetted surface cannot be ignored since it decreases the viscosity and the shear stress of the foam mixture. This effect can be substantiated with Figure 6.13 and Figure 6.14. When we compared the shear stress of the surface wetted particle-foam mixture (Figure 6.14) to the shear stress of the liquid foam (Figure 6.13), the shear stress of mixture is smaller than the shear stress of the liquid foam. The Jastrzebski & Oldroyd model was also used to determine the actual shear rate of surface wetted particle-foam

mixture. On the contrary, the values of actual shear rates of surface wetted particle-foam mixture determined by Jastrzebski & Oldroyd model are positive for both plate-plate and glass plate. As it is established by Herzhaft [51] , the Jastrzebski & Oldroyd model is more adequate than the Mooney model for foam behavior. In order to get accurate results, the Jastrzebski & Oldroyd model can be used for foam and its mixtures. In Figure 6.14, the flow curve of SPH method are close to the flow curve of p.p sandpaper over 0.05 1/s shear rate. Additionally, the actual shear rates, which were corrected by the Jastrzebski & Oldroyd model, have slip effects and they do not give the same results as the experiments of the p.p sandpaper.

6.3 Conclusion and Discussion

The slip effect is very important for rheological experiments. In order to understand the slip effect some rheological tests were performed. Especially, the visualization method was used to capture pictures with slip phenomena. Furthermore, the slip velocity and corrected shear rate were calculated by using Jastrzebski & Oldroyd models. The measurement devices were calibrated with calibration fluids (APN26 and APN145). Until now, researchers did not mention calibration tests, but they should also be taken into account, to improve the reliability of results. The slip effect has been investigated with three different gap distances of the plate-plate and glass plate-plate geometries. In order to compare the liquid foam to the surface wetted particle-foam mixture, flow curve tests were performed and the slip velocities were determined. The visualization method can also be used to determine slip velocity. The measured shear stress and viscosity of the surface wetted particle-foam mixture is smaller than the pure foam due to the use of distillized water and its effects on the structure of the liquid foam. In addition, the Mooney hypothesis is not suitable to determine the slip velocity of foam or its mixture. This is because the corrected data, which follows the Mooney hypothesis, has negative values and the negative shear rates are unphysical. Contrary to the Mooney hypothesis, the Jastrzebski & Oldroyd hypothesis can be used since the corrected shear rates are positive. However, it is not possible to say that the corrected data does not include the slip effect. The actual shear rates, which were determined by the Jastrzebski & Oldroyd hypothesis, were not corrected well. The phenomena can be shown with the SPH method. The rheological experimental results of the plate-plate sandpaper and the results of SPH method for no slip are very close to each other. On the other hand, the actual shear rates of the p.p, g.p.p and plate-plate camera do not have the same results of the p.p sandpaper and SPH method.

Chapter 7

SPH Method and Mini Slump Test

7.1   Introduction

In the construction industry, such as earth pressure balance (EPB) tunnelling, a mixture of soil and water is used for the excavation process. Thus, the primary application range of the EPB machine, which can be conditioned only by water, is in fine-grained soil $d \leq 0.063$ mm [39, 72]. According to Thewes [112] and Budach et al. [19], liquid foam is needed as a conditioning agent to achieve safe and economical EPB tunneling for coarse-grained soils. For this reason, workability and flowability should be known to describe the flow properties of the surface wetted soil (particle)-foam mixture. The term workability can be explained in various definitions, such as "a measure of how easy or difficult sample is to place [58]" and "the ability to perform satisfactorily in some transporting operation or forming process [110]". Flowability is defined as the flow of granular solids or powders [5].

The particle-foam mixture is rheologically complex (non-Newtonian) as defined in Özarmut et al. [88]. The slump test can be used to determine the flow behavior of complex fluid due to its simplicity. In order to measure slump of a sample, a truncated cone open at both ends is placed on a horizontal surface and is filled with the sample [31, 48]. After filling process, the cone is lifted vertically upwards. For a standard slump test, the final slump of a sample is related only to the yield stress [32, 33]. According to Ferraris [31], the existence of a yield stress causes the flow of sample. On the other hand, Ferraris et al. [32] assumed that the time dependence of slump is related to the viscosity for a modified slump test. A correlation between slump flow and viscosity was observed by Laskar [63]. The percentage increase in average diameter of the spread over the base diameter of the cone related to the viscosity was determined for slump flow [63].

As it is known, an ASTM [1] standard slump test is performed to measure workability and flowability of the material in macro-scale. Considering a micro-scale experiment of the material, a mini slump cone, which was produced approximately by one-seventh of the standard slump cone scaling, was used to measure the flow properties of the material experimentally. On the other hand, the flow properties can be determined numerically by using numerical approaches allowing to take into account free surface flow like the Smoothed Particle Hydrodynamics (SPH) method. In order to identify and to compare the rheological parameters of the surface wetted particle-foam mixtures, the modified Herschel-Bulkley-Papanastasiou equation [90] was implemented in SPH. Several researchers have previously applied the SPH method and investigated slump test experiments. SPH is a particle simulation method, which was parallel developed and invented by Lucy [69], Monaghan [83] and Gingold [42]. In 1994, Monaghan [84] applied the SPH method to free surface. The SPH technique is also applied to viscoelastic flow problems [30]. Additionally, some numerical simulations of the slump test have been carried out by Roussel et al. [99]. For the numerical simulations, they considered two classical conical geometries, the ASTM Abrams cone [1] and the ASTM minicone [2]. Roussel [98] and Schowalter and Christensen [103] worked on the slump test which has a relation with yield stress.

The flowability and workability of the surface wetted particle-foam mixture have not yet been investigated using Direct Numerical Simulations for comparisons with heteregenous experimental data of mini slump tests. In order to understand the flowability and workability of this suspension, both, experimental and numerical researches are needed. This investigation will help to understand the suspension rheologically very well and to solve some problems related with transportation in EPB tunnelling.

7.2   Smoothed Particle Hydrodynamics (SPH)

In Chapter 5, the modified Herschel-Bulkley-Papanastasiou rheology in 1D was used for pure foam and surface wetted particle-foam mixtures. The rheological properties of pure foam and it's mixtures (non-Newtonian fluids) were obtained by using rheometer with plate-plate geometry. In this chapter, the slump experiment was performed to describe the flow properties of non-Newtonian fluids. However, it is not always easy to interpret the experimental results without a numerical solution due to the lack of an analytical solution [124]. Thus, the lagrangian SPH method has been applied to the flow of the non-Newtonian fluids, and the numerical analysis was performed by Sivanesapillai et al. [105].

The advantage of SPH as a particle method is the Lagrangian character as well as its meshfree nature that allows the simulation of free surface flow without modeling the non-linear convective terms in the conservation laws.

Accordingly, it has gained increasing in modeling the flow of fluids. Zhu et al. [124] and Martys et al. [77] used a SPH approach to model non-Newtonian fluids. In order to validate this approach, the regularized Papanastasiou-Bingham model [90] was implemented into the SPH model. The regularisation method provides to avoid the singularity in viscosity in the limit of zero shear rate (unyielded region) [77]. Thus, the regularized model can be used for both yielded and unyielded regions [108].

The basic idea of SPH is the approximation of field quantities $f(\mathbf{x})$ and partial differential operators on the basis of the reproducing convolution-based kernel interpolation [68, 83, 107]

$$f(\mathbf{x}) \approx \int_{\Omega} f(\mathbf{x}') \, W(\mathbf{x} - \mathbf{x}', h) \, \mathrm{d}v, \tag{7.1}$$

where W is a non-negative continuously differentiable kernel function with compact support that is zero for $||\mathbf{x} - \mathbf{x}'|| > \kappa h$, with the smoothing length h and compactness factor κ. For simplicity, we chose h to be constant in space and time. $W(\mathbf{x} - \mathbf{x}', h)$ has to satisfy the Dirac delta property $\lim_{h \to 0} W(\mathbf{x} - \mathbf{x}', h) = \delta(\mathbf{x} - \mathbf{x}', h)$ with δ being the Dirac delta function. To provide zeroth and first order completeness, the completeness conditions $\int_{\Omega} W(\mathbf{x}, h) \mathrm{d}v = 1$ and $\int_{\Omega} \mathbf{x} W(\mathbf{x}, h) \mathrm{d}v = 0$ have to be fulfilled. The kernel function is used to be symmetric such that $W(\mathbf{x} - \mathbf{x}', h) = W(r, h)$ and $\mathrm{grad}\, W(\mathbf{x}, h) = (\mathbf{x}/r)[\frac{\partial W(r,h)}{\partial r}]$ with the radius $r = ||\mathbf{x} - \mathbf{x}'||$. The approximation gradients of field functions is done by

$$\mathrm{grad} f(\mathbf{x}) \approx \int_{\Omega} f(\mathbf{x}') \, \mathrm{grad}\, W(\mathbf{x} - \mathbf{x}', h) \, \mathrm{d}v, \tag{7.2}$$

where, as shown, the gradient operator is switched to the continuous differentiable kernel function.

We solve the numerical integration of the kernel interpolation by using quadrature rule over neighboring particles $j = 1...N$ forces. Therefore every arbitrary field function and its derivative is approximated by

$$f(\mathbf{x}) = \sum_{j} f_j \, W_{ij} \, V_j, \tag{7.3}$$

$$\mathrm{grad} f(\mathbf{x}) = \sum_{j} f_j \, \frac{\partial W_{ij}}{\partial \mathrm{r}_{ij}} \frac{\mathbf{x}_i - \mathbf{x}_j}{\mathrm{r}_{ij}} \, V_j. \tag{7.4}$$

7.3 SPH Discretization of Balance Equations

Early SPH algorithms, derived from probability theory, did not conserve linear and angular momentum [67]. Although these algorithms are suitable for many astrophysical problems, they have some challenges involving accuracy

and stability in the simulation of fluid mechanical problems. In order to solve these challenges, Gingold et al. [43] proposed a SPH algorithm that conserves both linear and angular momentum. The SPH algorithm was used to identify the criterion for instability in the tensile regime by Swegle et al. [107]. On the other hand, Bonet et al. [16] discussed the linear and angular momentum which preserves properties of a new corrected SPH algorithm. Thus, the discrete SPH algorithms propose exact mass and momentum conservation. The continuous balance equations are approximated partially by the occurring interacting particle forces with the presented scheme. The discrete form of the mass balance and the momentum balance equation therefore have the form

$$\dot{\rho} = \sum_j m_j \left(\mathbf{u}_i - \mathbf{u}_j\right) \cdot \operatorname{grad} W_{ij}, \tag{7.5}$$

$$m_i \dot{\mathbf{u}}_i = \sum_j \mathbf{F}_{ij}^V + \sum_j \mathbf{F}_{ij}^P + \mathbf{F}_i^G. \tag{7.6}$$

The local balance equation is transformed into a system of ordinary differential equations for the particle velocity $\mathbf{u}_i$. Therefore the total forces acting on each particle can be divided into gravitational forces $\mathbf{F}_i^G = m_i \mathbf{g}$ and particle interaction forces between particles i and j, represented by pressure interaction forces $\mathbf{F}_{ij}^P$ and viscous interaction forces $\mathbf{F}_{ij}^V$. Thus the discrete formulation of the interaction forces is

$$\mathbf{F}_{ij}^P = \left[\frac{1}{n_i} + \frac{1}{n_j}\right] \left(\frac{p_i \rho_i + p_j \rho_j}{\rho_i + \rho_j}\right) \frac{\partial W_{ij}}{\partial r_{ij}} \frac{\mathbf{x}_i - \mathbf{x}_j}{r_{ij}}, \tag{7.7}$$

$$\mathbf{F}_{ij}^V = \left[\frac{1}{n_i} + \frac{1}{n_j}\right] \frac{2\mu_i \mu_j}{\mu_i + \mu_j} \frac{\mathbf{u}_i - \mathbf{u}_j}{r_{ij}} \frac{\partial W_{ij}}{\partial r_{ij}}, \tag{7.8}$$

with the particle number density $n_i = \sum_j W_{ij}$ and $\mu_i = \mu_E$. The particle interaction forces act between particle i and each neighboring particle j included in the compact support κh of $W_{ij}(r_{ij}, h)$ with respect to the interpolation point $\mathbf{x}_i$.

7.4   Mini Slump Test

The flowability and workability of pure foam and it's mixtures have been tested by using the mini slump test. The same mixing process (Chapter 2) was used to prepare surface wetted particle-foam mixtures. The mixtures were taken $n_0^{(w+s)1} = 0.23$, $n_0^{(w+s)2} = 0.33$ and $n_0^{(w+s)3} = 0.5$ for surface wetted particles. In order to neglect the effect of the temperature on liquid foam, all experiments were carried out at room temperature. From the mini slump cone, the spread and slump of the pure foam and mixtures were measured to compare with

numerical simulations. In Roussel et al. [99], the slump and the spread were defined that the difference in height between the beginning of the test and after flow stops, and the last diameter of the collapse sample, respectively.
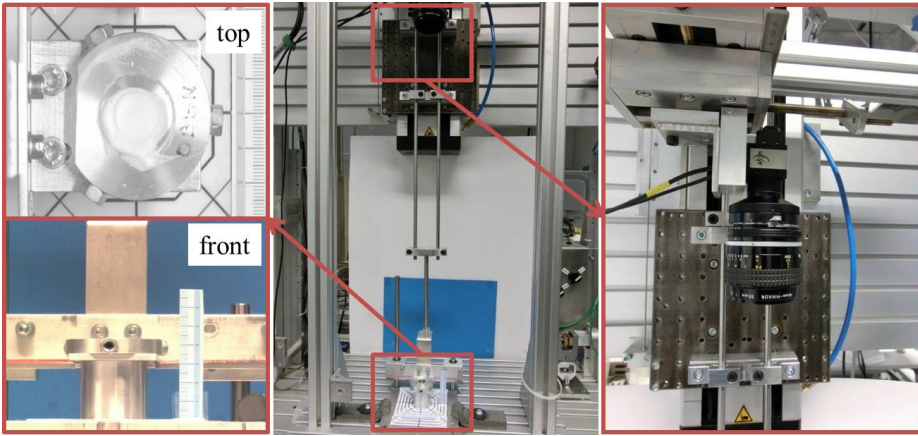
Figure 7.1: Cone setup (middle), front and top view of the cone (left) and camera (right)

As it is known, standard slump cone is lifted manually which cannot be controlled the lifting process precisely. Contrary to the lifting process of standard slump cone, the mini slump cone was lifted automatically. Cone setup was prepared to perform mini slump test. (Figure 7.1, middle). The movement of the cone was controlled by the Maxon DC motor with a digital positioning system (Epos 60W). By using software program, the speed of the movement was set 3 mm/s for all the experiments. The mini cone is stopped at 20 mm, meaning that lifting of the cone takes 6.6 s. An aluminium plate (DIN AlMgSi) with transparent paper was used to show the spread flow of the materials. To be more precise, many octagons with the same centerpoint were printed on the transparent paper (Figure 7.1). The slump test was synchronously recorded by two digital cameras. One is vertically orientated (Figure 7.1, right), while the second one is horizontally fixed in front of the cone setup. The horizontally fixed camera (DFK 31 BU03.H, The Imagingsource) used with the Nikon objectiv Nikkor AF (range: 35-70 mm, f/1:3.3-4.5) takes 15 photos per seconds. The vertically fixed camera (U-Eye UI 149xSE-C, IDS) with the Nikon Objectiv Micro-Nikkor (range: 55 mm, f/1:3.5) takes a photo in 1.5 s. The duration time of the slump test is approximately 1.20 min. According to a smaller version of standard slump cone (ASTM Abrams cone) [1], the mini slump cone is homemade and produced from aluminium (DIN AlCu4PbMgMn). As seen in Figure 7.2, the mini cone shape has dimensions that are approximately seven times smaller than the standard slump cone. The internal diameters of the mini slump cone are 28 mm at the base and 13.5 mm at the top. The height of the cone is 43.5 mm.

The mini cone was filled with foam and surface wetted particle-foam mixtures in two layers and each layer is compacted 4 times by a 15 mm rod. Before filling the sample, the inside of the cone moisturized with wet swab due to slip effect inside the cone. The moisturizing process leads to sticky surfaces (adhesion). Thus, the sticky surfaces prevent to slip inside the cone. For each sample, the mini slump test was performed three times to check repeatability. After filling process, the mini cone was lifted automatically. The slump and spread of the sample were recorded by cameras.
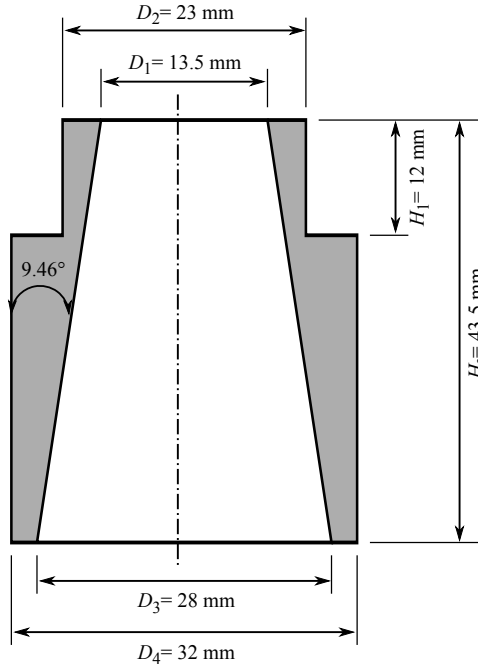
Figure 7.2: Mini cone geometry

7.5   Experimental and Numerical Results

7.5.1   Pure Foam and Surface Wetted Particle-Foam Mixture $\left(\mathbf{n_0^{(w+s)1}} = \mathbf{0.23}\right)$

The rheological experiments of pure foam and $n_0^{(w+s)1} = 0.23$ surface wetted particle-foam mixture were performed and matched with the Herschel-Bulkley-Papanastasiou model [88]. In order to investigate the rheology, the mini slump test can be used. In this test, the geometrical quantities, slump (the last height of the testing material) and spread (the last diameter of the testing material) are measured to get flowability of the testing material. Generally, the relation between slump or spread and yield stress of the material is considered for

the slump test. Coussot et al. [22] showed that the spread is more apposite to obtain the yield stress of the testing material. The relation between the spread and yield stress was also investigated by Domone [24]. The slump experiment was not performed to show the connection between the slump or spread and the yield stress of the material in this study. However, in order to obtain flowability and to compare the experimental and numerical results, the slump test was performed not only for pure foam but also for surface wetted particle-foam mixtures with $n_0^{(w+s)1} = 0.23$, $n_0^{(w+s)2} = 0.33$ and $n_0^{(w+s)3} = 0.5$.
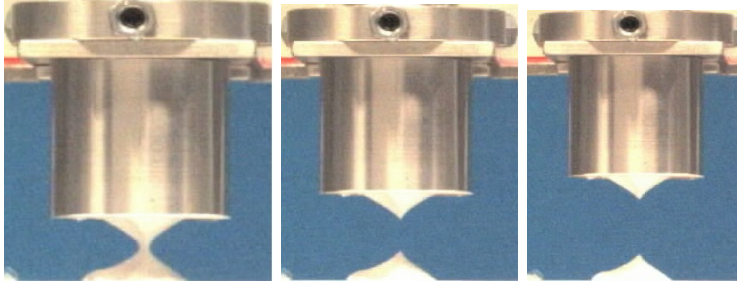
Figure 7.3: Slump test front view of the pure foam for $t_1 = 3$ s (left), $t_2 = 6$ s (middle) and $t_3 = 11$ s (right).

As seen in Figure 7.3 and Figure 7.4, the testing material (pure foam and $n_0^{(w+s)1} = 0.23$ surface wetted particle foam mixture) were filled in the mini cone. In Figure 7.3 and Figure 7.4, three pictures were taken at different times; $t_1 = 3$ s, $t_2 = 6$ s and $t_3 = 11$ s. For both figures, the slump tests cannot be conducted to show the slump and the spread of the pure foam and $n_0^{(w+s)1} = 0.23$ surface wetted particle-foam mixture due to high resistance to flow. A significant amount of the pure foam sticks to the mini cone, whereas the rest remains on the bottom plate (Figure 7.3). According to Tyrode et al. [114], the surfactants of liquid foam (Chapter 4) leads to very high foam stability at room temperature and foam flows after several hours. Thus, the mini slump test shows that pure foam cannot flow easily at room temperature because of the high stability of pure foam. On the other hand, it is clear that the measurement of slump and spread is not possible for pure foam.

The surface wetted particle-foam mixture shows the same treatment as pure foam (Figure 7.4). The volume percentage of the surface wetted particle $(n_0^{(w+s)1} = 0.23)$ is not enough to flow through the mini cone in $t_3 = 11$ s. Contrary to pure foam, the part of the surface wetted particle-foam mixture remains on the cone flows after $t_4 = 21$ s. The result of the mini slump test can also be related to the result of flow curve test in Chapter 5. As it is shown in Chapter 5, the shear stress or viscosity of pure foam is greater than that of the surface wetted particle-foam mixtures. The flow resistance (viscosity) of pure foam and surface wetted particle-foam mixture can be observed qualitatively
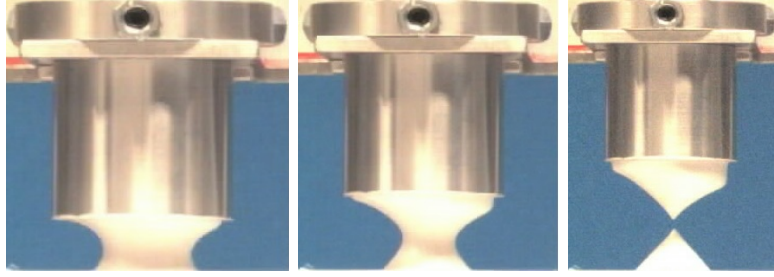
Figure 7.4: Slump test front view of $n_0^{(w+s)1} = 0.23$ surface wetted particle-foam mixture for $t_1 = 3$ s (left), $t_2 = 6$ s (middle) and $t_3 = 11$ s (right).

if the results in $t_4 = 21$ s are compared for mini slump test (Figure 7.5). The mini slump test shows that the viscosity of pure foam greater than the viscosity of surface wetted particle-foam mixture.
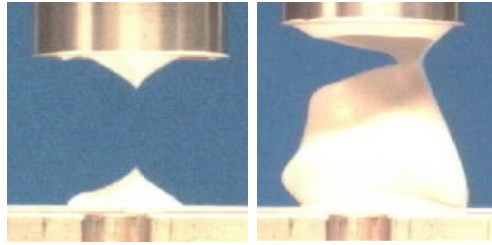
Figure 7.5: Slump test front view of pure foam (left) and $n_0^{(w+s)1} = 0.23$ surface wetted particle-foam mixture (right) for $t_4 = 21$ s.

Although flowing of the remaining part, slump and spread cannot be measured for $n_0^{(w+s)1} = 0.23$ surface wetted particle-foam mixture due to an incorrect result. The mini slump test gives an incorrect result even if repeated three times. Considering the slump test of the pure foam and $n_0^{(w+s)1} = 0.23$ surface wetted particle-foam mixture, the experimental results are not comparable and suitable to measure the slump and spread. Thus, the numerical simulation (SPH) was not carried out for both pure foam and $n_0^{(w+s)1} = 0.23$ surface wetted particle-foam mixtures.

7.5.2 Surface Wetted Particle-Foam Mixture ($n_0^{(w+s)2} = 0.33$)

The mini slump was also tested for higher amount volume of surface wetted particle. In order to observe the slump test of the mixture, the liquid foam with the volume $n_0^{f2} = 0.67$ was mixed with $n_0^{(w+s)2} = 0.33$ surface wetted particle. Due to the high volume of the surface wetted particle, the slump test was

accomplished. When the mini cone is lifted automatically, the mixture flows and the slump and the spread can be measured at different time. As it is known from standard slump test, spread and slump cannot be measured during the lifting process. For a slump test, the measurement of the spread and the slump should be taken after lifting process [31, 48]. Therefore, the time at which the foam separates from the cone is taken as the initial time $t_0 = 0$ s (Figure 7.6, left). The initial height and the initial base diameter of the mixture are 24 mm and 34.5 mm, respectively.
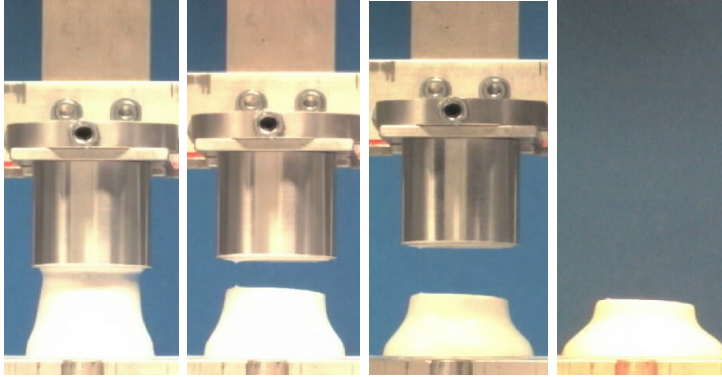

Figure 7.6: Slump test front view of $n_0^{(w+s)2} = 0.33$ surface wetted particle-foam mixture at $t_0 = 0$ s (left), at $t_1 = 1$ s (middle, left), at $t_2 = 3$ s (middle, right) and at $t_3 = 50$ s (right).

Four pictures, which were taken at $t_0 = 0$ s, $t_1 = 1$ s, $t_2 = 3$ s and $t_3 = 50$ s, can be seen in Figure 7.6. Generally, the duration of the mini slump test was set at $t_{final} = 1.10$ min to measure the final slump and spread of the mixture.
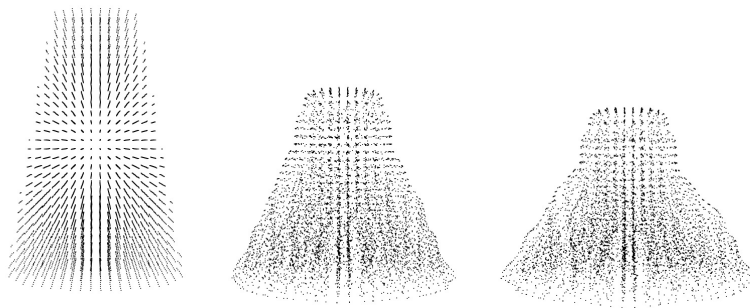
Figure 7.7: SPH simulation with the slip parameter (S=0.99) for $n_0^{(w+s)2} = 0.33$ surface wetted particle-foam mixture at $t_0 = 0$ s (left), at $t_1 = 1$ s (middle) and at $t_3 = 2.5$ s (right).

The final slump and spread of the mini cone test were not compared with the final slump and spread of SPH due to the long simulation time. This high simulation time arises because of small timesteps and a high number of neighboring particles in 3-dimensional simulations. In Figure 7.7, the results of SPH were taken at $t_0 = 0$ s , $t_1 = 1$ s and $t_2 = 2.5$ s. For the initial boundary condition ($t_0 = 0$ s), dimensions of the mini cone were set as initial values in the numerical simulation. The slump of SPH shows that the mixture flows very rapidly at the beginning, after a short time. As it is seen in Figure 7.8, the results of SPH (Figure 7.7) were taken to compare with the experimental data (Figure 7.6).
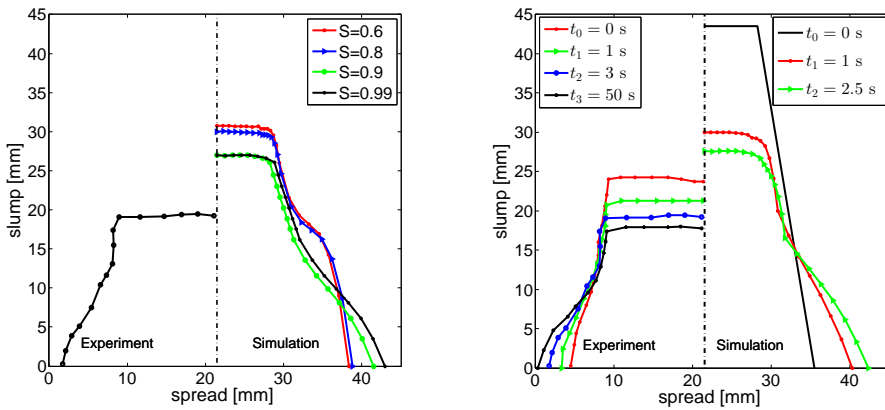
Figure 7.8: Comparison of the slump and the spread between experiment and simulation with different slip parameter S at $t_{exp} = 3$ s and $t_{sim} = 2.5$ s (left), and with S=0.99 at various time (right).

The spread of experiment at $t_{exp} = 3$ s and the spread of numerical simulations at $t_{sim} = 2.5$ s were compared for the slip parameter S (Figure 7.8, left). However, the slump of the experiment is difficult to compare with the slump of the simulation due to high difference in the initial height values of experiment and simulation. In order to show the effect of the slip on the flowability of the mixture, different slip parameters (S=0.6, 0.8, 0.9 and 0.99) were used in SPH method. The slip parameter affects on the spread of the mixture. When the total slip is taken into account, the spread has the highest value. It is also clear that the mini slump experiment has been performed by considering total slip due to transparent paper on the metal plate. Thus, the experiment and numerical simulation with S=0.99 gave the same spread. On the other hand, the slump and spread of the mixture are identical for different small slip parameters (S= 0.6 and S=0.8). At various time, the slump and the spread with

the same slip parameter (S=0.99) can be seen in Figure 7.8. The slump and the spread between t_1 and t_2 have approximately the same value for experiment and simulation that the proportional flow of the mixture is identical.
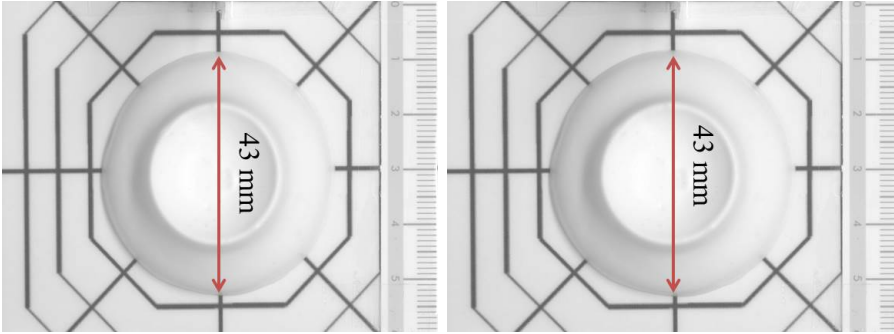
Figure 7.9: Top view (spread) of mini slump test of $n_0^{(w+s)2} = 0.33$ at $t_3 = 50$ s (left) and at $t_{final} = 1.10$ min (right).

The same spread value was measured 43 mm at $t_3 = 50$ s and $t_{final} = 1.10$ min (Figure 7.9). The experimental result shows that the flow of mixture stops after $t_3 = 50$ s and the final stage can be taken at $t_3 = 50$ s.

7.5.3 Surface Wetted Particle-Foam Mixture ($n_0^{(w+s)3} = 0.5$)
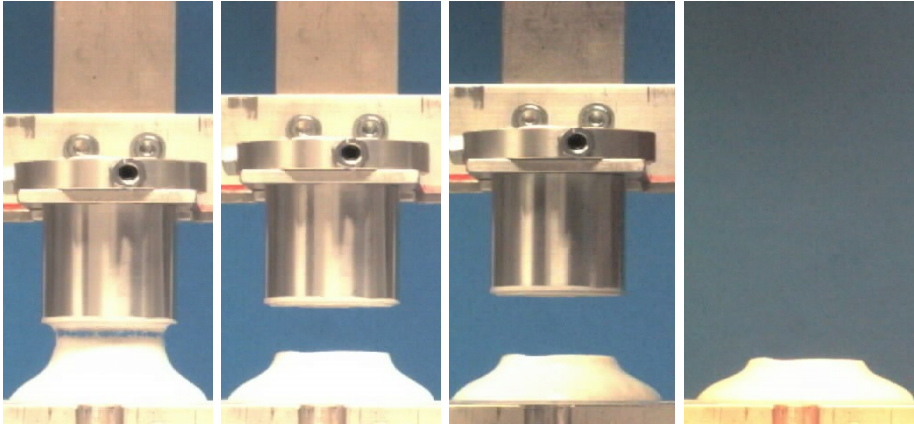
Figure 7.10: Slump test front view of $n_0^{(w+s)3} = 0.5$ surface wetted particle-foam mixture at $t_0 = 0$ s (left), at $t_1 = 1$ s (middle, left), at $t_2 = 3$ s (middle, right) and at $t_3 = 50$ s (right).

The slump experiment has also been performed for $n_0^{(w+s)3} = 0.5$ surface wetted particle-foam mixture. The same procedure used for $n_0^{(w+s)2} = 0.33$

was applied to this mixture. In order to show how the volume of surface wetted particle affects flowability or workability of the mixture, the volume of the surface wetted particle was increased, while the volume of foam was taken constant. The front view of the slump test, shown in Figure 7.10, was taken at various time $t_0 = 0$ s, $t_1 = 1$ s, $t_2 = 3$ s and $t_3 = 50$ s. It can be clearly seen that $n_0^{(w+s)3} = 0.5$ surface wetted particle-foam mixture flows rapidly in a short time.
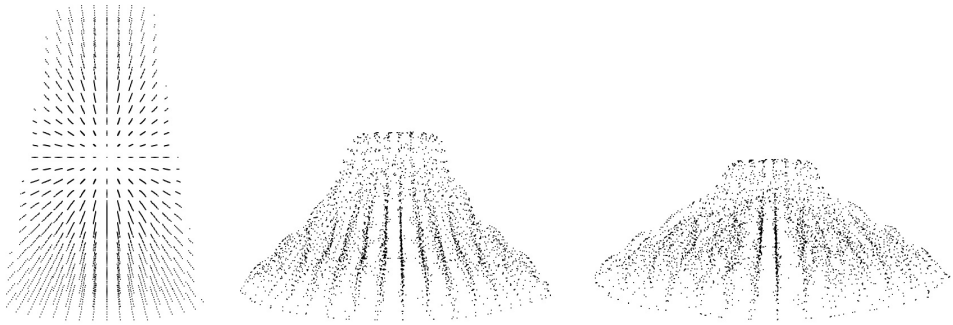
Figure 7.11: SPH simulation with the slip parameter (S=0.99) for $n_0^{(w+s)3} = 0.5$ surface wetted particle-foam mixture at $t_0 = 0$ s (left), at $t_1 = 1$ s (middle) and at $t_2 = 3$ s (right).

The numerical simulation of slump test at various time $t_0 = 0$ s, $t_1 = 1$ s and $t_2 = 3$ s were shown to compare with the experimental results (Figure 7.11). For the initial boundary condition ($t_0 = 0$ s), diameter and height of the mini cone were also set as initial values. At various times, the result of experiments and simulations show that the spread is similar for the mixture. On the other hand, the slip effect should also be considered to analyse how it affects the results for the slump test for $n_0^{(w+s)3} = 0.5$ surface wetted particle foam mixture. Experimentally, showing the influence of the slip is difficult. However, it can be shown by using the SPH method by using various slip parameter, such as S=0.6, S=0.8, S=0.9 and S=0.99 (Figure 7.12, left). We compare the experimental result, which are on the left of the dashed line and the numerical results on the right of the dashed line. The results (spread and slump) of experiment and numerical simulation were taken at $t_{exp} = t_{sim} = 3$ s. If the spread is considered, the simulation with the slip parameters S=0.6, S=0.8 and, S=0.9 yields nearly same results. The spread of the experiment gives the same result as the spread of the numerical simulation with the slip parameter S=0.99. As has been discussed previously, the same slip effect in the results of $n_0^{(w+s)2} = 0.33$ surface wetted particle-foam mixture can be seen for $n_0^{(w+s)3} = 0.5$ surface wetted particle-foam mixture. Therefore, the numerical simulations were carried out with the total slip (S=0.99) at $t_1 = 1$ s and $t_2 = 3$ s (Figure 7.12, right). As seen in Figure 7.12, spreads of experiment are equal

to spreads of numerical simulation. However, slump of experiment is difficult to compare with slump of numerical simulation.
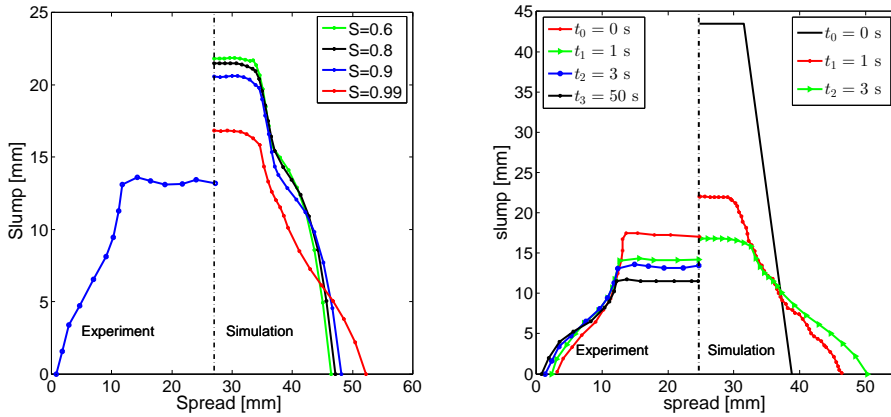
Figure 7.12: Comparison of the slump and the spread between experiment and simulation with different slip parameter S at $t_{exp} = t_{sim} = 3$ s (left), and with S=0.99 at various time (right).

The spread of mixture was measured 53 mm for both $t_3 = 50$ s and $t_{final} = 1.15$ min (Figure 7.13). In order to compare flow of the mixture ($n_0^{(w+s)3} = 0.5$) with the mixture ($n_0^{(w+s)2} = 0.33$), the total slump test was measured approximately at the same time $t_{final} = 1.15$ min.
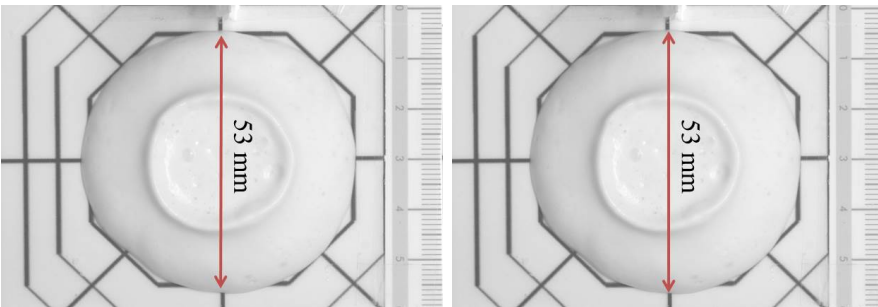
Figure 7.13: Top view (spread) of mini slump test of $n_0^{(w+s)3} = 0.5$ at $t_3 = 50$ s (left) and at $t_{final} = 1.15$ min (right)

The spread of this mixture is larger than the spread of $n_0^{(w+s)2} = 0.33$ surface wetted particle-foam mixture. The reason for this is the large volume of water. $n_0^{(w+s)3} = 0.5$ surface wetted particle-foam mixture consists of a large

volume of water and it is very well known that the viscosity of a water is very low, which increases the flowability of the mixture. Thus, when the flowability increases, the flow of the spread increases.

7.6   Conclusion

In this Chapter, the rheological properties (flowability and workability) of the non-Newtonian material (surface wetted particle foam mixture) were researched with the comparison of experimental (mini slump test) and numerical simulation (SPH method). The influence of increasing the volume of surface wetted particle on the suspension (mixture) was shown with experimental results. Numerical simulations were used to predict experimental results and to clarify the range of validity of the constitutive model in 3D. Especially, numerical simulations are very important to show how the slip effect can affect on the spread and slump of the mixture, which is not possible to show with the mini slump test.

The mini slump test can be used for high volume percentage of surface wetted particle-foam mixtures ($n_0^{(w+s)2} = 0.33$ and $n_0^{(w+s)3} = 0.5$). The experimental results show that pure foam cannot flow easily at room temperature after several minutes. The high stability of pure foam prevents to flow easily. Thus, the mini slump test cannot be performed for pure foam. On the other hand, the measurement of slump and spread are also not possible for $n_0^{(w+s)1} = 0.23$ surface wetted particle-foam mixture due to small volume of surface wetted particle. If we compare flowability of pure foam and $n_0^{(w+s)1} = 0.23$ surface wetted particle-foam mixture, it is clear that the mixture flows after several seconds while pure foam cannot flow after several minutes. Considering the flow of both materials, viscosity of pure foam is higher than $n_0^{(w+s)1} = 0.23$ surface wetted particle-foam mixture. For the high volume percentage of surface wetted particle-foam mixtures ($n_0^{(w+s)2} = 0.33$ and $n_0^{(w+s)3} = 0.5$), spread and slump were measured at various times by using mini slump test. The spread was used to compare the experimental and numerical results. When the total slip is taken into account, the spread values for both numerical simulation and experiment are consistent with each other. The consistency of the numerical and experimental results shows that slip effects should be taken into account for surface wetted particle-foam mixtures.

Chapter 8

Conclusion

The main objective of this research was to investigate the rheological proper-
ties of soil conditioning with the appropriate constitutive model on micro-scale
for the face stability of the EPB shield machine. The general introduction
elucidated the rheological experiments of the soil conditioning and the consti-
tutive model. For the rheological experiments, the slip effect, the mini slump
test and SPH method were also addressed in the general introduction.

Chapter 2 was focused on the working process of the EPB shield machine
and soil conditioning in mechanized tunnelling. Foam is the most suitable
conditioning agent, when the properties of foam is evaluated with various tests.
Especially, the rheological properties and workability of foam have an influence
on the soil conditioning which can change the perfoemance of the EPB shield
machine, thereby this phenomenon changes the cost of working process.

Chapter 3 was focused on the theoretical background of fluid flow. The
three laws of mechanics, constitutive and Navier-Stokes equations were pre-
sented to use for the fluid flow between plate-plate and cone-plate.

In Chapter 4, the rheological experiments and the working process of the
modern rheometer were explained to use the appropriate tools (geometry type)
for foam and particle foam mixtures. The general information about rheology
and rheometer with various types help to analyse rheological experiments of
materials and to classify the type of materials. A relationship between the
constitutive model and the flow of plate-plate and/or cone-plate geometry was
obtained to understand the derivation of the model analytically. Additionally,
the constitutive model was derived to use for numerical simulation in Chapter
7. In order to analyse the flow between plate-plate, cone-plate and cup &
bob geometries, the Navier-Stokes equations and rate of deformation tensors
were used in cylindrical and spherical coordinates. Due to influence of the wall
slip on the rheological experiments, the model was also derived for plate-plate
geometry at the special boundary conditions (with and without slip effect).

The rheological properties and the microstructure of foam and particle

foam mixtures were investigated in Chapter 5. As it is explained in Chapter 2, the parameter of foam (FIR), which are defined by volume of foam to volume of soil, is important for mechanized tunnelling. Thus, foam was mixed with various volume fraction of the dry particle and the rheological experiments were performed for the mixtures up to 0.3 volume fraction of particles due to noisy data occuring for higher values. When the volume fraction of particles is taken higher than 0.3, the mixture behaves like solid that means many small particles connect with each other and this phenomenon causes jamming of the particles. Due to jamming of the particles, the rheological experiments give noisy data (negative results) for viscosity or shear stress. For a high volume fraction of particle, foam was mixed with the surface wetted particle (up to 0.64 volume fraction of particle). It is also known that, water can be used as an additional conditioning agent in mechanized tunnelling and thereby the rheological investigation of the water can help to analyse effect of it on the soil conditioning. To obtain the rheological parameters, such as yield stress, fluid consistency, and exponent, the constitutive rheological model (the modified Herschel-Bulkley-Papanastasiou model) was developed to use for dry and surface wetted particle foam mixtures. The linear and non-linear viscoelastic regimes of the mixtures were verified and a relation between complex modulus and volume fraction of dry and surface wetted particle mixtures was obtained.

The slip effect, which is a challange for rheological experiments, was addressed in Chapter 6. It causes to get inaccurate results, when fluid flows at the solid boundaries. Thus, the non-Newtonian fluid between plate plate geometry was considered with slip effect by using the Jasterzebski & Oldroyd model, and the slip velocity of liquid foam and particle-foam mixtures were determined to get the actual shear rate and shear stress. Moreover, the shear stress was obtained by visualization method to compare with the actual shear stress. On the other hand, the sandpaper P320 was a good choice to minimize the slip effect on the plate plate geometry. The experimental result obtained by plate plate with sandpaper was verified by the numerical simulation (SPH method).

In Chapter 7, the SPH method and mini slump test were presented for non-Newtonian fluid flow. The flowability and workability of the non-Newtonian fluid were considered by mini slump test. The experimental results were also verified by SPH method and the slip effect was taken into account for the numerical simulation.

In conclusion, the rheological behavior of the foam and particle-foam mixtures were described by the modification of Herschel-Bulkley-Papanastasiou model in continuum mechanics. Thus, it helps to understand the flow behaviour of the foam and particle-foam mixture. All of the rheological experiments and their results in Chapter 5 and Chapter 7 are serves as a bridge between micro- and macro-scale in EPB shield machine.

Appendix

Appendix A

Navier Stokes Equations

An arbitrary velocity vector in cartesian coordinate system is

$$\mathbf{u} = u_x\mathbf{e}_x + u_y\mathbf{e}_y + u_z\mathbf{e}_z. \tag{A.1}$$

The equations of motion with three components in cartesian coordinates:

$$\rho\left(\frac{\partial u_x}{\partial t} + u_x\frac{\partial u_x}{\partial x} + u_y\frac{\partial u_x}{\partial y} + u_z\frac{\partial u_x}{\partial z}\right) = -\frac{\partial p}{\partial x} + \left(\frac{\partial \tau_{xx}}{\partial x} + \frac{\partial \tau_{xy}}{\partial y} + \frac{\partial \tau_{zx}}{\partial z}\right) + \rho g,$$

$$\rho\left(\frac{\partial u_y}{\partial t} + u_x\frac{\partial u_y}{\partial x} + u_y\frac{\partial u_y}{\partial y} + u_z\frac{\partial u_y}{\partial z}\right) = -\frac{\partial p}{\partial y} + \left(\frac{\partial \tau_{xy}}{\partial x} + \frac{\partial \tau_{yy}}{\partial y} + \frac{\partial \tau_{zy}}{\partial z}\right) + \rho g,$$

$$\rho\left(\frac{\partial u_z}{\partial t} + u_x\frac{\partial u_z}{\partial x} + u_y\frac{\partial u_z}{\partial y} + u_z\frac{\partial u_z}{\partial z}\right) = -\frac{\partial p}{\partial z} + \left(\frac{\partial \tau_{xz}}{\partial x} + \frac{\partial \tau_{yz}}{\partial y} + \frac{\partial \tau_{zz}}{\partial z}\right) + \rho g.$$

An arbitrary velocity vector in cylindrical coordinate system is

$$\mathbf{u} = u_r\mathbf{e}_r + u_\Phi\mathbf{e}_\Phi + u_z\mathbf{e}_z. \tag{A.2}$$

The equations of motion with three components in cylindrical coordinates:

$$\rho\left(\frac{\partial u_r}{\partial t} + u_r\frac{\partial u_r}{\partial r} + \frac{u_\Phi}{r}\frac{\partial u_r}{\partial \Phi} - \frac{u_\Phi^2}{r} + u_z\frac{\partial u_r}{\partial z}\right) =$$
$$-\frac{\partial p}{\partial r} + \left(\frac{1}{r}\frac{\partial(r\tau_{rr})}{\partial r} + \frac{1}{r}\frac{\partial \tau_{\Phi r}}{\partial \Phi} - \frac{\partial \tau_{\Phi\Phi}}{r} + \frac{\partial \tau_{zr}}{\partial z}\right) + \rho g,$$

$$\rho \left(\frac{\partial u_\Phi}{\partial t} + u_r \frac{\partial u_\Phi}{\partial r} + \frac{u_\Phi}{r} \frac{\partial u_\Phi}{\partial \Phi} + \frac{u_r u_\Phi}{r} + u_z \frac{\partial u_\Phi}{\partial z} \right) =$$

$$-\frac{1}{r} \frac{\partial p}{\partial \Phi} + \left(\frac{1}{r^2} \frac{\partial (r^2 \tau_{r\Phi})}{\partial r} \right) + \frac{1}{r} \frac{\partial \tau_{\Phi\Phi}}{\partial \Phi} + \frac{\partial \tau_{z\Phi}}{\partial z} + \frac{\tau_{\Phi r} - \tau_{r\Phi}}{r} \right) + \rho g,$$

$$\rho \left(\frac{\partial u_z}{\partial t} + u_r \frac{\partial u_z}{\partial r} + \frac{u_\Phi}{r} \frac{\partial u_z}{\partial \Phi} + u_z \frac{\partial u_z}{\partial z} \right) =$$

$$-\frac{\partial p}{\partial z} + \left(\frac{1}{r} \frac{\partial r \tau_{rz}}{\partial r} + \frac{1}{r} \frac{\partial \tau_{\Phi z}}{\partial \Phi} + \frac{\partial \tau_{zz}}{\partial z} \right) + \rho g.$$

An arbitrary velocity vector in spherical coordinate system is

$$\mathbf{u} = u_r \mathbf{e}_r + u_\varphi \mathbf{e}_\varphi + u_\theta \mathbf{e}_\theta. \tag{A.3}$$

The equations of motion with three components in spherical coordinates:

$$\rho \left(\frac{\partial u_r}{\partial t} + u_r \frac{\partial u_r}{\partial r} + \frac{u_\theta}{r} \frac{\partial u_r}{\partial \theta} + \frac{u_\varphi}{r \sin \theta} \frac{\partial u_r}{\partial \varphi} - \frac{u_\theta^2 + u_\varphi^2}{r} \right) + \frac{\partial p}{\partial r} =$$

$$\left(\frac{1}{r^2} (\frac{\partial (r^2 \tau_{rr})}{\partial r}) + \frac{1}{r \sin \theta} \frac{\partial \tau_{\theta r} \sin \theta}{\partial \theta} + \frac{1}{r \sin \theta} \frac{\partial \tau_{r\varphi}}{\partial \varphi} - \frac{\tau_{\theta\theta} + \tau_{\varphi\varphi}}{r} \right) + \rho g,$$

$$\rho \left(\frac{\partial u_\varphi}{\partial t} + u_r \frac{\partial u_\varphi}{\partial r} + \frac{u_\theta}{r} \frac{\partial u_\varphi}{\partial \theta} + \frac{u_\varphi}{r \sin \theta} \frac{\partial u_\varphi}{\partial \varphi} + \frac{u_r u_\theta}{r} + \frac{u_\theta u_\varphi \cot \theta}{r} \right) + \frac{1}{r \sin \theta} \frac{\partial p}{\partial \varphi} =$$

$$\left(\frac{1}{r^2} \frac{\partial (r^2 \tau_{r\varphi})}{\partial r} + \frac{1}{r} \frac{\partial \tau_{\theta\varphi}}{\partial \theta} + \frac{1}{r \sin \theta} \frac{\partial \tau_{\varphi\varphi}}{\partial \varphi} + \frac{\tau_{r\varphi}}{r} + \frac{2 \cot \theta \tau_{\theta\varphi}}{r} \right) + \rho g,$$

$$\rho \left(\frac{\partial u_\theta}{\partial t} + u_r \frac{\partial u_\theta}{\partial r} + \frac{u_\theta}{r} \frac{\partial u_\theta}{\partial \theta} + \frac{u_r u_\theta}{r} - \frac{u_\varphi^2 \cot \theta}{r} \right) + \frac{1}{r} \frac{\partial p}{\partial \theta} =$$

$$\left(\frac{1}{r^2} \frac{\partial (r^2 \tau_{r\theta})}{\partial r} \right) + \frac{1}{r \sin \theta} \frac{\partial (\tau_{\theta\theta} \sin \theta)}{\partial \theta} + \frac{1}{r \sin \theta} \frac{\partial \tau_{\theta\varphi}}{\partial \varphi} + \frac{\tau_{\theta r}}{r} - \frac{\cot \theta}{r} \tau_{\varphi\varphi} \right) + \rho g.$$

Appendix B

The Derivation of Stress Tensor for Cone-Plate Geometry

The derivation of the modified Herschel-Bulkley-Papanastasiou model at small angle is

$$\ln \tau_{\theta\varphi} = \ln\left(K\sqrt{\dot{\gamma}}\right) + \ln\left(\tau^*(1 - \exp(-a\,\dot{\gamma}))\right),$$

$$\ln \tau_{\theta\varphi} = \ln\left(K\right) + \ln(\dot{\gamma}^{\frac{1}{2}}) + \ln\left(\tau^*\right) - \ln\left(\tau^*\exp(-a\dot{\gamma})\right),$$

$$\ln \tau_{\theta\varphi} = \ln\left(K\right) + \ln(\dot{\gamma}^{\frac{1}{2}}) + \ln\left(\tau^*\right) - \ln\left(\tau^*\right) - \ln\left(\exp(-a\dot{\gamma})\right),$$

$$\ln \tau_{\theta\varphi} = \ln\left(K\right) + \ln(\dot{\gamma}^{\frac{1}{2}}) + \underbrace{\ln\left(\tau^*\right) - \ln\left(\tau^*\right)}_{=0} - \ln\left(\exp(-a\dot{\gamma})\right),$$

$$\ln \tau_{\theta\varphi} = \ln\left(K\right) + \ln(\dot{\gamma}^{\frac{1}{2}}) - (-a\dot{\gamma}),$$

$$\ln \tau_{\theta\varphi} = \ln\left(K\right) + \ln(\dot{\gamma}^{\frac{1}{2}}) + a\dot{\gamma},$$

$$\exp(\ln \tau_{\theta\varphi}) = \exp(\ln\left(K\right) + \ln(\dot{\gamma}^{\frac{1}{2}}) + a\dot{\gamma}),$$

$$\tau_{\theta\varphi} = \exp(\ln{(K)}) \exp(\ln(\dot{\gamma}^{\frac{1}{2}})) \exp(a\dot{\gamma}),$$

$$\tau_{\theta\varphi} = K\,\dot{\gamma}^{\frac{1}{2}}\,\exp(a\dot{\gamma}).$$

Bibliography

[1] *ASTM Designation C-143-90 Standard test method for slump of hydraulic cement concrete.* Annual Book of ASTM Standards, 04.01, Am. Soc. Test. Mat., Easton, MD, 1996.

[2] *ASTM Designation C230/C230M-03 Standard Specification for Flow Table for Use in Tests of Hydraulic Cement.* Annual Book of ASTM Standards, 04.01, Am. Soc. Test. Mat., Easton, MD, 2004.

[3] Prüfung von Frischbeton - Teil 2: Setzmaß. Hg. v. DIN Deutsches Institut für Normungen e. V. Beuth Verlag GmbH, Berlin, 2008.

[4] Prüfung von Frischbeton - Teil 8: Selbstverdichtender Beton Hg. v. DIN Deutsches Institut für Normungen e. V. Beuth Verlag GmbH, Berlin, 2009.

[5] E. C. Abdullah, A. M. Salam, and A. R. Aziz. Cohesiveness and flowability properties of silica gel powder. *Physics International*, 1(1):16–21, 2010.

[6] A. Ahuja and A. Singh. Slip velocity of concentrated suspension in couette flow. *Journal of Rheology*, 53:1461–1485, 2009.

[7] L. H. Babendererde. Developments in polymer application for soil conditioning in EPB-TBMs. In *Conference Proceedings: Tunnels and Metropolises*, pages 691–695. Balkema, 1998.

[8] T. Babendererde, W. Hensel, and B. Sharma. Additives to master major permeabilities for EPB and slurry TBMs. In *Tunnel*, page 35. Bauverlag, 2011.

[9] G. Baki and K. S. Alexander. *Introduction to Cosmetic Formulation and Technology.* John Wiley & Sons, 2015.

[10] I. Baki. *Process Understanding: For Scale-Up and Manufacture of Actice Ingredients.* Wiley-VCH, 2011.

[11] H. A. Barnes and D. Bell. Controlled-stress rotational rheometry - A historical review. *Korea-Australia Rheology Journal*, 15:187–196, 2003.

[12] H. A. Barnes, J. F. Hutton, and K. Watters. *An Introduction to Rheology.* Elsevier Science Publishers, 1st Edition, 1989.

[13] V. Bertola, F. Bertrand, H. Tabuteau, D. Bonn, and P. Coussot. Wall slip and yielding in pasty materials. *The Society of Rheology*, 47:1211–1226, 2003.

[14] A. Bezuijen. The influence of soil permeability on the properties of a foam mixture in a TBM. In *Tunnelling. A decade of progress. GeoDelft 1995-2005*, pages 36–41. Taylor & Francis, 2005.

[15] E. C. Bingham. The history of the society of rheology from 1924-1944. *The Society of Rheology*, 1944.

[16] J. Bonet and T. S. L. Lok. Variational and momentum preservation aspects of smooth particle hydrodynamics formulations. *Computer Methods in Applied Mechanics and Engineering*, 180:97–115, 1999.

[17] R. Brummer. *Rheology Essentials of Cosmetics and Food Emulsions.* Springer, 2006.

[18] C. Budach. *Untersuchungen zum erweiterten Einsatz von Erd-druckschilden in grobkörnigem Lockergestein.* PhD thesis, Ruhr-Universität Bochum, Bochum, 2012.

[19] C. Budach and M. Thewes. Erweiterte Einsatzbereiche von EPB-Schilden. *Geotechnik*, 36(2):96–103, 2013.

[20] S. C. Chu. *Effect of silica particles on foam stability.* PhD thesis, The University of Birmingham, Birmingham, 2012.

[21] S. Cohen-Addad, M. Krzan, R. Höhler, and B. Herzhaft. Rigidity percolation in particle laden foams. *Physical Review Letters*, 99(16), 2007.

[22] P. Coussot, S. Proust, and C. Ancey. Rheological interpretation of deposits of yield stress fluids. *Journal of Non-Newtonian Fluid Mechanics*, 66:55–70, 1996.

[23] T. Dang-Vu and J. Hupka. Characterization of porous materials by capillary rise method. *Physicochemical Problems of Mineral*, 39:47–65, 2005.

[24] P. Domone. The slump flow test for high-workability concrete. *Cement and Concrete Research*, 28:177–182, 1998.

[25] Z. Du, B. S. Murray, R. Ettelaie, E. Dickinson, M. Bos, and T. van Vilet. Disproportionation in systems of protein-stabilized gas bubbles. In *3th International sympossium on food rheology and structure*, pages 401–406. Kerschensteiner Verlag, 2003.

[26] D. J. Durian. Foam mechanics at the bubble scale. *Physical Review Letters*, 75(26):4780–4783, 1995.

[27] D. J. Durian and A. J. Liu. *Jamming in colloiadal dispersions: hard-sphere suspensions, emulsions and foams*. Taylor & Francis, 2001.

[28] EFNARC. Specification and guidelines for the use of specialist products for mechanized tunneling (TBM). In *Soft Ground and Hard Rock Tunnelling*. The European Federation of Producers and Contractors of Specialist Products for Structures, 2005.

[29] C. Enzendorfer, R. Harris, P. Valko, M. Economides, P. Fokker, and D. Davies. Pipe viscometry of foams. *Journal of Rheology*, 39(2):345–358, 1995.

[30] J. Fang, R. G. Owens, L. Tacher, and A. Parriaux. A numerical study of the sph method for simulating transient viscoelastic free surface flows. *Non-Newtonian Fluid Mechanics*, 139:68–84, 2006.

[31] C. F. Ferraris. Measurement of the rheological properties of high performance concrete: State of the art report. *Journal of Research of the National Institute of Standards and Technology*, 104(5):461–478, 1999.

[32] C. F. Ferraris and F. de Larrard. Modified slump test to measure rheological parameters of fresh concrete. *Cement, Concrete and Aggregates*, 20(2):241–247, 1998.

[33] C. F. Ferraris and F. de Larrard. Testing and modelling of fresh concrete rheology. In *National Institute of Standards and Technology Interagency Report (NISTIR) 6094*. National Institute of Standards and Technology, Gaithersburg, Maryland, 1998.

[34] J. D. C. Figueroa, Z. J. E. Hernandez, P. R. Duarte, and R. J. Pena. Stress relaxation and creep recovery tests performed on wheat kernels versus doughs: Influence of glutenins on rheological and quality properties. *Cereal Foods World*, 58(3):139–144, 2013.

[35] H. Flanders. Differentiation under the integral sign. *The American Mathematical Monthly*, 80:615–627, 1973.

[36] A. Franck. Measuring and evaluating oscillation data. In *Application Notes (APN007)*. TA Instruments, Germany, 2005.

[37] P. Fritz, R. S. Hermanns, and A. Heinz. Modified bentonite slurries for slurry shields in highly permeable soils. In *4th International Symposium Geotechnical Aspects of Underground Construction in Soft Ground*, pages 35–40. Toulouse, France, 2002.

[38] S. Fujii and R. Murakami. Smart particles as foam and liquid marble stabilizers. *KONA Powder and Particle Journal*, 26:153–166, 2008.

[39] M. Galli. *Rheological characterisation of earth-pressure-balance (EPB) support medium composed of non-cohesive soils and foam.* PhD thesis, Ruhr-Universität Bochum, Bochum, 2016.

[40] P. Gerland, A. E. Raftery, H. Sevcikova, N. Li, D. Gu, T. Spoorenberg, L. Alkema, B. K. Fosdick, J. Chunn, N. Lalic, G. Bay, T. Buettner, G. K. Heilig, and J. Wilmoth. World population stabilization unlikely this century. *Science*, 346:234–237, 2014.

[41] R. B. Gilmer, A. N. Alexandrou, and V. Entov. On the determination of yield surfaces in Herschel-Bulkley fluids. *Journal of Rheology*, 43: 463–483, 1999.

[42] R. A. Gingold and J. J. Monaghan. Smoothed particle hydrodynamics-theory and application to non-spherical stars. *Monthly Notices of the Royal Astronomical Society*, 181:375–389, 1977.

[43] R. A. Gingold and J. J. Monaghan. Kernel estimates as a basis for general particle method in hydrodynamics. *Journal of Computational Physics*, 46:429–453, 1982.

[44] J. W. Gooch. *Encyclopedic Dictionary of Polymers.* Springer New York, 2007.

[45] V. Grishenko. Energy efficiency of tunnel boring machines. Master's thesis, KTH Royal Institute of Technology, Sweden, 2014.

[46] S. Gunasekaran and M. M. Ak. *Cheese Rheology and Texture.* CRC Press, 2002.

[47] M. E. Gurtin, E. Friet, and L. Anand. *The Mechanics and Thermodynamics of Continua.* Cambridge University Press, 2010.

[48] A. Hackley and C. F. Ferraris. *The Use of Nomenclature in Dispersion Science and Technology.* U.S. Department of Commerce, Technology Administration, National Institute of Standards and Technology, 2001.

[49] B. Haffner, Y. Khidas, and O. Pitois. Flow and jamming of granular suspensions in foams. *Soft Matter*, 10:3277–3283, 2014.

[50] M. Herrenknecht. EPB or slurry machine: The choice. *Tunnels and Tunnelling*, 26:35–36, 1994.

[51] B. Herzhaft. Correlation between transient shear experiments and structure evolution of aqueous foams. *Journal of Colloid and Interface Science*, 247:412–423, 2002.

[52] R. Höhler and S. Cohen-Addad. Rheology of liquid foam. *Journal of Physics: Condensed Matter*, 17(41):1041, 2005.

[53] A. Ikeda, L. Berthier, and P. Sollich. Unified study of glass and jamming rheology in soft particle systems. *Physical Review Letters*, 109, 2012.

[54] Z. D. Jastrzebski. Entrance effects and wall effects in an extrusion rheometer during the flow of concentrated suspensions. *Industrial and Engineering Chemistry Fundamentals*, 6:445–453, 1967.

[55] S. W. Jeong. Determining the viscosity and yield surface of marine sediments using modified bingham models. *Geosciences Journal*, 17:241–247, 2013.

[56] G. Katgert, B. P. Tighe, and M. van Hecke. The jamming perspective on wet foams. *Soft Matter*, 9:9379–9746, 2013.

[57] S. A. Khan, C. A. Schnepper, and R. C. Armstrong. Foam rheology: III. measurement of shear flow properties. *Journal of Rheology*, 32(1):69–92, 1998.

[58] S. H. Kosmatka and W. C. Panarese. *Design and Control of Concrete Mixtures*. Portland Cement Association, 1994.

[59] A. M. Kraynik. Foam flows. *Annual Review of Fluid Mechanics*, 20: 325–357, 1988.

[60] A. B. J. Kroezen and J. G. Wassink. Bubble size distribution and energy dissipation in foam mixtures. *Journal of the Society of Dyers and Colourists*, 103:386–394, 1987.

[61] A. B. J. Kroezen, J. G. Wassink, and C. A. C. Schipper. The flow properties of foam. *Journal of the Society of Dyers and Colourists*, 104: 393–396, 1988.

[62] L. Langmaack. Europe and Asia: Application of new TBM conditioning additives. In *BAUMA2001*, 6th International Symposium for tunnel construction. Verlag Glückauf GmbH, Essen, 2001.

[63] A. I. Laskar. Correlating slump, slump flow, vebe and flow tests to rheological parameters of high-performance concrete. *Materials Research*, 12(1):75–81, 2009.

[64] A. S. C. Lawrence. *Soap films*. G. Bell & Sons, 1929.

[65] Y. Leong, G. Campbell, Y. Yeow, and J. Withers. Processing parallel-disk viscometry data in the presence of wall slip. *Korea-Australia Rheology Journal*, 20:51–58, 2008.

[66] A. J. Liu and S. R. Nagel. *Constrained Dynamics on Microscopic and Macroscopic Scales.* Taylor & Francis, 2001.

[67] M. B. Liu and G. R. Liu. Smoothed particle hydrodynamics (SPH): an overview and recent development. *Archives of Computational Methods in Engineering*, 17:25–76, 2010.

[68] M. B. Liu, G. R. Liu, and K. Y. Lam. Constructing smoothing functions in smoothed particle hydrodynamics with applications. *Journal of Computational and Applied Mathematics*, 155(2):263–284, 2003.

[69] L. B. Lucy. A numerical approach to the testing of the fission hypothesis. *Astronomical Journal*, 82:1013–1024, 1977.

[70] R. F. MacMichael. A new direct-reading viscosimeter. *Journal of Industrial and Engineering Chemistry*, 7:961–963, 1915.

[71] C. W. Macosko. *Rheology: Principles, Measurements and Applications.* Wiley-VCH, 1994.

[72] B. Maidl, M. Herrenknecht, U. Maidl, and G. Wehrmeyer. *Mechanised shield tunnelling.* Ernst & Sohn, 2012.

[73] U. Maidl. *Erweiterung der Einsatzbereiche der Erddruckschilde durch Bodenkontionierung mit Schaum.* PhD thesis, Ruhr-Universität Bochum, Bochum, 1995.

[74] U. Maidl. EPB shields are once more gaining ground against hydroshields. *Geomechanics and Tunneling*, 7(1):2–3, 2014.

[75] A. Mardaru, G. Djelveh, G. Isopencu, C. Jinescu, A. M. Mares, and G. Ghimiciu. Characterizing foams flow obtained by continuous foaming operation. *University Politehnica of Bucharest Scientific Bulletin*, 73(3): 117–132, 2011.

[76] P. Marmottant, C. Raufaste, and F. Garner. Discrete rearranging disordered patterns part II: 2D palsticity, elasticity and flow of a foam. *European Physical Journal E*, 25(4):371–384, 2008.

[77] N. S. Martys, W. L. George, B. W. Chun, and D. Lootens. A smoothed particle hydrodynamics-based fluid model with a spatially dependent viscosity: application to flow of a suspension with a non-Newtonian fluid matrix. *Rheologica Acta*, 49(10):1059–1069, 2010.

[78] S. Marze, D. Langevin, and A. Saint-Jalmes. Aqueous foam slip and shear regimes determined by rheometry and multiple light scattering. *Journal of Rheology*, 52:1091, 2008.

[79] C. McEvedy and R. Jones. *Atlas of World Population History*. Puffin, 1978.

[80] S. P. Meeker, R. T. Bonnecaze, and M. Cloitre. Slip and flow in soft particle pastes. *Physical Review Letters*, 92(19):198302–198301, 2004.

[81] T. G. Mezger. *The Rheology Handbook: For Users of Rotational and Oscillatory Rheometers*. Vincentz Network, 2006.

[82] G. W. E. Miligan. Lubrication and soil conditioning in tunnelling, pipe jacking and microtunneling. *Tunnels and Tunnelling International*, 32 (7):22–24, 2000.

[83] J. J. Monaghan. Smoothed particle hydrodynamics. *Annual Review of Astronomy and Astrophysics*, 30:543–574, 1992.

[84] J. J. Monaghan. Simulating free surface flows with SPH. *Journal of Computational Physics*, 110(2):399–406, 1994.

[85] M. Mooney. Explicit formulas for slip and fluidity. *Journal of Rheology*, 2(2):210–222, 1931.

[86] K. J. Mysels, K. Shinoda, and S. Frankel. *Soap films: Studies of their thinning and a bibliography*. Pergamon Press, 1959.

[87] E. Nowak, G. Combes, E. H. Stitt, and A. W. Pacek. A comparison of contact angle measurement techniques applied to highly porous catalyst supports. *Powder Technology*, 233:52–64, 2013.

[88] A. O. Özarmut and H. Steeb. Rheological properties of liquid and particle stabilized foam. *Journal of Physics: Conference Series*, 602, 2015.

[89] A. O. Özarmut, M. Galli, H. Steeb, and M. Thewes. Two-scale investigations on the rheological properties of foam and particle-laden foams. In *Third International Conference on Computational Methods in Tunnelling and Subsurface Engineering*, pages 687–700. Aedificatio Publishers, 2013.

[90] T. C. Papanastasiou. Flow of materials with yield. *Journal of Rheology*, 31(5):385–404, 1987.

[91] D. Peila, C. Oggeri, and C. Vinai. Screw conveyor device for laboratory tests on conditioned soil for EPB tunneling operations. *Geotechnical and Geoenviromental Engineering*, 133(12):1622–1625, 2007.

[92] R. K. Prud'home and S. A. Khan. *Foams: Theory, Measurements and Apllications*. Surfactant Science Series, 1st edition, 1995.

[93] S. Psomas. Properties of foam/sand mixtures for tunnelling applications. Master's thesis, University of Oxford, Oxford, 2001.

[94] S. Quebad, M. Sibai, and J. P. Henry. Use of chemical foam for improvements in drilling by earth pressure balanced shields in granular soils. *Tunnelling and Underground Space Technology*, 13(2):173–180, 1998.

[95] G. I. S. Ranjani and K. Ramamurthy. Analysis of the foam generated using surfactant Sodium Lauryl Sulfate. *International Journal of Concrete Structures and Materials*, 4(1):55–62, 2010.

[96] M. Reiner. The deborah number. *Physics Today*, 17:62, 1964.

[97] E. Rio, W. Drenckhan, A. Salonen, and D. Langevin. Unusually stable liquid foams. *Advances in Colloid and Interface Science*, 205:74–86, 2013.

[98] N. Roussel. Correlation between yield stress and slump: Comparison between numerical simulations and concrete rheometers results. *Materials and Structures*, 39(4):501–509, 2006.

[99] N. Roussel and P. Coussot. Fifty-cent rheometer for yield stress measurements: From slump to spreading flow. *Journal of Rheology*, 49(3): 705–718, 2005.

[100] J. Schetz and A. Fuhs. *Fundamentals of Fluid Mechanics*. John Wiley & Sons, 1999.

[101] J. Schmelzer, J. Möller, V. Slezov, I. Gutzow, and R. Pascova. Ostwald ripening in porous materials. *Quimica Nova*, 21(4):529–533, 1998.

[102] L. Schneider and K. Hutter. *Solid-Fluid Mixtures of Frictional Materials in Geophysical and Geotechnical Context*. Springer Verlag, 2009.

[103] W. R. Schowalter and G. Christensen. Toward a rationalization of the slump test for fresh concrete: comparisons of calculations and experiments. *Journal of Rheology*, 42(2):865–870, 1998.

[104] G. Schramm. *A practical approach to Rheology and Rheometry*. Thermo Electron Karlsruhe, 2nd edition, 2004.

[105] R. Sivanesapillai, N. Falkner, A. Hartmeier, and H. Steeb. Pore-scale SPH study on the evolution of interfacial areas in porous media during primary drainage and imbibition. *Advances in Water Resources*, 95:212–234, 2016.

[106] A. Stocco, E. Rio, B. P. Binks, and D. Langevin. Aqueous foams stabilized solely by particles. *Soft Matter*, 7(2):1260–1267, 2011.

[107] J. W. Swegle, D. L. Hicks, and S. W. Attaway. Smoothed particle hydrodynamics stability analysis. *Journal of Computational Physics*, 116: 123–134, 1995.

[108] A. Syrakos, G. C. Georgios, and A. N. Alexandrou. Solution of the square lid-driven cavity flow of a bingham plastic using the finite volume method. *Journal of Non-Newtonian Fluid Mechanics*, 195:19–31, 2013.

[109] T. F. Tadros. *An Introduction to Surfactants.* De Gruyter, 2014.

[110] G. H. Tattersall. *The Workability of Concrete.* Cement and Concrete Association, 1976.

[111] M. Thewes. TBM tunneling challenges-redefining state of the art. Keynote lecture in world tunnel congress 2007 Prague. *Magazine Tunnel*, 16:13–21, 2007.

[112] M. Thewes, C. Budach, and M. Galli. Laboruntersuchungen von verschiedenen konditionierten Lockergesteinsböden für Tunnelvortriebe mit Erddruckschildmaschinen. In *Tunnel- International Journal for Subsurface Construction*, 4th BASF TBM Conference, pages 21–30, London, 2010.

[113] C. Tropea, A. Yarin, and J. F. Foss. *Handbook of Experimental Fluid Dynamics.* Springer, 2007.

[114] E. Tyrode, A. Pizzino, and O. J. Rojas. Foamability and foam stability at high pressures and temperatures. instrument validation. *Review of Scientific Instruments*, 74(5):2925–2932, 2003.

[115] M. van Hecke. Jamming of soft particles: geometry, mechanics, scaling and isostaticity. *Journal of Physics: Condensed Matter*, 22:24, 2010.

[116] J. F. Vincent. *Structural Biomaterials.* Macmillan, 1982.

[117] N. J. Wagner and J. F. Brady. Shear thickening in colloidal dispersions. *Physics Today*, 62(10):27–32, 2009.

[118] H. J. Walls, S. B. Caines, A. M. Sanchez, and A. Khan. Yield stress and wall slip phenomena in colloidal silica gels. *Journal of Rheology*, 47(4): 847, 2003.

[119] E. W. Washburn. The dynamics of capillary flow. *Physical Review*, 18 (3):273–283, 1921.

[120] D. Weaire, S. J. Cox, and K. Brakke. Liquid foams - precursors for solid foams. In *Cellular Ceramics: Structure, Manufacturing, Properties and Applications*, chapter 1, pages 18–28. Wiley-VCH, 2005.

[121] A. Yoshimura and R. K. Prud'homme. Wall slip corrections for Couette and parallel disk viscometers. *Journal of Rheology*, 32:53–67, 1988.

[122] Y. Yuan and T. R. Lee. Contact angle and wetting properties. *Surface Science Techniques*, 51:3–34, 2013.

[123] S. Zand-Parsa and A. R. Sepaskhah. Soil hydraulic conductivity function based on specific liquid vapor interfacial area around the soil particles. *Geoderma*, 119:143–157, 2004.

[124] H. Zhu, N. S. Martys, C. Ferraris, and D. D. Kee. A numerical study of the flow of bingham-like fluids in two-dimensional vane and cylinder rheometers using a smoothed particle hydrodynamics (SPH) based method. *Journal of Non-Newtonian Fluid Mechanics*, 165:362–375, 2010.

AYCAN ÖZLEM ÖZARMUT

PERSÖNLICHE DATEN

Geburtsdatum: 01. Mai 1984
Geburtsort: Erzincan/Türkei
Nationalität: türkisch
Familienstand: verheiratet

BERUFSERFAHRUNG

02/2011-10/2015   Wissenschaftliche Mitarbeiterin an der **Ruhr-Universität Bochum**
Lehrstuhl für Kontinuumsmechanik
Aufgaben:
-Entwicklung von kontinuumbasierten nicht Newtonischen Strömungsmodellen
-Experimente in der Verfahrenstechnik
-Mikroskopische Untersuchung von Werkstoffen
-Betreuung von Versuchen im Fachlabor Mechanik
-Durchführung von Übungsveranstaltungen
-Betreuung von Masterarbeiten

05/2010-12/2010   Studentische Hilfskraft an der **Ruhr-Universität Bochum**
Lehrstuhl für Kontinuumsmechanik
Aufgaben:
-Vorbereitung von Übungsmaterialen für die Vorlesung „Continuum Mechanics"
-MATLAB basierte Implementierung von thermomechanischen Zyklen
-Technische Zeichnungen mit kommerziellen Software

10/2009-04/2010   Studentische Hilfskraft an der **Ruhr-Universität Bochum**
Lehrstuhl für Statik und Dynamik
Aufgaben:
 -MATLAB basierte Implementierungen von FEM-Problemen
 -Strukturanalyse durch relevante kommerzielle Software

STUDIUM

02/2011 – 09/2017   **Ruhr-Universität Bochum**   Bochum/Deutschland
Ph.D., Lehrstuhl für Kontinuumsmechanik, Fakultät Bauingenieurwesen
Thema: Rheological Characterization of Particle-Foam Mixtures.

10/2008 – 11/2010   **Ruhr-Universität Bochum**   Bochum/Deutschland
M.Sc., Computational Engineering
Thema: A Comparative Study of constitutive models for Shape Memory
Polymers.

09/2003 – 06/2008   **Universität Gaziantep**   Gaziantep/Türkei
B.Sc., Maschinenbauingenieurwesen
Thema: Research of Electrical Discharge Machining (EDM)

VERÖFFENTLICHUNGEN

Özarmut, A. Ö., Kazakeviciute-Makovska, R., Steeb, H., 2012. On response functions in linear thermoelastic models of shape memory polymers. In: Proceedings in Applied Mathematics and Mechanics (PAMM), 12(1), 335-336.

Kazakeviciute-Makovska, R., Steeb, H., Aydin, A. Ö., 2012. On the evolution law for the frozen volume fraction in linear theories of shape memory polymers. Archive of Applied Mechanics, 82(8), 1103-1115

Özarmut, A. Ö., Galli, M., Steeb, H., Thewes, M., 2013. Two-scale Investigations on the Rheological Properties of Foam and Particle-Laden Foams. In: EURO:TUN 2013, 3rd International Conference on Computational Methods in Tunneling and Subsurface Engineering, Aedificatio Publishers, Proceedings ISBN 978-3-942052-01-6, CD: ISBN 978-3-942052-02-3, pages 687 – 698.

Özarmut, A. Ö., Steeb, H., 2013. Rheological Properties of Liquid and Particle Stabilized Foam. Journal of Physics: Conference Series, 602

Kazakeviciute-Makovska,R., Özarmut, A. Ö., Steeb, H., 2014. Characterization of shape memory polymer Estane (TM) by means of dynamic mechanical thermal analysis technique, Smart Materials Research, Article ID 250258, 2014 doi:10.1155/2014/250258 (open access)

PRAKTIKA

07/2007 – 09/2007	**Anteks Textile Company**	Antalya/Türkei
	-Kaufmännische Prozesse	
	-Lagerung und Lagerkontrolle	
	-Qualitätskontrolle	
07/2006 – 09/2006	**ThyssenKrupp Steel Europe AG**	Duisburg/Deutschland
	-Wärmbehandlung und Warmbearbeitung	
	-Technische Zeichnungen mittels AutoCAD	
07/2005 – 08/2005	**Universität Gaziantep**	Gaziantep/Türkei
	-Ein- und Ausbau eines Automotors	
	-Herstellung eines Schraubstocks aus Stahl durch Bohren, Schleifen und Fräsen	
	-Schweißen	

BESONDERE KENNTNISSE & INTERESSEN

Sprachen	Türkisch	Muttersprache
	Deutsch	Verhandlungssicher
	Englisch	Verhandlungssicher
Software	Math.: Matlab,	
	Programmierungs-/Skriptsprachen: Fortran, Java, Matlab	
	FEM & CAD: AutoCAD, Solidworks, Ansys	
	MS Office	
Hobbys	Kochen, Reisen, Malen, Schwimmen, klassische Musik	